Département de physique
Université de Fribourg (Suisse)

Two non-destructive neutron inspection techniques: Prompt gamma-ray activation analysis and cold neutron tomography

THESE

Présentée à la Faculté des Sciences de l'Université
de Fribourg (Suisse) pour l'obtention du grade de
Doctor rerum naturalium

Sébastien Baechler
de Rechthalten (FR)

Thèse No 1381

Edition Mécanographie
2002

Acceptée par la Faculté des Sciences de l'Université de Fribourg (Suisse) sur proposition de:

Prof. Dr. P. Schurtenberger, Université de Fribourg, Président du Jury,
Prof. Dr. J.-C. Dousse, Université de Fribourg, Directeur de Thèse,
Prof. Dr. J. Jolie, Universität zu Köln, Directeur de Thèse,
Dr. E. Lehmann, Paul Scherrer Institut, Rapporteur.

Fribourg, le 3 juillet 2002

Les directeurs de thèse:

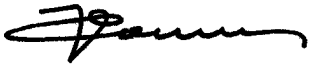

Prof. Dr. J.-C. Dousse

Prof. Dr. J. Jolie

Le doyen

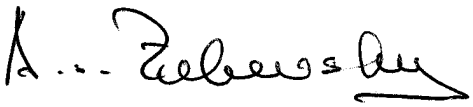

Prof. Dr. A. von Zelewsky

Contents

Abstract

Two non-destructive inspection techniques employing both cold neutron beams have been developed at the Swiss spallation source SINQ of the Paul Scherrer Institute: (1) prompt gamma-ray activation analysis (PGAA) and (2) neutron tomography.

PGAA is a nuclear analytical method for identifying and quantifying simultaneously the elements contained in a sample. The technique consists in detecting capture gamma rays emitted by the target material during neutron irradiation. The PGA facility at SINQ was designed, constructed, and tested by Prof. J. Kern and Dr. M. Crittin. In the present work, a new analytical approach, namely the k_0-standardization, has been studied and applied to obtain higher accuracies in the determination of element concentrations. First, this method has been applied successfully for quantitative determination of boron in aqueous solutions. Then, standard reference materials were analyzed to assess the accuracy of the method for multielement determination. Finally, the technique was applied to various samples from archeology, geology, medicine, nuclear industry and material science. Of particular interest was the concentration determination of hydrogen and boron, two elements that are difficult to measure with other techniques. Besides, a neutron focusing capillary lens was used to measure element concentrations in two-dimensional array across the surface of a bulky sample from a natural reactor. A description of the PGAA technique and of some results is presented in the first part of this thesis.

A new cold neutron tomography set-up was developed at SINQ in collaboration with the University of Ghent (Belgium) with the objective to complement the existing thermal neutron radiography station. The new device was set up at the same beam line as the PGA instrument so that the two facilities were employed alternately. Neutron tomography is similar to X-ray tomography, which is widely used in medicine and industry. It provides three-dimensional information on the inner structure of a sample. As a result of the differences between neutron and X-ray interaction mechanisms, complementary information is provided by the two techniques. Unlike X-rays, neutrons have the prominent ability to penetrate most metals easily while delivering a high contrast for many light elements. Besides, if cold neutrons are used, thicker sections of metallic materials can be inspected. The whole tomography system consisted of a rotation table and an imaging device, which was based on a scintillator converting the neutron beam to a light image viewed with a CCD camera. The achievable resolution was limited by the inherent divergence of the neutron guide (L/D = 70) and was about 0.24 mm under optimal conditions. Furthermore, a neutron velocity selector was used to perform radiography and tomography experiments with monochromatic neutron beams. Finally, examinations were performed on objects covering a broad range of application fields, such as geology, dentistry, archeology, nuclear industry and aerospatial industry. A detailed presentation of the cold neutron tomography set-up and some results obtained with this technique are given in the second part of this thesis.

Résumé

Deux techniques d'inspection non-destructives utilisant des faisceaux de neutrons froids ont été développées à la source de neutrons SINQ de l'Institut Paul Scherrer : (1) l'analyse par activation neutronique prompte (PGAA) et (2) la tomographie neutronique.

L'analyse par PGA (Prompt Gamma-ray Activation) est une méthode nucléaire qui permet de déterminer la concentration d'éléments présents dans un échantillon. Cette technique consiste à détecter les rayons gamma prompts émis par l'échantillon suite à des réactions de captures neutroniques. L'installation PGA à SINQ a été conçue, construite et testée par le prof. J. Kern et la Dr. M. Crittin. Cette thèse propose une nouvelle approche analytique, nommée la standardisation du k_0, qui permet d'obtenir une meilleure précision dans la détermination des concentrations. Cette méthode a été utilisée tout d'abord pour mesurer la quantité de bore dans des solutions aqueuses. Puis, la mesure de matériaux de référence a prouvé la validité de la méthode pour des analyses multi-élémentaires. Finalement, divers échantillons provenant de domaines très variés tels que l'archéologie, la géologie, la médecine, l'industrie nucléaire et la science des matériaux, ont été étudiés avec cette technique. Le PGAA s'est révélé particulièrement important pour l'analyse de l'hydrogène et du bore qui sont difficilement mesurables avec d'autres techniques. En outre, une lentille à neutrons a permis de déterminer la distribution bidimensionnelle d'éléments dans un échantillon provenant d'un réacteur naturel. La première partie de cette thèse décrit la technique et les résultats de l'analyse par PGA.

Une installation de tomographie utilisant des neutrons froids a été développée en collaboration avec l'Université de Gand (Belgique) sur la même ligne de faisceau que le système PGA, les deux instruments étant utilisés de façon alternée. La tomographie neutronique est semblable à la tomographie par rayons X, laquelle est couramment utilisée dans les sciences médicales et l'industrie. Comme celle-ci, elle fournit des informations tridimensionnelles sur la structure des échantillons. Cependant, comme les processus d'interaction des neutrons et des rayons X avec la matière sont différents, les informations fournies sont complémentaires. Contrairement aux rayons X, les neutrons pénètrent facilement la plupart des métaux, ce qui permet d'améliorer le contraste des éléments légers. Par ailleurs, les neutrons froids rendent possible l'étude de matériaux métalliques encore plus denses. L'installation comprenait une table de rotation et un détecteur, lequel était composé d'un scintillateur et d'une caméra CCD. La résolution, qui était limitée par la divergence du guide de neutrons (L/D = 70), était d'environ 0.24 mm dans des conditions optimales. En outre, un dispositif permettant de sélectionner la vitesse des neutrons a été utilisé pour des expériences de radiographie et de tomographie nécessitant des faisceaux monochromatiques. Finalement, différentes études ont porté sur des objets provenant de la géologie, l'archéologie, la médecine dentaire, l'industrie nucléaire et l'aérospatiale. Cette technique et ses résultats font l'objet de la deuxième partie de cette thèse.

PART I : PROMPT GAMMA-RAY ACTIVATION ANALYSIS

I-1 Introduction

Basic concept

Prompt gamma-ray activation analysis (PGAA) is a non-destructive nuclear method for performing both qualitative and quantitative multi-element analysis of major, minor, and trace elements in samples. Especially, the technique is used for the analysis of light elements such as H, B, C, N, Si, P, S and Cl, as well as for heavy elements such as Cd, Sm, Gd and Hg [1].

The nuclear reaction used for PGAA is the neutron capture, also called (n,γ) reaction. When a neutron is absorbed by a target nucleus, the compound nucleus is in an excited state with energy equal to the binding energy of the added neutron. Then, the compound nucleus will almost instantaneously (< 10^{-14} s) de-excite into a more stable configuration through emission of characteristic prompt gamma rays. In many cases, this new configuration yields a radioactive nucleus which also de-excites (or decays) by emission of characteristic delayed gamma rays. PGAA is based on the detection of the prompt gamma rays emitted by the target during neutron irradiation, while neutron activation analysis (NAA) is utilizing the delayed gamma rays from the radioactive daughter nucleus (Fig. 1).

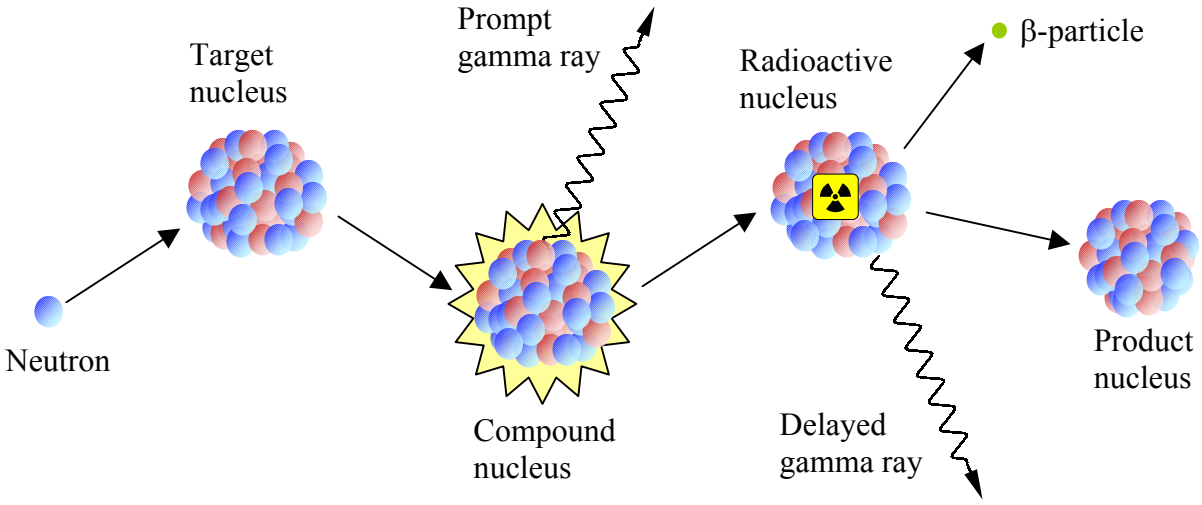

Fig. 1. Diagram illustrating the neutron capture by a target nucleus followed by the emission of gamma rays.

Consequently, PGAA is a complementary technique to NAA by allowing determination of elements that do not form radioactive products after irradiation (e.g., H and B), and elements for which the half life is too long to be conveniently measured by NAA (e.g., C.). Boron is the only exception to the usual prompt gamma-rays measurement, in which the gamma measured is not due to the (n,γ) reaction. Indeed, boron (like lithium-6) reacts with neutrons by emissions of α-particles, i.e. via the reaction $^{10}B(n, \alpha)^{7}Li$. Most of the ^{7}Li are formed in the excited state and de-excited instantaneously ($7.3 \cdot 10^{-14}$ s) by emission of 477 keV gamma-rays. Thus, the boron neutron capture process is written as $^{10}B(n, \alpha\gamma)^{7}Li$.

The PGAA technique requires mainly a source of neutrons and high-resolution spectrometers for measurement of gamma rays with energies over the range from about 100 keV to 11 MeV. Then, the energies of the prompt gamma rays identify the neutron-capturing elements, while the intensities of the peaks at these energies reveal their concentrations. The development of analytical methods for PGAA is given in details further in this chapter (see k_0-standardization approach).

The PGA facility at PSI

The PGA facility was installed at the end of the cold neutron guide 1RNR12 at the Swiss spallation source SINQ (Paul Scherrer Institute, PSI). At the SINQ, neutrons are produced with a spallation reaction, in which a heavy metal (lead) is bombarded with the proton beam from the PSI accelerator [2]. In 2001, the neutron flux at the exit of the PGA guide was about $1.8 \cdot 10^{8}$ n/cm^2 at a nominal proton current of 1.2 mA on the SINQ target.

The PGA set-up was designed, constructed, and tested by Prof. J. Kern and Dr. M. Crittin during her Ph.D. work. The system consisted mainly of a sample chamber and holder, two spectrometers, i.e. a Compton-suppressed spectrometer and a pair spectrometer, and detector shielding against neutrons and gamma radiation. An interesting feature of this installation is the use of a neutron focusing lens to perform two-dimensional scanning of samples. The PGA facility was described at length in Ref. [3] and more succinctly through the papers in chapter I.2.

New software for acquisition (GARDAS, namely Gamma-ray Data Acquisition Software, by S. Baechler) and for analysis (PEGASE, namely Program Evaluating Gamma-ray Spectra for the determination of Elemental compositions, by Dr. L. Genilloud [4]) were developed under the Labview environment.

k_0 standardization approach

For a sample irradiated in a neutron beam with flux ϕ for a time t, the peak area A of a neutron capture γ-ray of energy E_γ from mass m of element x is in given by :

$$A_{x,E_\gamma} = N_x \sigma \phi t I_{\gamma,x} \varepsilon_{\gamma,x} = \frac{m_x N_A \theta_x}{M_x} \cdot \sigma \phi t I_{\gamma,x} \varepsilon_{\gamma,x} \qquad (1)$$

where N_x is the number of target nuclei, N_A the Avogadro's number, θ the abundance of the capturing isotope, M the atomic weight, σ the effective cold neutron capture cross-section, I_γ the γ-ray abundance per neutron capture and ε the absolute full energy peak detection efficiency. Since most of the factors in Eq. (1) have constant values, the peak area is only proportional to the mass and the irradiation time. However, I_γ and σ are given with insufficient accuracy in nuclear data libraries and thus the absolute method has not been pursued in PGAA work.

The usual analysis for PGA was carried out using a comparative method. Indeed, element concentrations (or masses) were determined by comparing the gamma-ray count rate of an element in an unknown sample to the corresponding element sensitivity. The analytical sensitivity S of an element x is defined as the gamma-ray count rate of a known amount of the element:

$$S_x = \frac{A_\gamma / t}{m} \qquad \text{(in cps·mg}^{-1}\text{)} \qquad (2)$$

This method, also called the relative standardization, has been applied to the PGA measurements at SINQ by Dr. M. Crittin during her Ph.D. work.

However, element sensitivities are dependent upon the geometry and composition of the sample [5]. If the sample matrix contains large concentrations of neutron absorbing nuclides, self-shielding occurs, resulting in a decrease in element sensitivities. The presence of large concentrations of neutron scattering nuclides may increase or decrease sensitivities, depending on the geometry of the sample. Furthermore, scattering of cold neutron within the warm target results in an increase in the average neutron energy, and a significant decrease in element sensitivities. The neutron flux and its energy distribution are perturbed not only through complicated processes of absorption and scattering within the sample, but also though the scattering from the wall of the sample box and from the atoms of the ambient gas.

One approach to the problem is to prepare standards matching closely the sample in geometry and composition for every element to be determined. On the other hand, this approach is time consuming for multi-element analysis or for a large variety of samples.

The analytical biases due to neutron scattering and absorption are largely eliminated using the internal monostandard method (or k-standardization) [5]. In other words, the sensitivity for a studied element x is determined relatively to that of an internal comparator c. Then, using Eq. (1) and (2), the relevant sensitivity ratio, namely the k-factor, is given by the following expression:

$$k_c(x) = \frac{S_x}{S_c} = \frac{\theta_x \sigma_{0,x} I_{\gamma,x} / M_x}{\theta_c \sigma_{0,c} I_{\gamma,c} / M_c} \cdot \frac{\varepsilon_{\gamma,x}}{\varepsilon_{\gamma,c}} \tag{3}$$

It has been assumed that, for nearly all elements at neutron energies less than 5 meV, the neutron cross section (σ) is inversely proportional to velocity v, hence $\sigma=\sigma_0 \cdot v_0/v$, where v_0 is the standard velocity of thermal neutron (2200 m/s). Thus, the k-factors are independent of the neutron energy, and the sample matrix and geometry. This approach has been applied successfully at the PGA facility of SINQ for quantitative determination of boron in aqueous solutions. The paper related to this study has been accepted for publication in Nuclear Instruments and Methods in Physics Research A.

Furthermore, the k-factors can be evaluated as universal constants by eliminating the detector efficiency dependance and thus applied in any PGA system:

$$k_{0,c}(x) = \frac{S_x / \varepsilon_{\gamma,x}}{S_c / \varepsilon_{\gamma,c}} = \frac{\theta_x \sigma_{0,x} I_{\gamma,x} / M_x}{\theta_c \sigma_{0,c} I_{\gamma,c} / M_c} \tag{4}$$

Knowledge of the prompt k_0-factors allows the determination of the relative concentration of any element detectable in the sample. The relative concentration C of element x with respect to element y in the same sample is given by the formula:

$$C_{x,y} = \frac{m_x}{m_y} = \frac{S_x / \varepsilon_{\gamma,x}\, k_{0,c}(x)}{S_c / \varepsilon_{\gamma,c}\, k_{0,c}(y)} \tag{5}$$

If the mass (or concentration) of one element is known, the absolute concentration of any other element can be determined. Otherwise it is necessary to measure only a single standard containing the comparator element to determine absolute concentrations. In this case the standard should be of comparable geometry and have comparable scattering and absorption properties.

Prompt k_0-factors have been determined for 26 elements to facilitate quantitative analysis, without the necessity of using element standards. Results of this study were submitted for publication in Journal of Radioanalytical and Nuclear Chemistry. In a previous work, theoretical k_0-values were used in combination with the neutron lens to perform elemental mapping of a sample coming from a natural fossil reactor. For that study, more emphasis was given to qualitative than quantitative results. The results of this project have been published [J. Radioanal. Nucl. Chem., 250 (2001) 39].

Applications

Many applications, covering a wide variety of fields, were realized in collaboration with partners from universities and research institutes. The most interesting applications fields are highlighted in the following Table together with the object of the analysis and the different collaborations (more details are given in chapter I.2).:

Fields	Objects/Analysis	Collaborations
Archeology	Major components (Cu, Zn, Sn, Pb) in Roman brooches	Archeologists A. Mazur & K. Mazur (Musée romain d'Avenches)
Geology	Boron in water samples	Prof. U. Krähenbühl (Univ. Bern), J. Grimm, (Diplomarbeit Chemie, Univ. Bern), Pierre Christe (Ph.D. Thesis, Univ. Basel)
	Multi-element analysis of powder samples	
Medicine	Boron taken up by cells in a new treatment for rheumatoid arthritis.	Dr. N. Stritt (Diploma-thesis NDS Medizin Physik, ETHZ), Dr. N.E.A. Crompton (PSI)
Nuclear industry	Multi-element analysis of ashes from the PSI-incinerator.	Dr. H.F. Beer (PSI), Dr. P. Zimmermann (PSI)
Material science	Hydrogen in YBCO crystal	Dr. H. M. Ronnow (Institut Laue-Langevin)
	Hydrogen in Zr-alloys	Dr. E. Lehmann (PSI)
	Boron in Ni_3Al-alloys	F. della Torr (Ph.D. Thesis, PSI)
	Boron in graphite reactor	Dr. K. Kirch (PSI)
	Determination of Ge/Bi & Si/Bi-ratios in BGO/BGSO crystals	V. Vaithianathan (Crystal Growth Centre, Anna University, India)

Outlook

The PGA facility was dismantled in January 2002 and will be transferred to the new Munich research reactor FRM-II in a near future. A net increase of the performances is expected due to the higher neutron flux available at FRM-II and the use of the new generation of highly efficient gamma-ray spectrometers.

References

[1] Z. B. Alfassi, C. Chung (Ed.), Prompt Gamma Neutron Activation Analysis, CRC Press, Boca Raton, Florida, 1995.

[2] For further information, see http://asq.web.psi.ch/ASQ/facilities/SINQSYSTEMS.html).

[3] M. Crittin, J. Kern, J.-L. Schenker, Nucl. Instr. and Meth. A 449 (2000) 221.

[4] L. Genilloud, PEGASE. Program evaluating gamma-ray spectra for the determination of elemental compositions. Internal Report IFP-PAN, University of Fribourg, Switzerland, 2000.

[5] R.L. Paul, J. Radioanal. Chem. 191 (1995) 245.

[6] G. L. Molnár, ZS. Révay, R. L. Paul, R. M. Lindstrom, J. Radioanal. Chem. 234 (1998) 21.

Prompt gamma ray activation analysis for determination of boron in aqueous solutions

S. Baechler [a,b], P. Kudejova [c], J. Jolie [c], J.-L. Schenker [a], N. Stritt [d]

[a] *Physics Department, University of Fribourg, Ch. du Musée 3, CH-1700 Fribourg, Switzerland*
[b] *Paul Scherrer Institute, CH-5232 Villigen, Switzerland*
[c] *Institut für Kernphysik, Universität zu Köln, D-50937 Köln, Germany*
[d] *Bundesamt für Gesundheit, CH-3003 Bern, Switzerland*

Prompt gamma-ray activation analysis (PGAA) is a nuclear analytical technique for the determination of trace and other elements in solid, liquid or gaseous samples. The method consists in observing gamma rays emitted by a sample during neutron irradiation. Of particular importance for PGAA is the measurement of boron. Indeed, this technique gives the opportunity to detect boron concentration down to the ppm or ppb level depending on the sample matrix. Furthermore, boron cannot be easily measured by other methods without risks of contamination. Trace analysis of boron in liquids has been performed and characterized at the PGA facility of the neutron spallation source SINQ (Paul Scherrer Institute, Switzerland). First, a calibration curve was determined with standard boron solutions. Then, the PGAA was applied for the determination of boron in geological water samples. The results were compared with ICP-MS measurements. Finally, the method yielded promising results to measure the concentration of boron taken up by cells in a new treatment for rheumatoid arthritis.

Keywords: Prompt gamma-ray activation analysis; Boron detection; Non-destructive.

1. Introduction

Prompt gamma-ray activation analysis (PGAA) is a non-destructive technique to identify elements and determine their concentration in a sample [1]. The method is based on the detection of capture gamma rays emitted by a sample during neutron irradiation. Then, the elemental concentration is retrieved for the identified elements. The measurements used to detect boron are based on the detection of the 478 keV gamma rays following the reaction $^{10}B(n,\alpha)^{7}Li$. The isotopic abundance of ^{10}B in natural boron is 18.3% of weight units. The recoiling ^{7}Li nucleus, initially in an excited state, decays with 94% by the Doppler-broadened 478 keV prompt gamma ray [2]. Thus, the boron peak is easy to identify in a

prompt gamma-ray spectrum, because it is wider than the other.

The sensitivity of an element is strongly correlated with its neutron capture cross-section that varies nearly randomly between isotopes. Due to the exceptionally large cross-section of ^{10}B nucleus (3837 b for thermal neutrons), boron can be easily detected by PGAA with a detection limit in the order of 1 mg/l, i.e. 1 ppm [3, 4]. Using cold neutrons increases the sensitivity of boron because its capture cross section follows the 1/v dependence, where v is the neutron velocity [5].

Boron concentration is relatively difficult to determine using other methods. Indeed, although Inductively Coupled Plasma (ICP) techniques are very sensitive, they have problems of contamination and evaporation because the sample must be processed before measurements. On the other hand, PGAA requires no special preparations of samples, because it is a non-destructive method. These conditions make boron a very suitable element for PGAA. Consequently, the PGA facility at SINQ has been directed specifically to boron analysis. The aim of the present study was to determine boron traces in liquid samples.

2. Experimental set-up

The PGA facility has been built at the end of the 1RNR12 cold neutron guide of the Swiss spallation source SINQ at the Paul Scherrer Institute (Villigen, Switzerland). A 590 MeV protons beam bombards a lead target, causing it to be broken down whereby many neutrons are liberated, which are slowed down in a heavy water moderator. A fraction of the released neutrons are cooled by 25 K liquid deuterium and transported to the experiments by neutron guides [6]. The beam size at the sample position is 20 mm wide and 50 mm high and the present neutron flux is about $1.4 \cdot 10^8$ n/cm^{2}s. The neutron wavelength spectrum measured by time of flight shows a maximum at about 4 Å on a nearly Maxwellian distribution [7].

The PGA facility is mainly composed of a detection system, a sample box and shielding (Fig. 1). The neutron beam interacts with the sample placed in a target chamber made out of aluminum. A sample changer, consisting of a Teflon ladder, enables to place six different samples that can be moved vertically by a step motor. Then, prompt gamma rays are detected by the Compton-suppressed spectrometer resulting in a high signal-to-noise ratio. The spectrometer is composed of a coaxial-type high-purity Ge detector shielded by a 240×240 mm^2 by 250 mm long NaI(Tl)/BGO scintillator. The BGO part is situated in the forward direction where the Compton-scattered radiation have the highest energies. Software for acquiring the data and positioning the motor was developed on Labview© and enables the measurement of six samples automatically.

In the construction, special attention was given to obtain a very low contribution of gamma rays emitted following boron capture

in the shielding. Consequently, B_4C was essentially excluded for neutron shielding. The internal wall of the sample box is covered by an ^{6}LiF polymer (6 mm thick). The entrances to the gamma-ray collimators are covered by 1-cm-thick ^{6}LiF tiles to avoid the neutrons reaching the Ge detector. ^{6}LiF tiles were used because of their low gamma emission. Furthermore, the spectrometer is also protected by neutron/gamma shields consisted of cadmium foils (thickness 1 mm) and lead bricks (5-15 cm). Finally, the instrument, placed inside a concrete bunker, has a very low background of gamma rays for (n,γ) measurement. The PGAA facility at SINQ has been described in more detail elsewhere [8].

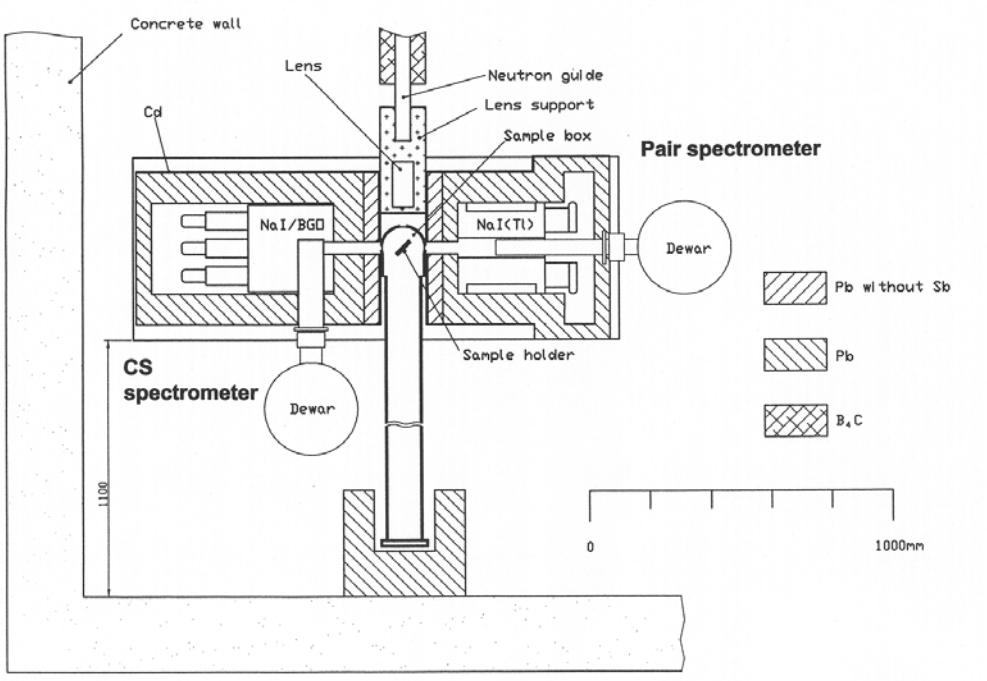

Fig. 1. Schematic horizontal cut of the prompt gamma activation facility at SINQ.

3. Analytical method

To perform analytical measurements, the method consisted in determining the analytical sensitivity (cps/mg) for different elements: for a precise amount of each of the pure elements, the areas under the strongest peaks were determined [8]. Then multi-elements samples were irradiated and the observed peak areas were compared with the corresponding analytical sensitivities.

However, element sensitivities depend strongly on the geometry and the composition of the sample [9]. Indeed, self-shielding occurs in samples containing large amounts of neutron absorber nuclides (typically boron) resulting in lower element sensitivities. Furthermore, an increase or decrease in elemental sensitivities, depending on the sample geometry, ensues from large concentrations of neutron scattering nuclides (hydrogen particularly). Finally, the scattering of cold neutrons within a warm

target (room temperature) results in an increase in the neutron energy, and thus a significant decrease in element sensitivity [10, 11]. Because the matrix of a multi-element sample is completely different from the one of a pure material, this method is not really reliable on its own, but requires particular studies of the target. Besides, the impacts of these processes on the measurements are extremely difficult to be evaluated.

These analytical biases disappear in homogenous samples if elemental ratios are determined [9, 12, 13]. The ratio of the experimentally measured sensitivity for a studied element to that of an internal standard is independent of sample geometry or composition. This ratio is defined as the relative sensitivity $k_{x,s}$ and is determined with known samples as follows:

$$k_{x,s} = \frac{A_{0,x}/C_{0,x}}{A_{0,s}/C_{0,s}} \qquad (1)$$

where A_0 is the net peak area and C_0 the concentration for the element of interest x and the internal standard s in a known sample. Then, the concentration of the element of interest in an unknown sample is give by

$$C_x = \frac{A_x/A_s}{k_{x,s}/C_s} \qquad (2)$$

where A is the net peak area and C the concentration for the element of interest x and the internal standard s in an unknown sample.

This approach was particularly suitable for the analysis of boron (absorber nuclides) in water sample (scatter nuclides). A sample matrix of distilled water consists of 11.2 % weight units of hydrogen. In the present study, the concentration of hydrogen in known and unknown samples was identical ($C_{0,H} = C_H$). Thus, relations (1) and (2) were simplified, with hydrogen as the inner monitor and boron as the element of interest

$$C_B = \frac{A_B/A_H}{k_{B,H}}$$

with

$$k_{B,H} = \frac{A_{0,B}/A_{0,H}}{C_{0,B}} \qquad (3)$$

The relative sensitivity $k_{B,H}$ was obtained by plotting the peak area ratio (B/H ratio) versus the boron concentration.

4. Measurements and analysis

A set of standard samples with various natural boron concentration in the range of 1-350 ppm were prepared by diluting the standard solution of 1 g/l boric acid (H_3BO_3) with distilled water. Then, 1 ml of the prepared solutions were pipetted into polytetra-fluoroethylene (PTFE) vials of cylindrical shape that were 10 mm in outer diameter, 0.5 mm in thickness and 30 mm in height. Using the analytical method described above, changes in pipetted volume of solution did not modify the accuracy of the results. Then, the samples were irradiated from 15 min (350 ppm) to 3 h (distilled water) depending on the

boron concentration. Indeed, when a statistical error of 2.4% was obtained in 2 h for the 1.75 ppm sample, a 17.5 ppm solution required approximately 1 min for the same statistics. Finally, 1 ml solutions of three different geological samples provided by International Atomic Energy Agency (IAEA) were measured during 2 h.

The prompt gamma-ray spectrum in Fig. 2 shows the Doppler-broadened boron peak (478 keV), as well as the strong hydrogen peak (2223 keV) and the single- and double-escape peaks. Several peaks corresponded to neutron capture reactions of carbon and fluorine, which were the major components of the Teflon vials. The background level was increased by a factor of 2 in the boron peak region when measuring liquid solutions instead of empty vials (Fig. 3). Indeed, with hydrogenous samples, neutrons were scattered out of the target into the surrounding material, thus enhancing considerably the background. The Doppler broadening of the boron peak increased considerably the probability of interference from other gamma rays [3]. In this study, the boron peak was overlapped with prompt gamma rays from ^{23}Na (472 keV). This contamination came from the NaI(Tl) scintillator making up parts of the Compton-suppressed detector. The statistical fluctuation of the boron peak concealed the Na peak in case of high boron content in the samples (Fig. 3). A minor contribution came from the ^{6}LiF tiles used as neutron shielding material. In this case, the 478 keV peak from the ^{6}Li(n,γ)^{7}Li reaction was not broadened. Considering the

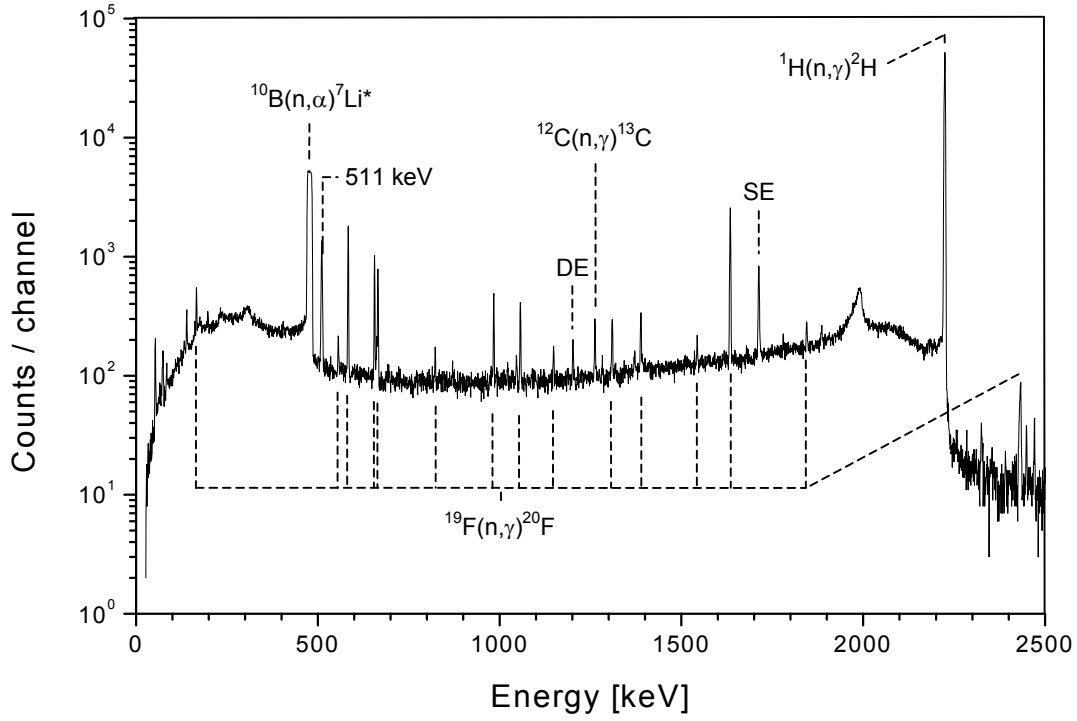

Fig. 2. Partial prompt gamma-ray energy spectrum measured at the PGA facility. The sample, a standard solution containing 105 ppm of ^{nat}B, was measured during 30 min.

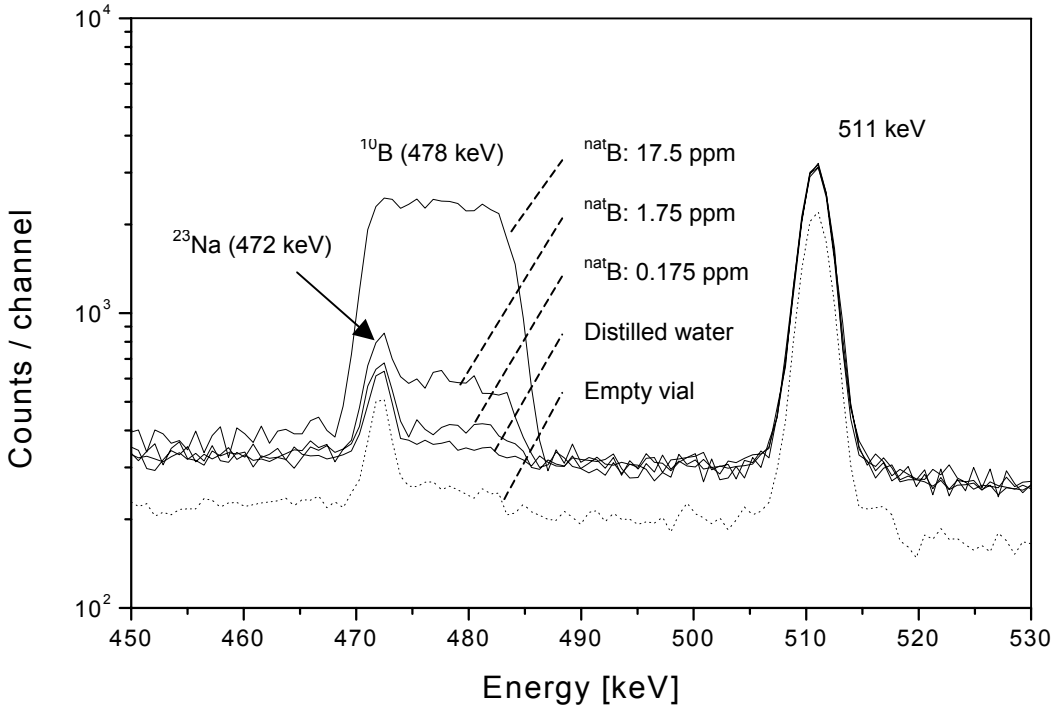

Fig. 3. Part of prompt gamma-ray spectra near the boron peak for various boron concentrations.

small cross section of the reaction (0.038 b for thermal neutrons), the influence of this peak was significant only at low boron concentrations (< 5 ppm).

A boron peak decomposition method was developed by Magara and Yonezawa [14]. The region of interest is decomposed into a broad peak, interfering normal peaks and a background. The Doppler-broadened 478 keV peak is represented by an integral of the Gaussian function. The fitting function for the explored boron Doppler-broadened peak area can be written as a sum of these separated functions

$$F(E) = F_{Na}(E) + F_{Li}(E) + F_B(E) + F_{Bckg}(E) \quad (4)$$

where $F_{Na}(E)$ and $F_{Li}(E)$ are common Gaussian shape functions for sodium (472 keV) and lithium (478 keV) peaks, $F_B(E)$ describes the boron Doppler-broadened shape and finally $F_{Bckg}(E)$ gives the background contribution. The line shape function for the Doppler-broadened boron peaks is obtained as the following integral:

$$F_B(E) = N\int_0^{\pi} \exp\{-\frac{(E - E_0 + k\cos\theta)^2}{2\sigma^2}\}\sin\theta \, d\theta \quad (5)$$

where E_0 is the centroid position of the peak, N and σ represent the peak amplitude and width, respectively. The relation $k\cos\theta$ gives the Doppler broadening ΔE. Expression (5) has no analytical solution, nevertheless, after integrating and some adjustments, the function can be written as follows:

$$F_B(E) = \frac{Area}{4k}\{erf\frac{(E - E_0 + k)}{\sqrt{2}\sigma} - erf\frac{(E - E_0 - k)}{\sqrt{2}\sigma}\} \quad (6)$$

where the new parameter $Area$ gives the searched boron peak net area.

The background can be fitted to a linear function of energy with parameters a, b:

$$F_{Bckg}(E) = aE + b. \qquad (7)$$

Another possibility is to use a more complicated function according to Magara and Yonezawa [14]:

$$F_{Bckg} = A \arctan\{b(E - E_2)\} + C \qquad (8)$$

where A, b, E_2 and C are free parameters. This function is suitable for intense boron peaks (i.e. concentration higher than 5 ppm) because it includes the low energy step caused by low angle Compton scattering of radiation from the surrounding material back to the detector. According to the experience with fitting procedure, the E_2 parameter can be set equal to the E_0 of the boron peak. The Origin 5.0 was used for proper peak analysis and the fitting function $F(E)$ was implemented to the nonlinear fitting procedure. The resulting fit of the boron peak decomposition procedure is shown in Fig. 4.

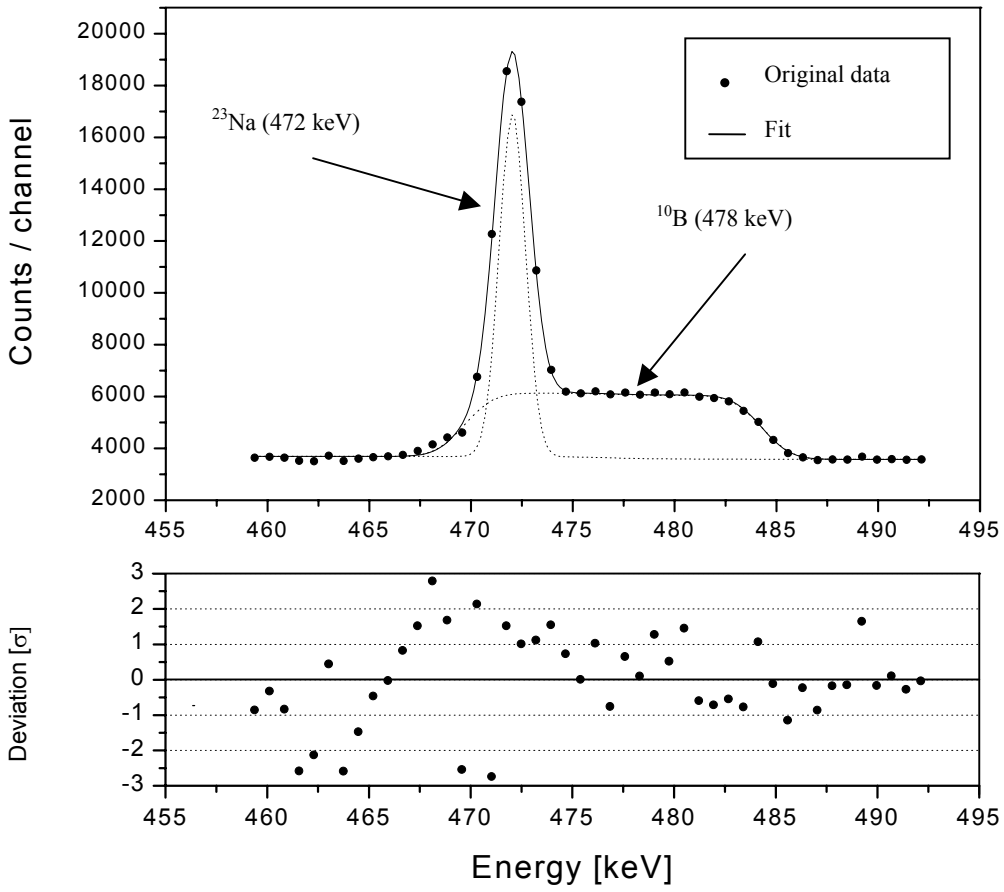

Fig. 4. Resulting fit for the seawater IAEA sample showing the decomposition of the ^{23}Na and ^{10}B peaks.

5. Results and discussions

The calibration curve was obtained by plotting the peak area ratio of the 478 keV boron and the 2223 keV hydrogen versus the known boron concentration of 21 samples (Fig. 5). The measured value for 17.5 ppm natural boron solution are determined with a statistical error of 1% and for comparison: 0.175 ppm … 10%; 1.75 ppm … 2.5%; 175 ppm…0.7%. The experimental data points fit the straight line given by the relation: $y = (0.0369 \pm 0.0001)x + (0.012 \pm 0.001)$, where y is the concentration in ppm units and x is the B/H ratio with related errors corresponding to one standard deviation (1 SD). Indeed, the linear regression yielded a correlation coefficient $R = 0.9997$ and the method demonstrated good linearity over a wide range (Fig. 5). The slope of the calibration plot gave the sensitivity of the technique, while the intercept yielded the signal from the blank (background). According to the International of Pure and Applied Chemistry (IUPAC) definition, the limit of detection (LOD) was given by the blank signal plus three standard deviations of the blank signal [15]. In the present case, the blank signal was estimated by the intercept and the standard deviation was determined by the standard error on the intercept. Then, the calculated value is substituted into the linear relation to obtain the corresponding concentration. Thus, the LOD is given by 3·SD/slope = 0.08 ppm. Similarly, the limit of

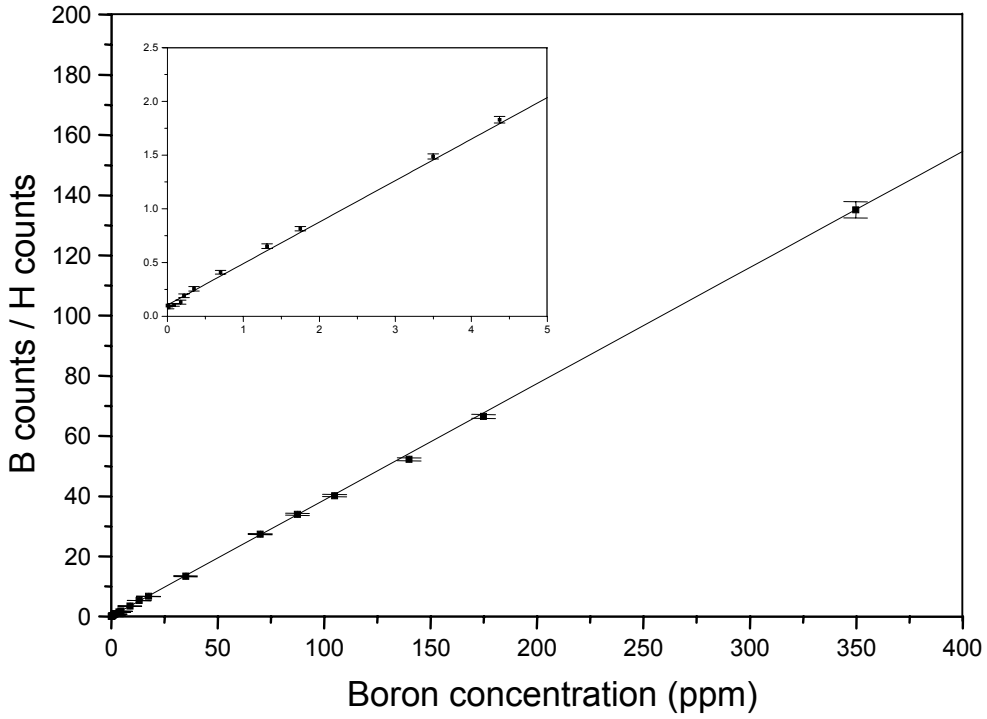

Fig. 5. Linear fit of the calibration curve obtained by plotting the peak area ratio of boron and hydrogen versus the boron concentration.

quantification (LOQ), that is the lowest concentration which can be quantified with an acceptable statistical significance, was determined by 10·SD/slope = 0.26 ppm.

Finally, the calibration curve was used to estimate boron concentrations of unknown samples. In that case, there were two sources of uncertainties for measured data evaluation: the statistical errors from the spectrum evaluation based on 1SD and the uncertainty from the calibration curve determination. The results of the IAEA samples were in good agreement with the values obtained by ICP methods (Table 1) [16]. Although boron was most certainly detected in the sample "Groundwater 1", insufficient statistics restricted the concentration to a relative error of 30%. Moreover, the boron concentration of this sample was below the limit of quantification.

Table 1. Analytical results of natural boron (in ppm) for three geological samples

Sample Description	This work	ICP-MS [a]	ICP-OES [a]
Sea water	4.8 ± 0.2	4.9 ± 0.2	5.3 ± 0.3
Groundwater 1	0.20 ± 0.06	0.193 ± 0.006	0.22 ± 0.02
Groundwater 2	1.83 ± 0.07	1.75 ± 0.05	1.77 ± 0.09

[a] Ref. 16

6. Conclusions and outlook

In the present investigation, PGAA was used to determine natural boron concentration in aqueous samples. The analytical procedure proved to yield reliable quantitative results for concentrations in the range from 0.26 to 350 ppm of natural boron. The advantage of the method was the independence of n-H scattering, the self-shielding of boron and geometry variance. As opposed to the boron amount needed for quantitative analyses, boron trace was detectable down to 0.08 ppm (or 0.016 ppm of ^{10}B). To our knowledge, the performance of the PGA facility at SINQ was better than other facilities located on thermal neutron beams. The determination of ^{10}B was previously performed at a cold neutron beam guide by Yonezawa et al. [17], as a part of the boron neutron capture therapy (BNCT) at the Japan Atomic Energy Research Institute (JAERI). In that case, the detection limit of ^{10}B in a blood sample was 0.14 ppm. Although blood and water matrices are slightly different for boron detection using PGAA, the results demonstrate that our system is competitive. Furthermore, the technique was applied to determine boron concentration in geological samples. The results showed a good correlation with the concentration obtained by ICP techniques.

Other groups showed that PGAA was a very useful technique in medicine. As ^{10}B in human tissue can be determined non-destructively and rapidly, many applications of ^{10}B have been carried out in BNCT treatment of brain tumors [3, 17-19]. The PGA facility at SINQ is used for a different medical application. Indeed, the technique permits to measure the concentration of boron taken up by cells in a new treatment for rheumatoid arthritis. Rheumatoid arthritis is an autoimmune disease characterized by swollen and painful inflammation of the membrane (synovium) lining articular joints [20]. A recent technique is proposed to treat synoviocytes with the $^{10}B(n,\alpha)^{7}Li$ reaction, the so-called boron neutron capture synovectomy (BNCS). The aim in measuring at the PGA station is to study the kinetics of uptake by a boron compound named KBH ($K_2B_{12}H_{12}$ 94% enriched with ^{10}B) in different cells lines. Beforehand, it is necessary to establish a calibration curve using solutions of known amount of KBH in a nutritional medium. The preparation of the unknown solutions containing the cells includes several steps. First, the cells are immersed in a nutritional medium doped with KBH and placed in an incubator. Then, for different incubation periods, they are extracted from this boronated solution and mixed to the original KBH free medium. Finally, these solutions with cells are analyzed and it is possible to determine the KBH concentration incorporated by cells as a function of the incubation time. This study has already started and the PGA technique to detect boron yields promising results [21].

Acknowledgements

The present study was supported by the Swiss National Science Foundation, the Paul Scherrer Institute (PSI) and the University of Cologne. The authors would like to express their gratitude to Prof. U. Krähenbühl and J. Grimm (University of Bern) for providing the IAEA samples and to Dr. N.E.A. Crompton (PSI) for his collaboration with the medical application.

[1] Z.B. Alfassi, C. Chung (Ed.), Prompt Gamma Neutron Activation Analysis, CRC Press, Boca Raton, FL, 1995.

[2] R.B. Firestone, V.S. Shirley (Ed.), Table of Isotopes, 8th Edition, Wiley, New York, 1996.

[3] T. Kobayashi, K. Kanda, Nucl. Instr. and Meth 204 (1983) 525.

[4] M. Crittin, J. Jolie, J. Kern, S. J. Mannanal, R. Schwarzbach, Boron detection by prompt gamma-ray activation analysis (PGAA), in: B. Larsson, et al., (Eds.), Advances in Neutron Capture Therapy, Elsevier, Amsterdam, 1996, p. 343.

[5] J. Byrne, Neutrons, Nuclei and Matter, An Exploration of the Physics of Slow

Neutrons, Institute of Physics Publishing, Philadelphia, 1994.

[6] G.S. Bauer, Nucl. Instr. and Meth. B 139 (1998) 65.

[7] W. Wagner, G.S. Bauer, J. Duppich, S. Janssen, E. Lehmann, M. Lüthi, H. Spitzer, J. Neutron Res. 6 (1998) 249.

[8] M. Crittin, J. Kern, J.-L. Schenker, Nucl. Instr. and Meth. A 449 (2000) 221.

[9] R.L. Paul, J. Radioanal. Chem. 191 (1995) 245.

[10] R.L. Paul, E. A. Mackey, J. Radioanal. Chem. 181 (1994) 321.

[11] E.A. Mackey, G. E. Gordon, R. M. Lindstrom, D. L. Anderson, Anal. Chem., 64 (1992) 2366.

[12] R.M. Lindstrom, R.F. Fleming, R.L. Paul, E.A. Mackey, Proceedings of the international k_0 Users Workshop, Rijksuniversiteit Gent, 1992, p. 125.

[13] G.L. Molnár, Zs. Révay, R.L. Paul, R.M. Lindstrom, J. Radioanal. Chem. 234 (1998) 21.

[14] M. Magara, C. Yonezawa, Nucl. Instr. and Meth. A 411 (1998) 130.

[15] J.C. Miller, J.N. Miller, Statistics for Analytical Chemistry, 2nd Edition, Ellis Horwood Limited, Chichester, UK, 1988, p. 115.

[16] J. Grimm, Studien zur Bestimmung von Bor und Analyse der Isotopenverhältnisse in geochemischen Proben, Diplomarbeit Universität Bern, 2000.

[17] C. Yonezawa, H. Matsue, H. Sawahata, T. Kurosawa, M. Hoshi, Y. Ito, in: Y. Mishima (Ed.), Cancer Neutron Capture Therapy, Plenum Press, New York, 1996, p. 221.

[18] C.P.J. Raaijmakers, M. W. Konijnenberg, , L. Dewit, D. Haritz, R. Huiskamp, K. Philipp, A. Siefert, F. Stecher-Rasmussen, B.J. Mijnheer, Acta Oncologica, 34 (1995) 517.

[19] R. Rogus, O.K. Harling, I. Olmez, S. Wirdzek, Boron-10 prompt gamma analysis using a diffracted neutron beam, in Progress in B.J. Allen et al., (Eds.), Progress in Neutron Capture Therapy for Cancer, Plenum Press, New York, 1992.

[20] J.C. Yanch, S. Shortkroff, R. E. Shefer, S. Johnson, E. Binello, D. Gierga, A. G. Jones, G. Young, C. Vivieros, A. Davison, C. Sledge, Med. Phys., 26 (1999) 364.

[21] N. Stritt, Boron uptake in cells, a study about the kinetics of boron uptake in cells, neutron-induced cell death (apoptosis) and neutron-induced cell cycle arrest, Diploma-Thesis, NDS Medizin Physik ETHZ, 2001.

The k_0-method in cold-neutron prompt gamma-ray activation analysis

S. Baechler[a,b*], P. Kudejova[c], J. Jolie[c], J.-L. Schenker[a],

[a] *Physics Department, University of Fribourg, CH-1700 Fribourg, Switzerland*
[b] *Paul Scherrer Institute, CH-5232 Villigen, Switzerland*
[c] *Institut für Kernphysik, Universität zu Köln, D-50937 Köln, Germany*

The k_0-standardization method has been applied and evaluated at the cold-neutron prompt gamma-ray activation (PGA) facility of the Swiss spallation source SINQ (Paul Scherrer Institute). The k_0-factors for 26 elements of interest were measured using chlorine as a comparator. The results showed good agreement with the values determined at other cold and thermal neutron guided beams, except for a few elements.
Then, standard reference materials were analyzed to assess the accuracy of the method using the obtained k_0-factors. Finally, the technique was used for multielement determination in various samples coming from nuclear waste storage, geochemistry and geology. In addition, the non-destructive nature of PGAA offered an interesting application in archeology.

1. Introduction

Prompt gamma-ray activation analysis (PGAA) is a non-destructive nuclear technique for measuring concentrations of various elements in a sample [1]. The method consists in observing capture gamma rays emitted promptly by a target material during neutron irradiation. PGAA is an important tool for analyzing light elements such as H, B, N, Si, P, S and Cl, which are usually difficult to measure by conventional neutron activation analysis (NAA). The analytical sensitivity of an element, defined as the gamma-ray count rate of a known amount of the standard, is strongly correlated with its neutron capture cross-section that varies nearly randomly between elements (or isotopes). Due to their large cross section, PGAA is highly sensitive to toxic elements as Cd and Hg and some rare earths, especially Sm and Gd. This technique is particularly suitable for non-destructive multielement analysis of both major and trace components. For example, PGAA proved to be the most adapted technique for quantitative determination of H, B, Si, S, P, Cl, Ca, Ti, Cr, Mn, Fe and Ni in minerals [2]. The potential of PGA is optimized when using low energy

neutrons, which can be guided far from the neutron source. First, the lack of fast-neutron and gamma-ray radiation reduces drastically the background level. Furthermore, the capture reaction rate of low-energies neutrons is improved due to the 1/v capture cross section behavior. Both the lower background and the enhanced cross section give rise to a substantial improvement of analytical sensitivities and detection limits [3].

A PGA facility has been built at the end of the 1RNR12 cold neutron guide of the Swiss spallation source SINQ at the Paul Scherrer Institute [4]. The quantitative analysis was carried out using a comparative method. Element concentrations were determined by comparing the gamma-ray count rate of an element in a sample to the corresponding element sensitivity. In a previous work, the analytical sensitivities were determined for 11 elements, including H, B, N, Na, Si, S, Cl, K, Ca, Ti, and Fe [4].

However, the differences in composition and geometry between samples and standards affect the accuracy of analytical results. Indeed, neutron self-shielding and scattering effects in the target influence strongly element sensitivities. These analytical biases in the comparative standardization are largely eliminated using an internal standardization; i.e. the sensitivity for a studied element is determined relatively to that of an internal comparator [5]. This approach has been applied successfully at the SINQ PGA facility for quantitative determination of boron in aqueous solutions [6]. The relative sensitivities, namely k-factors, can be evaluated as universal constants by eliminating the detector efficiency dependence. This extension introduces the so-called prompt k_0-factors [7, 8] that can be applied in any PGA system for multielement analysis by analogy with the k_0-standardization in NAA [9, 10]. The k_0-method yields only relative concentrations of elements. Absolute concentrations require the determination of at least one element in the sample using the comparative method for PGA based on standard reference materials of similar matrix and geometry or using another analytical technique. The k_0-factors for 26 elements have been measured with the cold neutron guided beam at SINQ. The results were compared to k_0-factors determined with both cold and thermal guided neutrons at other facilities.

2. Apparatus

The PGA facility has been built at the end of the 1RNR12 cold neutron guide of the Swiss spallation source SINQ at the Paul Scherrer Institute. At SINQ, a 590 MeV protons beam impinging onto a lead target produces neutrons through the spallation process. Recently, the proton current has been upgraded to 1.3 mA. Then a fraction of the released neutrons are slowed down into a cold moderator of liquid deuterium at 25 K. Finally, cold neutrons are transported to the PGA instrument by a curved neutron guide. The mean energy of the neutron

distribution was about 3 meV. The beam size at the end of the guide is 20 mm wide and 50 mm high and the neutron flux at the sample position is about $1.8 \cdot 10^8$ n/cm^{2}s.

Prompt gamma rays were detected by a Compton-suppressed spectrometer composed of a coaxial type high-purity germanium (HPGe) main detector shielded by a 240×240 mm^2 by 250 mm long NaI(Tl)/BGO scintillator. Indeed, the prompt gamma ray spectra were greatly simplified when reducing the background continuum due to Compton scattering. Since guided cold neutron beams provide low gamma and fast-neutron background, the germanium detector was in close geometry to the target located into an aluminum chamber. A sample changer, consisting in a Teflon ladder, enabled to place six different samples. In the construction of the system, special attention was given to achieve the lowest gamma-ray background. Consequently, ^{6}LiF polymer and tiles were mainly used for neutron shielding because of their low gamma emission. The PGA facility has been described in more detail elsewhere [4].

New analysis software, namely PEGASE for Program Evaluating Gamma-ray Spectra for the determination of Elemental compositions, has been recently developed under the LabVIEW environment [11]. This program includes an automated peak fitting procedure based on the computer code GASPAN [12]. Then, the routine for elemental identification compares the resulting information to a library of neutron capture gamma rays, which combines the Evaluated Nuclear Structure Data File (ENSDF) [13] and the new gamma-ray spectrum catalog for PGAA proposed by Révay et al. [14]. Finally, relative concentrations are calculated for elements for which the corresponding k0-factor was measured and inserted into the library.

3. Experimental procedure

The k_0-factors in PGA are determined using the following equation given by Molnár et al. [8]:

$$k_{0,c}(x) = \frac{(N_{\gamma,x} / \varepsilon_{\gamma,x})}{(N_{\gamma,c} / \varepsilon_{\gamma,c})} \cdot \frac{m_c}{m_x}, \qquad (1)$$

where N_γ is the net peak area under the gamma line, ε_γ the absolute full-energy peak detection efficiency and m the mass for the element of interest x with respect to the comparator element c. The precise determination of k_0-factors mandates thus (1) an accurate calibration of the detector efficiency, (2) the selection of a suitable comparator element and (3) standard samples with accurate elemental ratios.

3.1 Gamma-ray detection efficiency curve

PGAA required a gamma-ray detection efficiency curve covering a wide energy range, i.e. from 100 keV to 11 MeV. First, the efficiency of the detector was measured between 81 keV and 1408 keV using calibrated

sources of ^{152}Eu, ^{133}Ba, ^{137}Cs and ^{60}Co recommended in the IAEA-CRP report [15]. The certified strengths of these radioactive sources were used for the calculation of the absolute efficiency curve. Then, the efficiency calibration was extended to 3548 keV measuring a ^{56}Co source produced initially by the ^{56}Fe(p,n) reaction. Data points were deduced from emission probabilities proposed in Ref. [15]. Radioactive sources cannot be used above the highest energy of the ^{56}Co source at 3548 keV. Thus, prompt neutron-capture gamma rays are used to prolong the efficiency curve. The ^{14}N(n,γ) reaction allowed an efficiency calibration up to 10829 keV with high precision intensity values [15, 16]. The target consisted of a 300-mg pill of urea CH_4N_2O was exposed 24 hours to the neutron beam. In addition, selected gamma rays of the ^{12}C(n,γ) and ^{35}Cl(n, γ) reactions proposed in Ref. [16] were used to fill in gaps in the calibration curve. For this purpose, two samples of 30 mg of chloranil C_6ClO_2 and 1.5 g of graphite were measured successively for 5 hours. Finally, 66 data points with an average uncertainty of 1.5 %, from 0.2 % to 3.4 %, were considered for the construction of the efficiency curve, obtained by least-squares

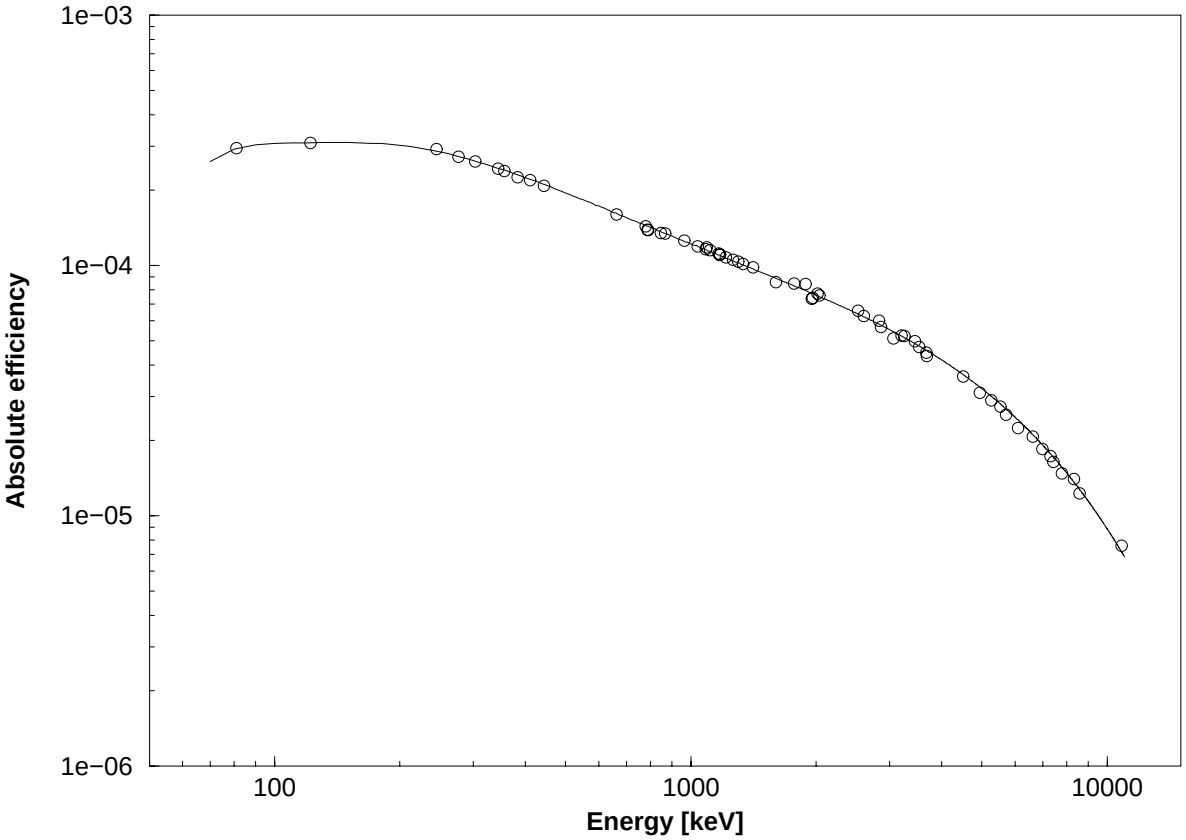

Fig.1. Absolute efficiency curve of the Compton-suppressed spectrometer at the PGA facility

fitting to the following function suggested in GASPAN:

$$\varepsilon(E) = 0.5 \cdot erfc[-a_1^{2\cdot(E-a_2)}] \cdot 10^{\sum_{i=3}^{8} a_i \cdot \log(E)^{(i-3)}} \quad (2)$$

where a_i are fitting parameters. The plot of the efficiency curve is shown in Fig. 1. The deviation between the measured and fitted values is in the order of 1.5% below 2 MeV, 2.5% between 2 MeV and 5 MeV and around 4% above 5 MeV.

3.2 Standard samples

Chloride was adopted as the internal comparator since the chloride compounds are available for a wide range of elements and offer a well-known stable stoichiometry as well as a good sample homogeneity [8]. Moreover, the $^{35}Cl(n,\gamma)$ reaction was used for detector efficiency calibration. Thus, chloride compounds were applied to measure k_0-factors of H (ammonium chloride), Na, Al, K, Ca, Cr, Mn, Fe, Co, Ni, Cu, Zn, Hg. However, for elements for which analytical sensitivities largely deviate from those of Cl, chloride compounds were replaced by appropriate mixtures of high-purity elemental compounds with ammonium chloride [17]. Then, mixed standard powder samples were prepared for elements with low sensitivity such as Si, P, S, Ti, Sn and Pb. In addition, k_0-factors of C and N, which are elements with extremely low sensitivity, were determined using H as comparator in standard samples of melamine ($C_3H_6N_6$). For each of those elements, 4 to 6 samples in the range of 10 to 1000 mg were prepared and sealed into FEP (Teflon) bags. For highly sensitive elements, i.e. B, Cd, Sm and Gd, certified standard solutions were mixed with ammonium chloride in an appropriate ratio. Then, 1ml of the prepared solutions was pipetted into Teflon vials of cylindrical shape. Finally, samples were irradiated for 0.5 to 12 hours in order to obtain sufficient statistics for the determination of photopeak areas under gamma-lines of interest. Beforehand a vacuum of a few mbar was created in the sample box in order to suppress the peaks from neutron capture in nitrogen.

4. Results and discussion

4.1 k_0-factors

The k_0-values of 26 elements related to the 1951 keV peak of chlorine are reported in Table 1 for the gamma-lines mostly appropriate to quantitative analysis. The errors corresponded to the propagated uncertainties combining counting statistics and efficiency function. Moreover, the standard deviation based on the different samples was consistent with the calculated propagated error. The errors obtained were then less 4%, except for C and N due to the low sensitivity, as well as for Fe, Ni, Cu and Pb, when considering lines above 7 MeV due to uncertainties of the efficiency curve. In this work, no effort was made to improve the accuracy of the energy values.

Table 1. Comparison of the $k_{0,Cl}$-factors measured at SINQ with those obtained at other facilities.

		This work (Cold neutrons)	IKI (Thermal neutrons)[a]		JAERI (Cold neutrons)[b]	
El	E_γ [keV]	$k_{0,Cl}$ ± Error	$k_{0,Cl}$ ± Error	dev. [σ]	$K_{0,Cl}$ ± error	dev. [σ]
H	2223	1.88 ± 0.06	1.80 ± 0.02	1.2	1.86 ± 0.06	0.2
B	478	349 ± 8	360 ± 3	1.2	380 ± 32	0.9
C	4945	0.00132 ± 0.00008[c]	0.00123 ± 0.00004	1.1		
C	1262	0.000626 ± 0.000034[c]	0.000558 ± 0.000016	1.8	0.000643 ± 0.000031	0.4
N	1885	0.00583 ± 0.00027[c]	0.00565 ± 0.00009	0.6	0.00698 ± 0.00032	2.7
Na	472	0.109 ± 0.003	0.118 ± 0.002	2.6	0.1162 ± 0.0003	2.7
Al	1779	0.0492 ± 0.0017	0.0472 ± 0.0007	1.1	0.0433 ± 0.0014	2.7
Si	3539	0.0211 ± 0.0007	0.0230 ± 0.0004	2.3	0.0211 ± 0.0001	0.0
P	637	0.00536 ± 0.00014	0.00545 ± 0.00028	0.3	0.00477 ± 0.00008	3.7
S	841	0.0571 ± 0.0014	0.0607 ± 0.0012	1.9	0.0573 ± 0.0012	0.1
Cl	1165	1.42 ± 0.04	1.41 ± 0.02	0.1		
K	770	0.130 ± 0.003	0.127 ± 0.002	0.7	0.128 ± 0.004	0.4
Ca	1942	0.0496 ± 0.0017	0.0464 ± 0.0015	1.4		
Ti	1381	0.581 ± 0.017	0.590 ± 0.015	0.4	0.591 ± 0.006	0.5
Ti	984	0.0125 ± 0.0005	0.0130 ± 0.0002	1.0		
Cr	749	0.0578 ± 0.0020	0.0598 ± 0.0013	0.8		
Cr	834	0.142 ± 0.004	0.145 ± 0.004	0.5	0.142 ± 0.005	0.0
Mn	314	0.144 ± 0.004			0.149 ± 0.008	0.6
Fe	7631	0.0630 ± 0.0032	0.0673 ± 0.0014	1.2	0.0559 ± 0.0027	1.7
Fe	352	0.0282 ± 0.0009	0.0221 ± 0.0011	4.3	0.0269 ± 0.0011	0.9
Co	230	0.638 ± 0.016	0.664 ± 0.010	1.4		
Co	555	0.510 ± 0.013	0.275 ± 0.004	16.7	0.509 ± 0.020	0.0
Ni	8998	0.131 ± 0.006	0.138 ± 0.003	1.1		
Ni	465	0.0727 ± 0.0018	0.0783 ± 0.0017	2.2	0.0811 ± 0.0028	2.5
Cu	7915	0.0714 ± 0.0037	0.0808 ± 0.0018	2.3		
Cu	278	0.0725 ± 0.0018	0.0830 ± 0.0018	4.1	0.0762 ± 0.0025	1.2
Cu	186	0.0204 ± 0.0006	0.0227 ± 0.0007	2.5		
Zn	1077	0.0297 ± 0.0011	0.0308 ± 0.0005	0.9		
Zn	115	0.0132 ± 0.0004	0.0140 ± 0.0004	1.3		
Cd	558	68.4 ± 1.7	90.5 ± 1.7	9.3	62.0 ± 1.5	2.8
Sn	1293	0.00541 ± 0.00017	0.00616 ± 0.00011	3.7		
Sn	1230	0.00289 ± 0.00010	0.00310 ± 0.00007	1.8		
Sm	334	146 ± 4	174 ± 3	6.2	116 ± 1	8.2
Sm	737	18.4 ± 0.6	21.8 ± 0.3	4.6		
Gd	1187	93 ± 3	109 ± 7	2.3		
Gd	182	234 ± 6			214 ± 1	3.4
Hg	368	6.40 ± 0.16	1.44 ± 0.06	28.7	7.00 ± 0.24	2.1
Pb	7368	0.00384 ± 0.00019	0.00360 ± 0.00009	1.1	0.00329 ± 0.00003	2.8

a) ref. 14 b) Ref. 14 & 18 c) Values were converted from $k_{0,H}$

The $k_{0,Cl}$-factors measured at SINQ were then compared with the values obtained at the Institute of Isotopes (IKI) in Hungary using thermal guided neutrons [14]. The two set of k_0-factors are in good agreement as demonstrated by the differences of both results being within two combined standard deviations (2σ) for most of elements. The combined standard deviation σ was derived from both k_0-factor uncertainties. The large deviation for Cd, Sm and Gd was expected because the k_0-method assume that the neutron capture cross sections of the elements follow the "1/v" law. Thus, the results for non "1/v" nature elements depend on the energy distribution (spectrum) of the neutron beam. On the other hand, strong differences were found for one line of Fe (352 keV) and Co (555 keV) and above all for Hg (368 keV).

These unexpected discrepancies were not confirmed when comparing our results with the k_0-factors measured at the Japan Atomic Energy Research Institute (JAERI) using thermal and cold guided neutrons [17, 18]. Only the k_0-values obtained with cold neutrons are reported in Table 1, because those measured with thermal neutrons agreed to within 3 % for most of the elements, except for C, and non "1/v" behavior elements, i.e. Cd and Sm. The $k_{0,Cl}$-factors obtained at SINQ agreed to within only one combined standard deviation (1σ) for H, B, C, Si, S, K, Ti, Cr, Mn, Fe and Co, including the 352 keV of Fe and the 555 keV of Co, with those obtained at JAERI. The difference of both reported k_0-values exceeded 3σ for Sm and Gd, as expected, but also for N and P, probably due to the low analytical sensitivities.

4.2 Application to reference materials

The method has been evaluated with multielement analysis of standard reference materials (SRM) such as estuarine sediment (NIST SRM1646a) and coal fly ash (NIST SRM1633b). The analytical results given in Table 2 are based on the measurements of 5 samples with different masses, in the range of 0.2 to 1.0 gram, with duration of about 6 hours. The certified value of the most abundant element, namely Si in both reference materials, has been used for normalization to obtain absolute concentrations.

The error values, calculated by the one standard deviation of the 5 samples, were less than 3% except for Cd and Sm in the estuarine sediment, as well as S, Cd and Gd in the coal fly ash. The results for the estuarine sediment obtained at SINQ agreed with the certified values within one combined standard deviation (1σ), except for Al and Fe which exceeded 2σ. The elemental concentrations for the coal fly ash are also in good agreement within 2σ, except for Al. In other word, the results for both materials agreed with the certified values within a relative variation of 7%.

Table 2. Analytical results of standard reference materials

Element		Estuarine Sediment (NIST SRM 1646a)		Coal Fly Ash (NIST SRM 1633b)	
		This work (n = 5) Av. ± Error	Certified value	This work (n = 5) Av. ± error	Certified value
B	µg/g	41.8 ± 1.1		74.8 ± 1.3	
Al	%	2.14 ± 0.050	2.297 ± 0.018	14.25 ± 0.050	15.05 ± 0.27
Si	%	40.00 [a]	40.00 ± 0.16	23.02 [a]	23.02 ± 0.08
S	%	0.347 ± 0.010	0.352 ± 0.004	0.193 ± 0.020	0.2075 ± 0.0011
Cl	%	0.636 ± 0.0082			
K	%	0.838 ± 0.020	0.864 ± 0.016	1.89 ± 0.034	1.95 ± 0.03
Ca	%	0.516 ± 0.0039	0.519 ± 0.020	1.41 ± 0.030	1.51 0.06
Ti	%	0.473 ± 0.010	0.456 ± 0.021	0.791 ± 0.0094	0.791 ± 0.014
Fe	%	1.86 ± 0.048	2.008 ± 0.039	7.25 ± 0.12	7.78 ± 0.23
Cd	µg/g	0.150 ± 0.023	0.148 ± 0.007	0.806 ± 0.043	0.784 ± 0.006
Sm	µg/g	2.45 ± 0.11		14.5 ± 0.32	20 [b]
Gd	µg/g	2.64 ± 0.078		17.7 ± 0.67	13 [b]

a) Analytical results are normalized for the certified Si value

b) Noncertified value

5. Examples of application

The k_0-factors measured at SINQ were applied to analytical measurements of samples coming from different fields. A useful application of the technique was found with respect to storage of radioactive waste. Several ashes, resulting from burnable waste from the Swiss nuclear power plants, medicine, industry and research, were investigated by PGAA for multi-elements analysis [20]. Indeed, the Swiss regulations require to specify not only the radioactive nuclides, but also the main inactive components of waste packages, i.e. ashes solidified with cement in drums, with respect to storage. Most analytical methods like ICP-OES, ICP-MS and ion chromatography require the total dissolution of the material. Due to the radioactivity and the main inactive components, the samples have to be diluted to be below the activity limits allowed in a non-radioactive laboratory and to avoid contamination of the apparatus by the inactive main components. Since the composition of the ashes varies quite a lot in dependence of the waste even the dissolution procedure may not work in any case. The PGAA technique offered a good possibility to circumvent these difficulties. Various ash samples were encapsulated in Teflon vials and measured directly without further preparation during 6 hours irradiation time. The concentrations of 20 elements, i.e. B, Na, Al, Si, P, S, Cl, K, Ca, Ti, Cr, Mn, Fe, Co, Ni, Cu, Zn, Cd, Sm and

Gd, were obtained with errors mostly less than 10%. The calculated total mass of the relative amounts of the pure elements converted to absolute masses of the corresponding oxides approaches 100% of the sample weight, thus showing the completeness of the analytical results.

The method was also used to determine major components, namely Cu, Zn, Sn and Pb, of several archeological objects. Similar investigations were previously realized by Glascock et al. [20] and Kasztovszky et al. [21]. The present study covered 53 La Tène and Roman brooches and one Roman pin from Western Switzerland. While selecting the material for the study, care was taken to make it representative in respect of chronology and typology. Therefore there were mainly selected brooch types matching chronologically periods extending from the late La Tène period until the end of the Roman period (from 120 BC to 380 AD). Next, from among various brooch types, the ones that had already been studied within other research projects were selected. In several cases, the examination included brooches imported to the territory of Western Switzerland.

As a result of the PGA study, it was possible to identify four different copper-based alloys: bronze (Cu 84.1-90.9%, Sn 6.9-15.8%, Zn 2.0-5.2%), leaded bronze (Cu 72.2-78.7%, Sn 7.4-15.9%, Zn 2.2-2.7%, Pb 6.5-16.8%), brass/gunmetal (Cu 72.3-86.4%, Zn 5.1-24.5%, Sn 0.4-8.5%) and leaded brass (Cu 73.4-75.4%, Zn 9.1-13.1%, Sn 3.2-6.9%, Pb 8.2-11.5%). One brooch was made of tinned lead (Pb 55.8%, Sn 29.5%, Cu 13.0%, Zn 1.7%), which was noted here as a curiosity. The preliminary analysis of the results allows for stating that bronze was the material of the La Tène brooches and brooches typical for Germanic region, found on the territory of Western Switzerland. Leaded bronze was mainly used for production of late Roman brooches and typically German ones. The lead content found in the case of one early Roman disc brooch could result from the application of enamel in the decoration, and requires a repetition of the analysis with a surface method. Vast majority of Roman brooches (including the pin) was made of brass. The occurrence, in three cases, of a large content of lead in the brass could point to the application of specific decorative techniques and calls for repetition of the analysis, as in the case of leaded bronze brooches. Detailed analysis of the results at the vast comparative background, using statistical methods, will definitely allow for formulation of more precise conclusions concerning the characteristics of particular alloys, and assigning them chronological value, especially in the typological aspect. These problems will be the subject of a larger study in the near future.

Besides, the method was used to determine major, minor and trace elements in different geological and environmental powder samples, with particular interest for accurate determination of B, which is difficult to measure by other analytical technique [22].

Boron concentration was also determined within samples from graphite reactor (< 1 μg/g), with respect to the project of a graphite-moderated pulsed spallation ultra-cold neutron source at PSI [23]. Otherwise, hydrogen is also of interest for PGAA because reliable techniques for measuring it are few. Thus, the method has been recently applied to determine low-level hydrogen, down to 30 μg/g, in high-TC superconductor YBaCuO crystals to study hydration effects.

6. Conclusions

The k_0-factors of 26 elements were determined using chlorine as comparator from measurements of stoichiometric compounds, homogenous mixtures and standard solutions with the cold neutron guided beam at SINQ. The measured k_0-factors were then compared with reported value from other neutron beam facilities and are generally in good agreement. Furthermore, the established method has been successfully applied to standard reference materials with accuracy better than 6%. Finally, PGAA has proved to be a useful tool for multielement analysis of a wide variety of samples in radioactive waste storage and geology. In addition, the technique offered a non-destructive capability for measuring chemical compositions of archeological samples. In a previous paper, elemental mapping of a sample coming from a natural reactor was carried out using a neutron lens to upgrade PGAA to a position sensitive technique [24]. For that study, more emphasis was given to qualitative than quantitative results. Indeed, at that time, the internal standard method has been applied using k_0-factors calculated theoretically from available data library that were often unreliable. Therefore, the k_0-database that was established in this work gives the opportunity to perform analogous measurements with more precise quantitative results.

Acknowledgements

This work was supported by the Swiss National Science Foundation, the Paul Scherrer Institute (PSI) and the University of Cologne. The authors wish to express their gratitude to the archeologists A. Mazur and K. Mazur for their precious collaboration, Dr. L. Genilloud for his help during brooches measurements, as well as the directors of the different museums for lending the objects. Also the authors would like to acknowledge H.-F. Beer and P. Zimmermann for their cooperation with inspection of radioactive ashes.

[1] Z. B. Alfassi, C. Chung (Ed.), Prompt Gamma Neutron Activation Analysis, CRC Press, Boca Raton, Florida, 1995.

[2] G. L. Molnár, R. M. Lindstrom, Nuclear reaction prompt gamma-ray analysis, in: Vértes et al. (Eds.), Nuclear Methods in

Mineralogy and Geology: Techniques and Applications, Plenum Press, New-York, 1998, p. 145.

[3] R. M. Lindstrom, C. Yonezawa, in: Prompt Gamma Neutron Activation Analysis, Z. B. Alfassi and C. Chung (Eds), CRC Press, Boca Raton, Florida, 1995, p. 93.

[4] M. Crittin, J. Kern, J.-L. Schenker, Nucl. Instr. and Meth. A 449 (2000) 221.

[5] R. L. Paul, J. Radioanal. Chem. 191 (1995) 245.

[6] S. Baechler, P. Kudejova, J. Jolie, J.-L. Schenker, Prompt gamma ray activation analysis for determination of boron in aqueous solutions, accepted for puplication in Nucl. Instr. And Meth. A (2002).

[7] R. M. Lindstrom, R. F. Fleming, R. L. Paul, E. A. Mackey, Proc. Intern. k_0 Users Workshop, Rijksuniversiteit Gent, 1992, p.125.

[8] Molnár, G. L., Zs. Révay, R. L. Paul, R. M. Lindstrom, J. Radioanal. Chem. 234 (1998) 21.

[9] A. Simonits, F. De Corte, J. Hoste, J. Radioanal. Ghem., 24 (1975) 31.

[10] F. De Corte, A. Simonits, A. DE Wispelaere, A. Elek, J. Radioanal. Nucl. Chem., 133 (1989) 3.

[11] L. Genilloud, PEGASE. Program evaluating gamma-ray spectra for the determination of elemental compositions. Internal Report IFP-PAN, University of Fribourg, Switzerland, 2000.

[12] F. Riess, Annual Report, Munich Tandem-Accelerator-Laboratory, 1991, p.168.

[13] Evaluated Nuclear Structure Data File (ENSDF), National Nuclear Data Center, Brookhaven National Laboratory; http://www.nndc.bnl.gov/nndc/endf/

[14] ZS. Révay, G.L. Molnár, T. Belgya, ZS. Kasztovszky, R.B. Firestone, J. Radioanal. Chem. 244 (2000) 383.

[15] X-ray and gamma-ray standards for detector calibration, IAEA-TECDOC-619, International Atomic Energy Agency, Vienna, 1991.

[16] S. Raman, C. Yonezawa, H. Matsue, H. Iimura, N. Shinohara, Nucl. Instr. and Meth. A 454 (2000) 389.

[17] H. Matsue, C. Yonezawa, J. Radioanal. Nucl. Chem., 245 (2000) 189.

[18] H. Matsue, C. Yonezawa, J. Radioanal. Nucl. Chem., 249 (2001) 11.

[19] S. Baechler et al., Labor für Radio- und Umweltchemie der Universität Bern und des Paul Scherrer Instituts, Annual Report 2001 p. 33.

[20] M.D. Glascock, M.F. Corman, Radiochem. Radioanal. Lett., 57/2 (1993) 73.

[21] ZS. Kasztovszky, Zs. Révay, T. Belgya, G.L. Molnár, J. Radioanal. Nucl. Chem., 244 (2000) 379.

[22] J. Grimm, Studien zur Bestimmung von Bor und Analyse der Isotopenverhältnisse in geochemischen Proben, Diplomarbeit Universität Bern, 2000.

[23] K. Kirch, a graphite-moderated pulsed spallation ultra-cold neutron source, submitted to Nucl. Instr. and Meth. A (2001).

[24] S. Baechler et al., J. Radioanal. Nucl. Chem., 250 (2001) 39.

Non-destructive analysis of a bulky sample from a natural fossil reactor

S. Baechler [a], Th. Materna [a] , J. Jolie [a] , P. Cauwels [b], M. Crittin [a], V. Honkimaki [c], H.U. Johner [d], B. Masschaele [b], W. Mondelaers [b], J. Kern [a], M. Piboule [e]

[a] *Institute of Physics, University of Fribourg, CH-1700 Fribourg, Switzerland*
[b] *Vakgroep Subatomaire en Stralingsfysika, Ghent University, B-9000 Gent, Belgium*
[c] *European Synchrotron Radiation Facility, PB 220, F-38043 Grenoble CEDEX, France*
[d] *Section of Environmental Radioactivity, CH-1700 Fribourg, Switzerland*
[e] *Institute Dolomieu, University Joseph Fourier Grenoble I, F-38043 Grenoble, France*

Two non-destructive and position sensitive methods were used to analyze a sample coming from the reactor site of Okelobondo near Oklo (Gabon). At the European Synchrotron Radiation Facility (ESRF), uranium and lead were visualized in this piece by element sensitive tomography. The same sample was then studied with the new prompt gamma activation (PGA) facility at the Swiss spallation neutron source SINQ (PSI Villigen). A neutron focusing capillary lens permits to upgrade PGA to a position sensitive method. In the Oklo sample the concentration of uranium but also of 7 other elements were spatially analyzed.

1. Introduction

In a region of Gabon, Oklo, natural nuclear reactors operated two billion years ago [1]. During their active period, these reactors produced radioactive waste products. They form the unique opportunity to study the diffusion of radioactive elements over a time scale of billions of years. The discovery of the natural nuclear reactors at Oklo ensued from routine measurements of uranium ores revealing a depletion of one percent in the relative abundance of ^{235}U, the fissile isotope used in nuclear stations. The most important reason why nuclear fission started two billion years ago is the high 3% relative abundance of ^{235}U in natural uranium at that moment. Because ^{235}U decays faster than ^{238}U, the present ratio of 0.72% does not permit natural fission to occur any more. At Oklo, not only the starting of a spontaneous fission is amazing but also the natural self-control of this phenomenon. Indeed, water acted as the moderator and limited the reactivity of the

core. The depletion of neutron absorbers such as boron compensated the burnup of ^{235}U. A natural reactor required two more conditions: a high density of uranium and a critical size [2, 3].

A sample coming from the reactor of Okelobondo, an extended area of the Oklo site, was analyzed by two non-destructive and position sensitive methods. At the European Synchrotron Radiation Facility (ESRF, Grenoble, France), the sample was imaged in three dimensions in order to retrieve the spatial distribution of uranium and lead, using a dichromatic tomography with synchrotron radiation. The spatial resolution was of the order of 100 μm. The same ore was studied by cold neutron capture at the new prompt gamma activation facility at the Swiss spallation neutron source SINQ (PSI, Villigen, Switzerland). Prompt gamma activation analysis (PGAA) was turned into a position-sensitive method using a neutron capillary lens. The uranium distribution retrieved by dual energy tomography permitted to normalize the PGAA data. Thus, elemental concentration maps of the sample with a spatial resolution of 1 mm were obtained.

2. Dichromatic tomography with synchrotron radiation

The concept of dichromatic tomography, also known as element sensitive tomography, is to measure the attenuation at several orientations of a sample with photons having an energy first just below and then just above the K-edge of the element of interest [4, 5]. The recorded patterns are used to reconstruct the three-dimensional attenuation distribution in the sample. The K-edge causes an abrupt increase of absorption of photons by an element. The difference between both distributions, yields the three-dimensional concentration of the element under study. Because the K-edge energy is characteristic of an element, the method can be applied to identify any element in an unknown matrix. An important property of this technique is that it yields directly the concentration of the element under study. With the advent of 3rd generation synchrotron radiation sources producing photons with energies above 100 keV, element sensitive scanning is possible for the actinides [6]. The set-up of the experiment at the high-energy beamline ID15a of the ESRF is illustrated in Fig. 1. A wavelength shifter was chosen to produce the X-ray beam. This device permits to produce high-energy photons (from 30 keV to 1000 keV). Two bent asymmetric-cut Si crystals working in fixed Laue-Laue mode selected the chosen energy, about 60 meters from the source. Two energies close to the K-edge of the element under study were chosen to perform the tomographies: 114.6 and 116.6 keV for uranium, 87 and 89 keV for lead with an energy spread of 250 eV.

The monochromatic beam then passed through a vacuum tube in order to avoid scattering of the X-rays by air. The sample was placed on a rotation table. At the sample

position, the beam was 5 mm high and 20 mm wide with an intensity of about 10^8 photons/s/mm^2. Finally, the detection system was placed at the end of the set-up to record the absorption images of the sample at 200 different rotation angles, equally distributed over 180°. A double scan for the Oklo sample took about 4 hours. Because of the thickness and the material of this sample, a high contrast in the absorption patterns between the inner part of the piece and the outside was observed. These effects, which cause artifacts in the reconstruction, were avoided placing wedge shaped copper masks (attenuation pieces) in front of the sample.

The detector, based on a converter and a charge coupled device (CCD) camera, is shown on the Fig. 2. The converter consisted of a powder phosphor screen, a 80 μm Gd_2O_2S:Tb layer, converting X-ray to visible light. The converter was imaged using a 1:1 optical lens, a 45°-mirror and a CCD camera. The mirror was used to keep the camera out of the direct beam. In addition, a lead glass was placed between the mirror and the camera, to protect the CCD from scattered photons. The CCD, Peltier cooled to reduce electronic background, had a sensitive area of 24.6×24.6 mm^2 covered by 1024×1024 pixels, a dynamic range of 14 bits (6384 grey-levels per pixel) and a read-out time of about 5 seconds.

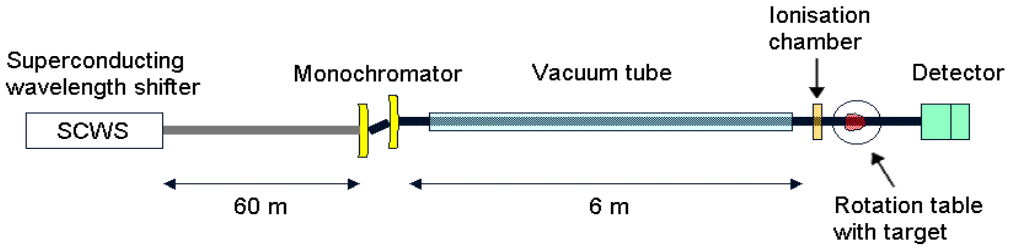

Fig. 1. The high-energy tomography set-up at ESRF.

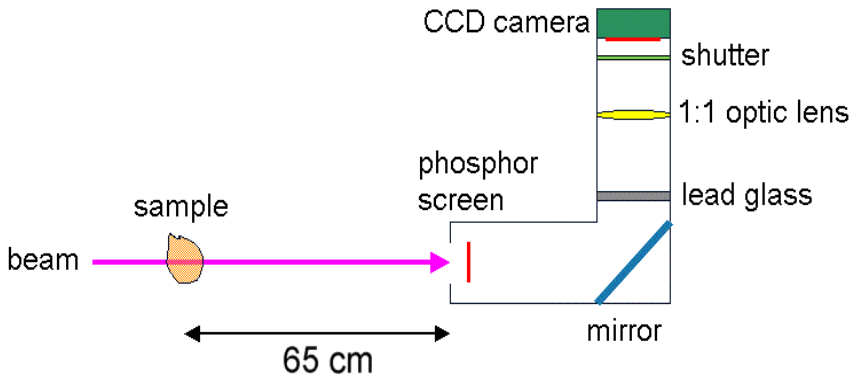

Fig. 2. The detector system based on a CCD camera and a phosphorescent screen.

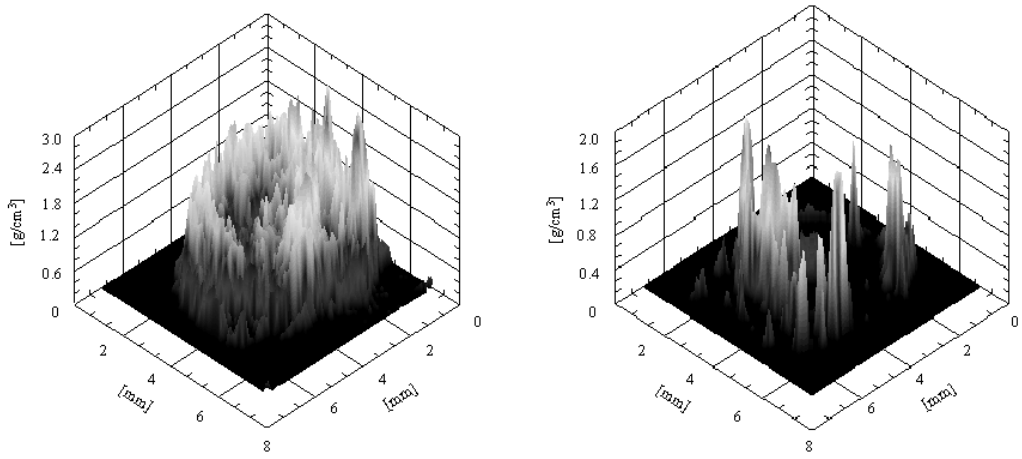

Fig. 3. The uranium distributions (in g/cm^3) in two horizontal slices taken in the lower (on the left) and upper (on the right) part of the sample.

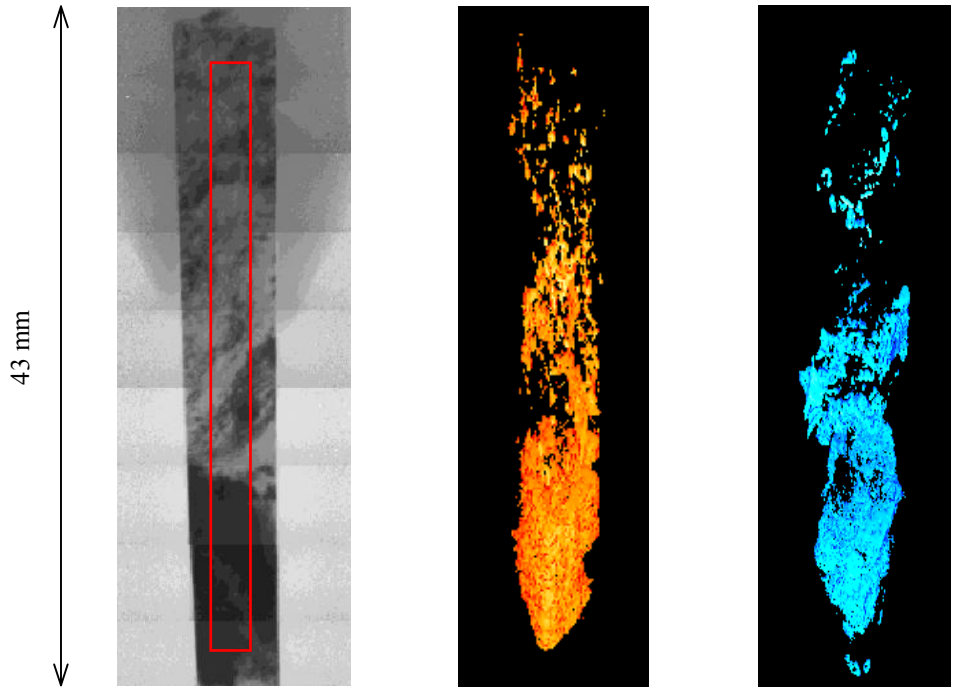

Fig. 4. On the left, radiograph of the Oklo sample with synchrotron radiation at 87 keV. The rectangle indicates the measurement positions for the PGAA. Iso-surfaces of uranium in the middle and lead on the right (surface U > 1 g/cm^3; surface Pb > 0.4 g/ cm^3).

The choice of the converter thickness came to a compromise between reducing light scattering in the converter and keeping a sufficient detective quantum efficiency. With this detection system, the spatial resolution was about 25 µm. However, the use of 4×4 binning, which consisted in bringing 16 pixels together on the CCD, raised the spatial

resolution to 100 μm. The binning was performed to decrease the exposure time.

The reconstruction method was based on a filtered back-projection with the Sheep-Logan filter, also used in computer tomography (CT) or positron emission tomography (PET). A package based on Labview and MS Visual C++ [7] was developed to perform the data analysis and reconstruction. Procedures to remove ring artifacts and white spots were also implemented. An IDL software package was used to visualize density surfaces.

Fig. 3 compares the uranium distributions in two horizontal slices taken in the upper and lower part and of the sample. Fig. 4 shows a single radiograph of the sample using 87 keV photons and two iso-density surfaces showing the results for the uranium and lead distributions in the sample.

3. Prompt gamma activation analysis

Prompt gamma activation analysis (PGAA) is a non-destructive technique to identify elements and determine their concentration in a sample [8,9]. In the traditional neutron activation analysis (NAA), gamma-rays emitted following beta-decay are measured after irradiation by a neutron beam. With the PGA method, prompt gamma-rays following neutron capture are observed during irradiation by a Compton-suppressed spectrometer or a pair spectrometer. Because the neutron capture cross-section varies strongly from element to element, the method is very sensitive to certain elements, e.g. H, B and rare-earth elements and very insensitive to others, e.g. Be and Pb. The standard procedure for PGAA consists in irradiating the whole sample by the neutron beam and returning the elemental concentration without any spatial information. A neutron focusing lens, designed for the available neutron beam characteristics, permitted the PGAA to be upgraded to a position sensitive method. By scanning the sample with the 1 mm focal spot, a two-dimensional elemental mapping was achieved. This method reveals the presence of many elements at once.

A PGA facility was installed at the end of the 1RNR12 cold neutron guide of the Swiss spallation source SINQ at PSI (Villigen, Switzerland) [10,11]. At SINQ, neutrons are created following a spallation reaction [12]: a heavy metal target, e.g. lead, is exposed to a high energy proton beam, producing neutrons. Then, the neutrons velocity is slowed down by cooling them in –250°C liquid D_2. Cold neutrons, which have a large wavelength, are transported using neutrons guides by total reflection. The new PGA facility used neutrons having a maximum wavelength of 0.35 nm with an asymmetric distribution. This neutron beam scans the sample, which is placed in a target chamber. Finally, gamma-rays are detected by the Compton-suppressed spectrometer, which is composed of a central Ge detector in a 240×240 mm^2 by 250 mm long NaI(Tl)/BGO scintillator. The pair spectrometer, which consists of a 25 cm^3 Ge

detector placed inside the central hole of a cylindrical NaI(Tl) scintillator optically divided into six slices, was not used for these measurements because of its low efficiency. The neutron focusing lens was placed between the end of the guide and the sample (Fig. 5). This neutron lens [13, 14] is composed of a large number of polycapillary fibers, parallel at the lens entrance and bent converging on a focal spot. Each fiber is composed of an array of microscopic channels which are perfectly parallel within each glass fiber. After completing multiple total reflections along the interior surfaces of the channels, neutrons are focused. The focal spot was about 1 mm in diameter. In front of the sample, a ^{6}LiF collimator of 1 mm in diameter was placed to absorb unfocalized neutrons. Finally, the detectors are shielded against neutrons and direct gamma-radiation. The new PGAA facility is described in more detail elsewhere [10,11].

The part of the sample outlined by the rectangle on the radiography of Fig. 4 was scanned in the vertical and horizontal directions. A prompt gamma-ray spectrum was obtained for each position. Elemental identification was performed by γ-spectroscopy, based on the Evaluated Nuclear Structure Data File, ENSDF. The spectrum analysis was carried out using the fitting software Picread [15], developed on Labview (Fig. 6).

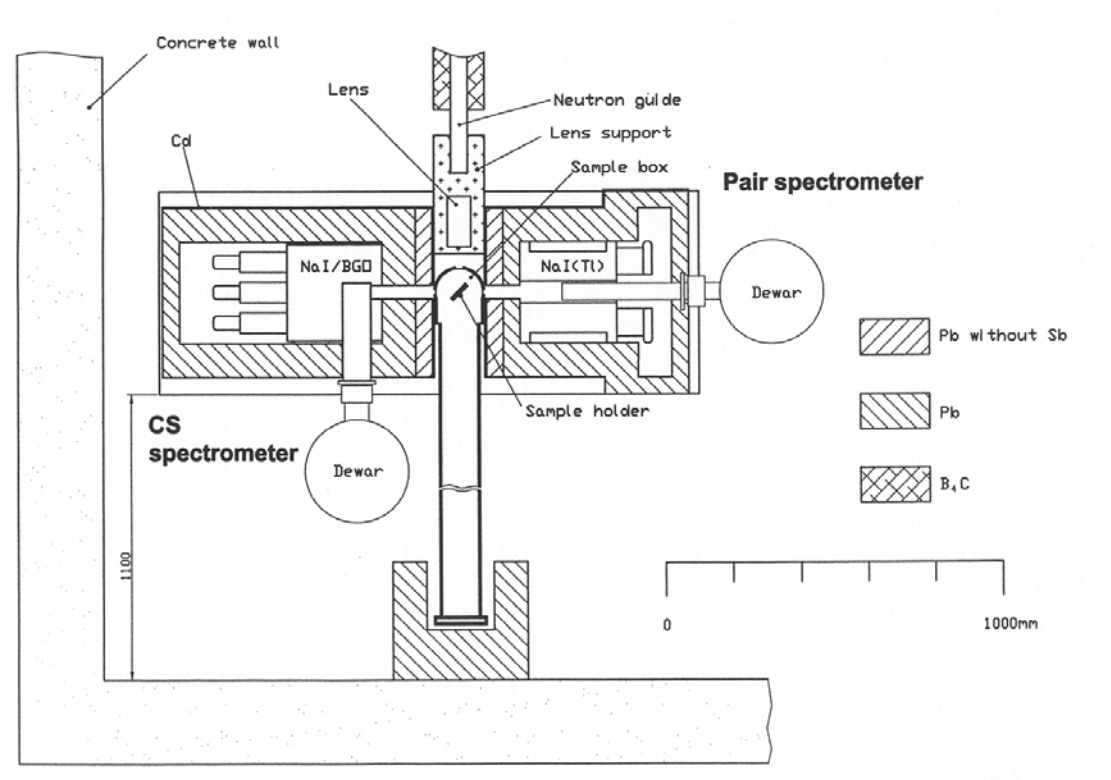

Fig. 5 Horizontal cut of the new prompt gamma activation facility at the Swiss spallation neutron source SINQ

The peak area A_x of energy E_γ from element x in the spectrum is given by:

$$A_{x,E_\gamma} = \frac{N_0 m_x}{M_x} \varepsilon(E_{\gamma,x}) \theta_x \Gamma_{x,E_\gamma} t_i \Phi_n \sigma_x \qquad (1)$$

where No is Avogadro's number, m_x is the mass of the element x, M_x is the atomic weight, $\varepsilon(E_{\gamma,x})$ is the counting efficiency, θ_x is the abundance of the capturing isotope, Γ_x is the γ-yield in photons per neutron capture, t_i is the irradiation time, Φ_n is the neutron flux and σ_x is the cold capture cross section. To reduce the effects of neutron scattering and absorption to a large extent and as the neutron flux coming out of the lens was not so well known, element ratios were analyzed instead of absolute masses m_x [16]. For almost all elements the law $\sigma = \sigma_0 \cdot v_0/v$, where v_0 is the thermal neutron velocity and σ_0 is the thermal capture cross section, is valid. Normalizing the peak area of element x to the peak area of a monitor element s, the following ratio was obtained:

$$\frac{m_x}{m_s} = \frac{\dfrac{M_x A_x}{\theta_x \Gamma_x \sigma_{0,x} \varepsilon_{\gamma,x}}}{\dfrac{M_s A_s}{\theta_s \Gamma_s \sigma_{0,s} \varepsilon_{\gamma,s}}} \qquad (2)$$

The monitor element used was uranium, because the spatial distribution of this element was already determined by dichromatic tomography (see above). The self absorption of the gamma-rays in the sample was not negligible because of the content and the heterogeneity in the Oklo sample. Due to the Z^5 dependence of the photoelectric cross section, this effect was strongly dominated by uranium and lead. Thus, using the ESRF data, the shape of the γ-ray efficiency versus energy curve was modified depending on the irradiation position After the evaluation of concentrations of the studied element at different positions, a distribution map was produced using Microsoft Excel 97 (Fig. 7).

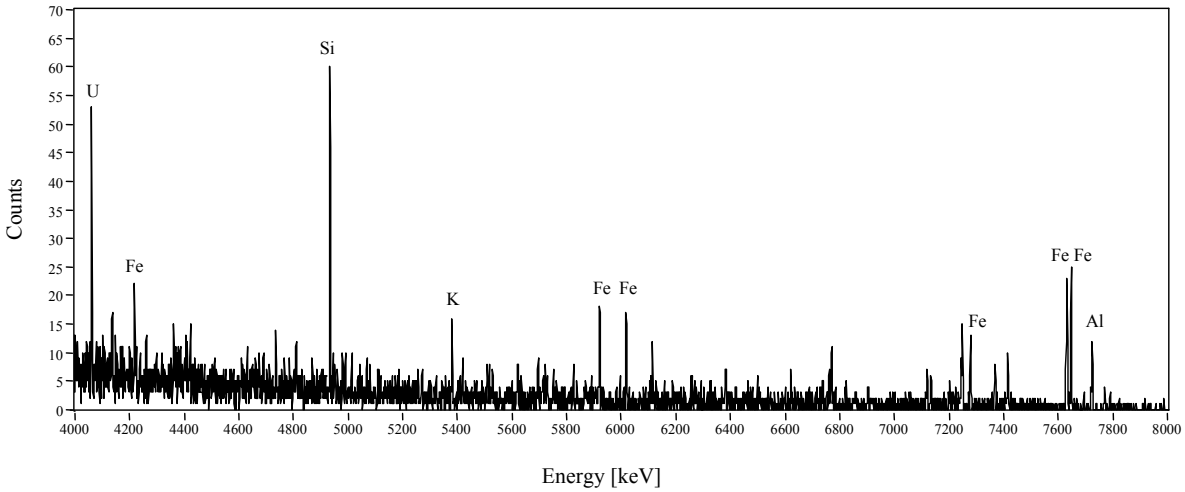

Fig. 6. Typical gamma-ray spectrum from 4.0 to 8.0 MeV obtained by prompt gamma activation of the Oklo sample.

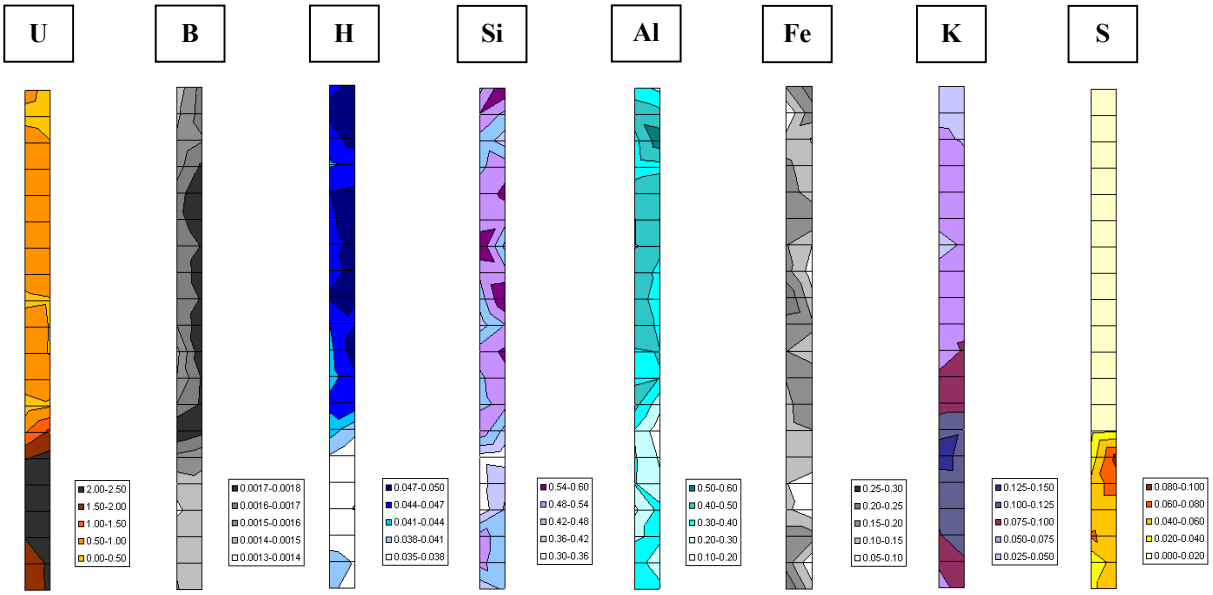

Fig. 7. Spatial distribution (in g/cm^3) of different elements from the prompt gamma activation analysis

4. Results and discussion

The studied sample from the Okelobondo reactor is composed of clay with a high uranite content. The dimensions of this sample are $5.3 \times 6.8 \times 43$ mm^3 and the mass is 4.987 g. Both methods yield a high uranium density in the lower part of the sample (Figs. 4 and 7). This part comes indeed from the core of the reactor. Since the operation of the reactor, two-billion-years old ago, a fraction of uranium decayed in stable isotopes of lead. The analysis revealed the presence of lead where the uranium concentration is the highest. The spatial distributions of silicon and aluminium confirm the presence of clay in the center of the reactor (Fig. 7). Boron and hydrogen are present in the clay and show a similar spatial distributions as the silicon and aluminium. The lower concentration of boron and hydrogen in the core is due to the high uranium density. Potassium and sulfur are present in the part of the piece containing high uranium concentration. Comparison between the Pb distribution obtained in Fig 4 and the S distribution from PGAA clearly confirm the presence of galena (PbS) which is consistent with geological analysis. In fact the correlation of lead seems to be stronger with the potassium than with the uranium. Unfortunately the PGAA technique is very insensitive to lead which does not allow for a direct test of this observation using Fig. 7. The distribution of potassium in the sample is more surprising, because at first glance one would expect to find it correlated to the clay. Supposing that its distribution is related to a late hydration with respect to the operation of the reactor, the distribution should be related to K-phyllites which are correlated to the galena distribution.

5. Conclusions

The present study shows that both non-destructive methods yield complementary results. By dichromatic tomography using synchrotron radiation, diffusion processes of uranium, which are important for nuclear waste storage, can be studied with a good resolution (100 μm). The distribution of lead, another heavy element, was also visualized. High-energy tomography could be a useful tool for geology. Indeed, the high energy combined with a high photon flux is an asset for large and dense samples containing actinides.

The prompt gamma activation using a lens yields concentration maps of many elements at once. In other words, this technique is not only element sensitive, but also position sensitive. The uranium distribution retrieved by dichromatic tomography was used as a monitor element to determine the concentration of other elements found in the Oklo sample. Using element ratios, analytical bias due to neutron scattering and absorption in cold prompt gamma activation analysis was minimized. The results show that PGAA is a powerful method to determine concentration of H, B, Si, Al, S, Fe, K which are elements of general geological interest in very dense samples in a non-destructive way.

The study shows that it is possible to determine the concentration of several elements in bulky and highly radioactive samples using synchrotron radiation and neutrons. This work thus opens the way for new methods for instance to investigate man-made radioactive waste without a risk of contamination.

Acknowledgements

This research was supported by the Swiss National Science Foundation, PSI, ESRF and by the Research Board of the Rijksuniversiteit Gent. The authors would like to thank Dr. Nicolas Stritt of the University of Fribourg for his help during computing analysis

.

[1] R. Bodu, H. Bouzigues, N. Morin, J.-P. Pfiffelmann, 1972 Compt. Rend D 275 1731.

[2] P.-L. Blanc, F. Gauthier-Lafaye, E. Ledoux, Pour la science, 237 (Juillet 1997).

[3] Western Australian Isotope Science Research Centre, Natural Fossil Fission Reactors; http://www.curtin.edu.au/curtin/centre/waisrc/OKLO/index.shtml.

[4] M. Bertschy, J. Jolie, W. Mondelaers, Appl. Phys., A62 (1996) 437.

[5] R. Lewis, (1997). Phys. Med. Biol. 42 (1997) 1213.

[6] T. Materna, J. Jolie, W. Mondelaers, B. Masschaele, V. Honkimaki, A. Koch, Th. Tschentscher, J. Synchrotron Rad., 6 (1999) 1059.

[7] T. Materna, TOUPI, A Reconstruction and Visualisation Package, Internal report IPF-PAN, University of Fribourg, Switzerland, 1999.

[8] Z.B. Alfassi, C. Chung (Eds), Prompt Gamma Neutron Activation Analysis, CRC Press, Boca Raton, 1995.

[9] G.L. Molnár, R.M. Lindstrom, Nuclear Reaction Prompt Gamma-Ray Analysis, in Nuclear Methods in Mineralogy and Geology: Techniques and Applications, A. Vértes et al. (Eds.), Plenum Press, 1998, p. 145.

[10] M. Crittin, J. Kern, J.-L. Schenker, Nucl. Instr. and Meth. A 449 (2000) 221.

[11] M. Crittin, J. Kern, J.-L. Schenker, J. Radioanal. Chem. 244 (2000) 399.

[12] G.S. Bauer, Nucl. Instr. and Meth. B 139 (1998) 65.

[13] M. A. Kumakhov, V. A. Sharov, Nature, 357 (june 1992) 390.

[14] H.H. Chen-Mayer et al., J. Radioanal. Chem. 215 (1997) 141.

[15] T. Materna, PICREAD, A fitting software, University of Fribourg, Switzerland, 1999.

[16] R.L. Paul, J. Radioanal. Chem. 191 (1995) 245.

PART II : COLD NEUTRON TOMOGRAPHY

II-1 Introduction

Basic concept

Radiography, using either X-rays or neutrons, provides pictures of the internal structure of objects by detecting the attenuation of the beam as it passes through different materials. While X-ray radiography is well known for its applications in diagnostic medicine, neutron radiography has emerged as a useful tool in industry and related research. Due to their fundamentally different interaction processes with matter, neutrons and x-rays are complementary in the nature of information supplied.

While the X-ray attenuation increases as the atomic number increases, no such rule exists for the attenuation of thermal neutrons (Fig.1). For example, some light elements (e.g. hydrogen and boron) have high thermal neutron attenuation coefficients, which gives high contrast in neutron imaging. On the other hand, some heavier materials (e.g. lead, bismuth and steel), which are essentially opaque to X-rays, are easily penetrated by neutrons. In addition, neutron attenuation characteristics in materials vary significantly with the neutron energy. For example, cold neutrons, compared to thermal neutrons, have lower attenuation coefficients for several metals (e.g. Al, Fe, Cu, Sn, Pb) due to the Laue-Bragg scattering. Otherwise, in most cases, the attenuation increases as the neutron energy decreases.

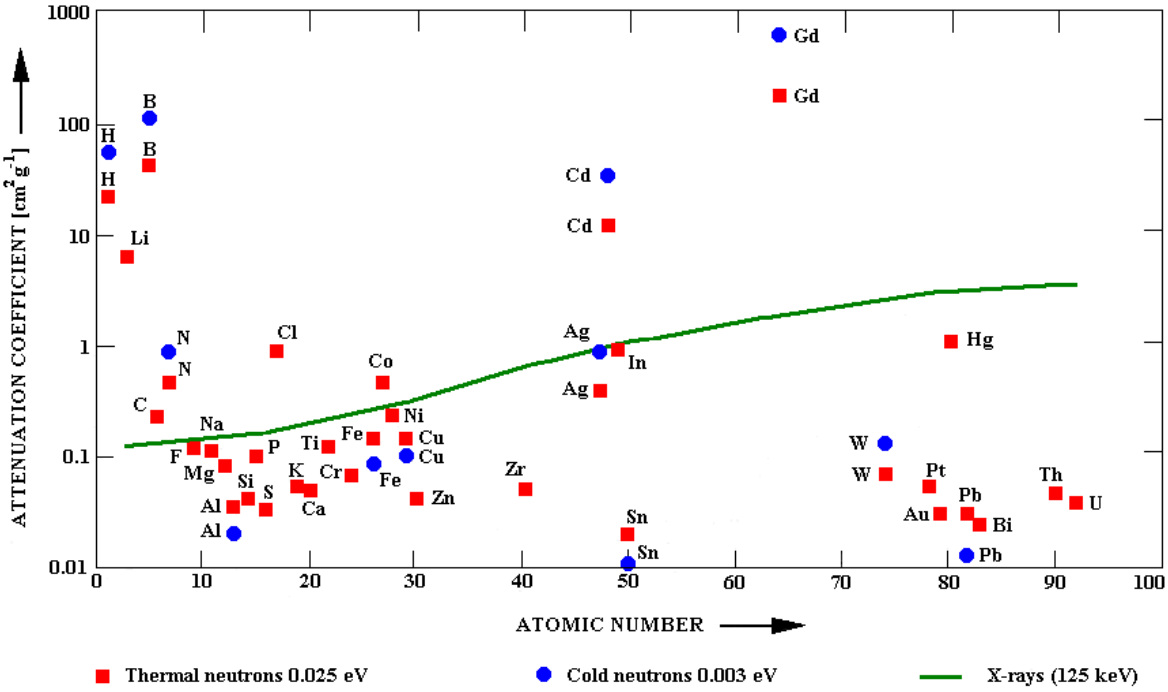

Fig. 1. X-ray and (thermal & cold) neutron attenuation coefficients for several elements.

A problem with radiography is the loss of depth information. Indeed, this technique is inadequate to resolve spatial structures along the direction of the beam. In contrast, computed tomography enables to look at cross-sectional images or "slices" of an object without physically cutting it. X-ray tomography has been revolutionary in diagnostic medicine, since it has enabled doctors to view internal organs with high precision. The principle of computed tomography is illustrated schematically in Fig. 2. By recording the transmission radiographs of an object from many different angles, it is possible to mathematically reconstruct the distribution of attenuation coefficient within an object. By assembling several slices, a 3-D volumetric image of the inner structure of the object can be built up. The reconstruction process is described briefly in what follows, and more details can be found in Ref. [1,2].

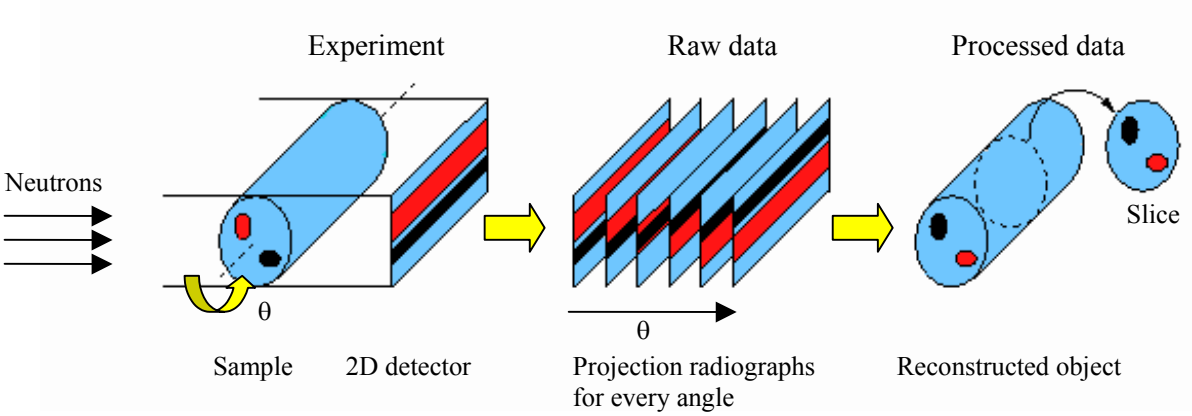

Fig, 2. Principle of computed tomography.

Tomographic reconstruction process

Assuming that the object is penetrated by a parallel beam, the procedure can be described in a (x,y) plane. The tomographic data acquisition is then modeled by the Radon transform:

$$p(t,\theta) = \Re\{\mu(x,y)\} = \int_{-\infty}^{\infty}\int_{-\infty}^{\infty} \mu(x,y)\delta(x\cos\theta + y\sin\theta - t)dxdy \qquad (1)$$

The measured projections $p(t,\theta)$ are considered as a set of line integrals passing through the 2D object $\mu(x,y)$ at angle θ ($0 \le \theta \le \pi$), see Fig. 3. Then the problem of reconstructing the image $\mu(x,y)$ from its projections is to compute the inverse Radon transform. This is based on the:

> **Fourier slice theorem**: The 1D Fourier transform of a projection taken at angle θ equals the central radial slice at angle θ of the 2D Fourier transform of the original object.

$$\Rightarrow F_1\{p(t,\theta)\} = P(\omega,\theta) = F_2\{\mu(x,y)\} = S(u,v) = S(\omega\cos\theta, \omega\sin\theta) \qquad (2)$$

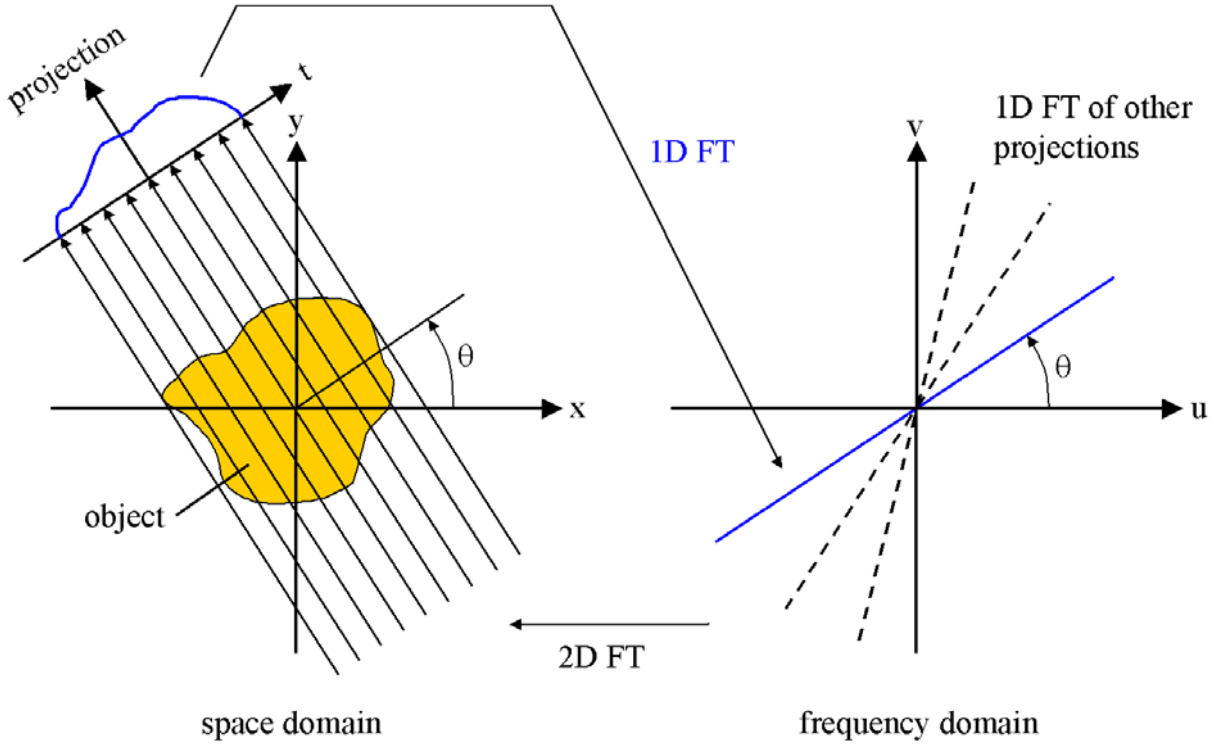

Fig. 3. The relation of the image space, the Radon space, and the Fourier space according to the Fourier slice theorem.

The Fourier slice theorem states that if the 2D Fourier space could be filled, the inverse 2D Fourier transform would give the original object (Fig. 2). In reality, as the number of rays and the number of projections are limited, the function S(u,v) is known only at a few points on radial lines (Fig. 3).

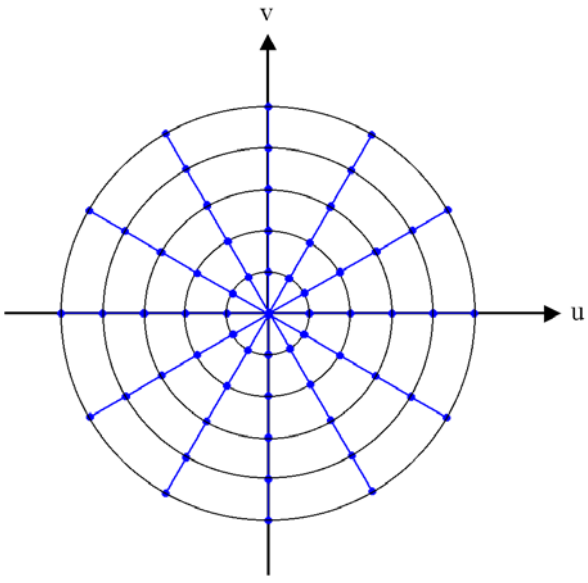

Fig. 4. Measured values in frequency domain.

Unfortunately, a discrete implementation of (2) using fast Fourier transforms (FFT) requires interpolations especially at the high frequencies, where the density of the resulting 2D Fourier space is low (see Fig. 4). This is why direct Fourier methods are not employed as inverse Radon transform algorithms. The most common algorithm is the filtered back projection (FBP), which is described next.

The inverse 2D FT expressed using the polar coordinates ω and θ in the frequency space is:

$$\begin{aligned}
\mu(x,y) = F_2^{-1}\{S(u,v)\} &= \int_{-\infty}^{\infty}\int_{-\infty}^{\infty} S(u,v)e^{i2\pi(xu+yv)}dudv \\
&= \int_{0}^{2\pi}\int_{0}^{\infty} S(\omega\cos\theta,\omega\sin\theta)e^{i2\pi\omega(x\cos\theta+y\sin\theta)}\omega d\omega d\theta \\
&= \int_{0}^{\pi}\left[\int_{-\infty}^{\infty} P(\omega,\theta)|\omega|e^{i2\pi\omega(x\cos\theta+y\sin\theta)}d\omega\right]d\theta \\
&= \int_{0}^{\pi} \hat{p}(x\cos\theta+y\sin\theta,\theta)d\theta := B\{\hat{p}(t,\theta)\} \qquad (3)
\end{aligned}$$

where the Fourier slice theorem (2) and the definition $\hat{p} := \int_{-\infty}^{\infty} P(\omega,\theta)|\omega|e^{i2\pi\omega t}d\omega$ were used. The notation $B\{\hat{p}(t,\theta)\}$ is the back projection of the filtered projections $\hat{p}(t,\theta)$ onto the reconstruction field.

The multiplication by $|\omega|$ serves as a filter applied to each projection profile in the frequency domain. This operation can be replaced by a convolution of $p(t,\theta)$ with the Fourier transform of $|\omega|$ in the spatial domain. Difficulties with the ideal filter $|\omega|$ occur with noisy data, as noise consists mainly of high frequencies, which are much enhanced by this filter. Therefore the ideal filter is often replaced by special filter functions that decrease towards high frequencies (like Shepp-Logan or Low Pass Cosine filter). Finally, the back-projection smears additively each filtered projection along the original ray path across the reconstruction field. Note that the filtered projection at the angle θ will make the same contribution to reconstruction at all those points in the image that correspond to the same t.

Reconstruction software used for neutron tomography was based on the filtered back-projection algorithm implemented under the C environment by Dr. T. Materna during his Ph.D. work at the University of Fribourg [3].

The new cold neutron tomography set-up at SINQ

The cold neutron tomography set-up, consisting of CCD camera, mirror, neutron screen, rotation and translation stage, was developed at the end of the PGA neutron guide 1RNR12. A detailed description of the set-up has been published in Nuclear Instruments and Methods in Physics Research A [Nucl. Instr. and Meth. A 481 (2002) 38]. Since its construction in 2000, the tomography system has been slightly modified to obtain higher performances. Special emphasis was placed on the improvement of the spatial resolution using thinner scintillators. Recently, in collaboration with N. Kardjilov (TU Munich), a neutron velocity selector was installed to perform radiography and tomography with monochromatic neutron beams. The paper related to this study, namely "*New features in cold neutron radiography and tomography, Part I: Thinner scintillators and a neutron velocity selector to improve the spatial resolution*", was submitted for publication in Nuclear Instruments and Methods in Physics Research A.

In addition, the use of the velocity selector in neutron imaging give the opportunity to achieve material discrimination. Indeed, the attenuation coefficient for monoenergetic cold neutrons changes quite drastically at the Bragg cut-offs for many solid materials due to the coherent scattering by the crystal lattice. In many cases, the variation in the total cross section for the corresponding elements is significant and this behavior can be exploited to differentiate among these materials. First results of these investigations were discussed by N. Kardjilov in the second part of the paper, *"New features in cold neutron radiography and tomography, Part II: Applied Energy-selective neutron radiography and tomography"*.

Applications

Various samples coming from different areas of activity, such as industry, geology, dentistry and more recently archeology, were studied by cold neutron tomography at SINQ. A new application has been initiated in nuclear industry with respect to final storage of radioactive waste. The aim of this study, realized in collaboration with P. Zimmermann (PSI), was to measure accurately the surface area of activated slag samples encapsulated in a lead container. Furthermore, the technique yielded promising results for the quality-control of pyrotechnic devices used in space programs, such as Ariane launchers programs. Investigations connected to aerospatial industry result from a cooperation with Dr. G. Bayon (CEA, France) through the COST action 524. Only a few of possible applications for neutron tomography are mentioned here, and more details can be found in chapter II.2 Publication.

Outlook

As a consequence of encouraging results provided by cold neutron imaging at the PGA beam line, a permanent tomography set-up supplied by a neutron velocity selector will be installed at the end of the NCR 1RNR13 neutron guide (SINQ).

References

[1] A.C. Kak, M. Slaney, Principles of computerized tomographic imaging, IEE Press, New York, 1998.

[2] J.A. Parker, Image Reconstruction in Radiology, CRC Press, Boston 1990.

[3] T. Materna, TOUPI, a reconstruction visualisation package, internal report IPF-PAN, University of Fribourg, Switzerland, 1999.

The new cold neutron tomography set-up at SINQ

S. Baechler[a,b], B. Masschaele[c], P. Cauwels[c], M. Dierick[c], J. Jolie[d], T. Materna[d], W. Mondelaers[c]

[a] *Physics Department, University of Fribourg, Ch. du Musée 3, Ch-1700 Fribourg, Switzerland*
[b] *Paul Scherrer Institute, CH-5232 Villigen, Switzerland*
[c] *Vakgroep Subatomaire en Stralingsfysica, University of Gent, B-9000 Gent, Belgium*
[d] *Institut für Kernphysik, Universität zu Köln, D-50937 Köln, Germany*

A new cold neutron tomography set-up is operational at the neutron spallation source SINQ of the Paul Scherrer Institute (PSI) in Villigen, Switzerland. The detection system is based on a ^{6}LiF/ZnS:Ag conversion screen and a CCD camera. Several tests have been carried out to characterize the quality of the tomography system, such as homogeneity, reproducibility, L/D-ratio and spatial resolution. The high flux and the good efficiency of the detector lead to very short exposure times. Thus, a typical set of tomography scans can be performed in only 20 min. Then, 3D computed tomography objects were calculated using the filtered back-projection reconstruction method. Initial results of various samples show that cold neutron tomography can be a useful tool for industry, geology and dentistry. Furthermore, suitable applications can be found in the field of archeology.

Keywords: Cold neutron computed tomography; Neutron detector; CCD camera.

1. Introduction

X-ray tomography is a non-destructive method of analysis widely used in medical imaging. The goal is to look at slices of objects without physically cutting it. For this purpose, a series of X-ray radiographs taken at different angles are computed to create cross-sectional images. This technique provides information about the inner structures of a subject. The same method can be applied using neutrons instead of X-rays. Thermal neutrons and X-rays share the common properties that neither is charged and both have wavelengths comparable with the mean separations of atoms in solids. However, their properties contrast rather than compare in other important aspects. Most of the radiographic inspection techniques are based on the attenuation of an incident beam through an object. X-rays, passing through an object, interact predominantly with the outer shell electrons of the atom. This results in the absorption of X-rays increasing monotonically as a function of

the number of electrons of the atom. Unlike X-rays, neutrons are attenuated by matter, either by scattering from the nucleus of the target or through absorption by that nucleus. Since neutrons interact with the nucleus of the atom, the interaction is a more random function when plotted vs. Z. Thus, photons are almost unable to discriminate between materials of similar atomic number Z, but neutrons can interact differently and show significant differences between these materials. For instance, boron and carbon, or cadmium and tin, both neighbouring elements in the periodic table, are easily distinguishable by neutron radiography. Another difference is that several light elements such as hydrogen and boron, being transparent to X-rays, are highly neutron absorbent and their trace in samples can be detected without difficulty. In contrast, heavy materials, e.g. lead, bismuth and steel, are relatively opaque to X-rays but easily penetrated by neutrons [1]. Thus, neutron tomography is a complementary technique to X-ray tomography, allowing investigation of different types of samples.

If cold neutrons are used, a stronger contrast can be achieved, because in most of the cases the total cross-section increases as the neutron wavelength increases. For elements which are predominantly absorbers, e.g. B, Li, Cl, Cd and Hg, the neutron absorption cross-section follows the 1/v dependence below the resonance region, where v is the neutron velocity. The attenuation coefficient of hydrogen, a predominantly scatter nucleus, increases significantly for low energy neutrons. An important behaviour of cold neutrons occurs in crystalline materials. If the wavelength of neutrons is greater than the Bragg cut-off, i.e. twice the largest lattice spacing of the material, the coherent neutron scattering cross section decreases abruptly. The Bragg cut-off depends on the material and is around 4 Å for many metals. Thus, cold neutrons penetrate thicker metallic materials such as Al, Fe, Ni, Cu and Pb.

The standard procedure for tomography consists in measuring the beam attenuation at several orientations of a sample [2, 3]. The recorded patterns are then used to reconstruct tomograms that are cross-sectional images yielding the attenuation coefficient distribution. These images are then assembled into a three-dimensional picture that can display the whole object under study in great detail.

In addition to the thermal neutron radiography station [4, 5], a new cold neutron tomography set-up was developed at the Swiss spallation source SINQ of the Paul Scherrer Institute (Villigen, Switzerland). Among the European facilities connected to the COST action 524 “Neutron Tomography and Computation Analysis” [6], this installation presently provides the unique possibility to perform neutron tomography at a cold beam line.

2. Experimental apparatus

The new cold neutron tomography set-up is located at the end of the 64 m long PGAA neutron guide 1RNR12 [7], exploiting the high cold neutron flux of the spallation source SINQ. A super-mirror coating was chosen for the neutron guide, except the last 10 m coated with natural Ni. The first 23-m of the neutron guide is curved and the radius of curvature is 3612 m giving a characteristic cut-off wavelength λ^* of approximately 1.0 Å. The neutron wavelength spectrum was determined by neutron time of flight [8,9]. The "effective" wavelength, corresponding to the arithmetic mean value of this nearly Maxwellian distribution, is about 5.5 Å. The beam size at the exit of the guide is 20 mm wide and 50 mm high and the neutron flux at the sample position is about $1.2 \cdot 10^8$ n/cm^{2}s for the present 1.2 mA proton current impinging the spallation source target. A continuous measurement of this current gives a monitoring of the neutron flux. The spallation neutron source SINQ has been described in more detail elsewhere [8].

The incident beam interacts with a sample placed on a rotation table. Finally, the detection system records the distribution of the transmitted beam. Additional step motors permit the specimen to be translated into the two transverse directions. The rotation table and the detection system are placed on rails and can be moved along the beam axis independently. The neutron tomography set-up is shown in Fig. 1. The detector is composed of a conversion screen and a CCD camera [10]. The whole installation is very compact and can be easily dismounted or transferred to another facility.

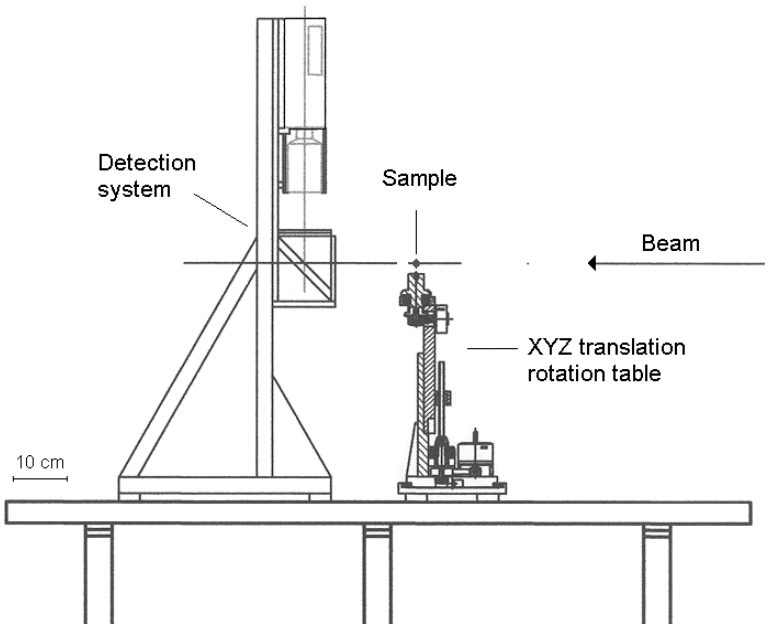

Fig. 1. Cold neutron tomography set-up at the Swiss spallation neutron source SINQ.

The neutron to visible light converter consists of a dispersion of ZnS(Ag) and ^{6}LiF in an acrylic binder [11]. The detection mechanism is based on the ^{6}Li(n,α)^{3}H nuclear interaction. Then, ejected alphas and tritons interact with phosphor to create scintillation events that can be detected by a CCD imaging system. The conversion screen emits a spectrum in the blue region with a wavelength peak at 460 nm An advantage of this converter is the relatively low gamma sensitivity. Since neutron capture cross-section of ^{6}Li, as well as most of the nuclei, is inversely proportional to the neutron velocity, the conversion efficiency is higher using cold neutrons than thermal neutrons. Furthermore, the scintillator is aluminized to enhance the intrinsic efficiency; indeed, an aluminium layer acts as a reflector for back scattered light [11]. The 10-cm SQ by 420-µm thick converter is imaged using an optical lens, a 45°-mirror and a CCD camera. The silver-free mirror, made of aluminium and titanium to avoid lasting activation, keeps the camera out of the direct beam. In addition, a lead glass is placed between the mirror and the camera to protect the chip from emitted photons.

The front side illuminated CCD camera has a scan area of 8.6×6.9 mm^2 covered by 1280×1024 pixels, a dynamic range of 12 bits (4096 gray-levels per pixel) and a fast read-out time of 8 full frames per second. An active area of (2.8×2.2) cm^2 is projected on the CCD detector, corresponding to 22 µm pixels on the scintillator and sample. For the scanning of the projections, the CCD is binned by a factor 4 in each direction to minimize the size of the images. Thus, the 320×256 matrix, resulting in a pixel size of 88 µm, needs 160 KB of disk space. The camera is Peltier cooled to –12°C in order to reduce electronic background. Furthermore, the spectral sensitivity matches with the blue emission spectrum of the scintillator. The data stream is transferred via a fibre optic cable connecting camera and PCI-Interface-Board. A schematic map of the detector is illustrated in Fig 2.

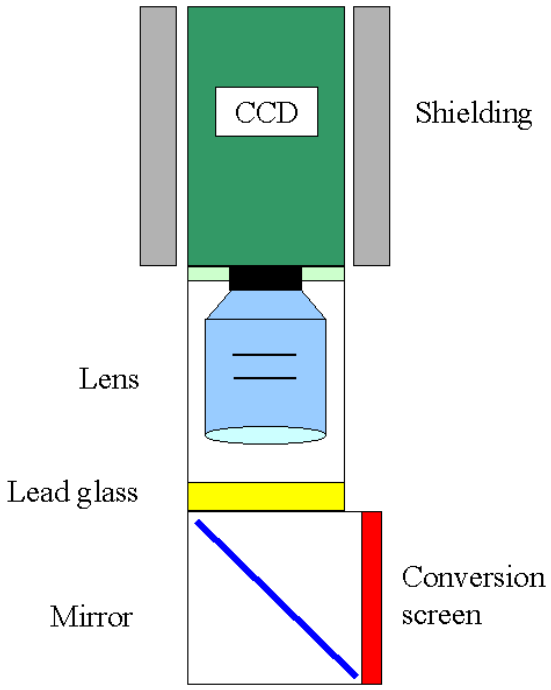

Fig. 2. The detection system based on a CCD camera and a ^{6}LiF/ZnS:Ag conversion screen.

The detection system is protected by neutron/gamma-shields to avoid neutron damage and to suppress the interference with scattered gamma rays from the environment.

Materials used for this purpose are ^{6}LiF polymer (3 mm) and B_4C plates for neutrons and lead bricks (2.5 cm) for gamma rays. In addition, the very low gamma background present in the PGAA bunker is an asset for a tomography location. Software for controlling the camera settings, displaying and storing the images and positioning the motors was developed on Labview©. Thus, the whole experimental procedure can be performed automatically on a standard PC.

3. Characterization of the set-up

Some characteristics of the new cold neutron tomography set-up have been determined to test its performance. The line profile across the neutron beam distribution is essentially flat, with a small breakdown on the right side (Fig. 3). Indeed the distribution over the width is inhomogeneous due to the curvature of the guide [9]. To assess the reproducibility of these inhomogeneities, two images of the white beam were recorded under the same conditions. By dividing both images, the arithmetic mean μ and the standard deviation σ were calculated over the pixel array. The results ($\mu = 1.00$ and $\sigma = 0.01$) show a good reproducibility of the set-up.

The converter and the divergence of the beam essentially influence the lack of image sharpness (or spatial resolution). The neutron guide acts as a divergent source and the divergence angle θ is given by twice the critical angle of reflection γ_c. The latter depends on the neutron wavelength and for a guide coated with natural nickel, $\gamma_c = 0.1°/Å$. Using $\lambda_{eff} = 5.5$ Å, an "effective" divergence angle can be calculated, $\theta_{eff} = 1.1°$. The divergence angle determines the quality of the projection and thus an effective $L/D = 1/\tan(\theta_{eff}) = 52$ is calculated. This estimation is available for a constant angular distribution of the neutrons. In reality, imperfections of the neutron guide decrease the reflectivity essentially at big angles, leading to a smaller effective divergence and thus a greater L/D [12].

The spatial resolution was studied experimentally by measuring a sharp knife-edge of a 25-μm thick Gadolinium foil. From a line profile perpendicular across the edge, the Line Spread Function (LSF) can be calculated [13,14]. Then, the resolution is given by the full width at half maximum (FWHM) of the LSF. The Modulation Transfer Function (MTF) for spatial frequencies in the range of 0-1.5 lp/mm was calculated from the Fourier transform of the LSF. For instance, the LSF and MTF are shown in Fig. 4, where the distance between the foil and the converter is 2.5 cm. This configuration with a distance sample-converter of 2.5 cm is typical for tomography, allowing the sample to be rotated in front of the detector. To study the impact of the beam divergence on the spatial resolution, an edge is measured at different distances between the foil and the converter. Then, the corresponding resolution was extracted.

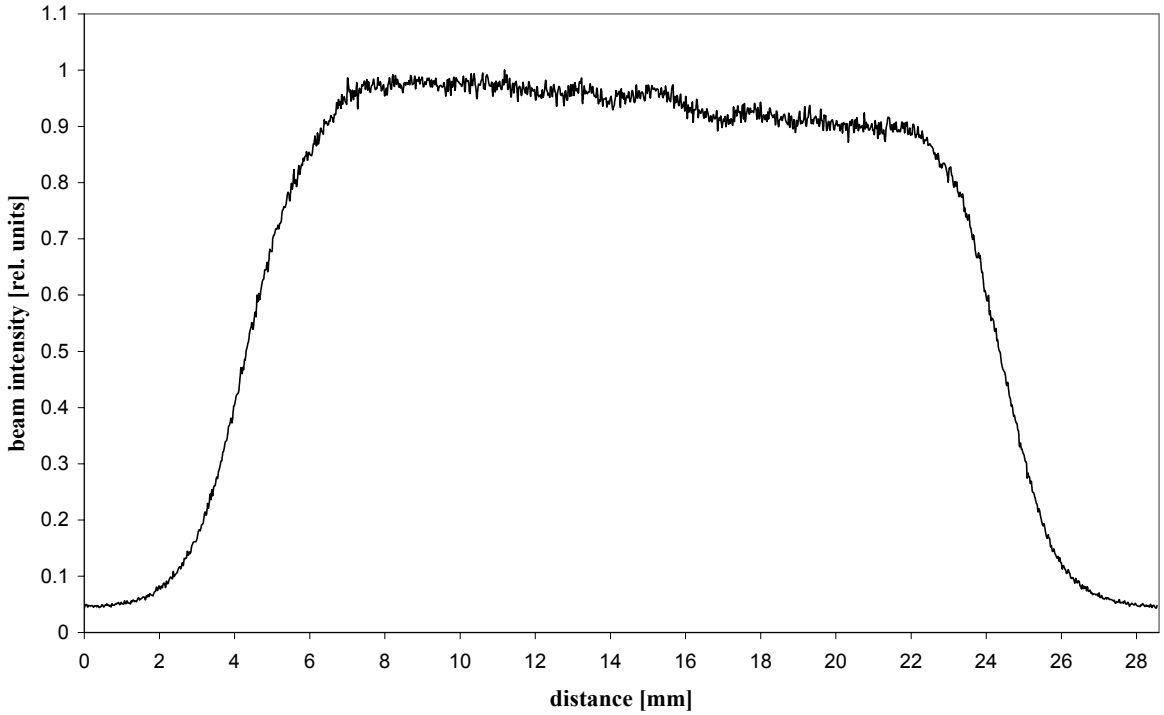

Fig. 3. Horizontal line profile across the neutron beam measured with the new tomography set-up.

Except for the value obtained when the foil and converter are in close contact, the relation between the distance and the resolution is clearly linear (Fig. 5). The detection of radiation emitted from the gadolinium foil by the converter could explain the non-linear behavior of the offset. Thus, the inherent resolution of the detection system, including the effects of the neutron converter, the lens and the CCD corresponds to the intercept of the straight line and is about 0.33 mm. The lack of geometric sharpness relative to the distance foil-converter is given by 1/(L/D) [15], but also by the slope of this straight line. This yields a value of L/D = 1/0.0137 = 73 which is slightly greater than the theoretical value, as expected. In the future, a more accurate L/D measurement will be performed with the standard method described by Kobayashi and Wakao [16].

The high neutron flux and also the good sensitivity of the CCD based detection system lead to a typical exposure time of only 750 μs. Including the time to rotate the sample and the time to read-out and save images, the system acquires 400 projections in about 20 min. Thus, the new set-up at SINQ eliminates most of temporal limitations in the field of neutron tomography. Furthermore, half the time can be saved by performing only 200 rotations. Indeed, the reconstruction with 200 and 400 projections seem to be both equally good.

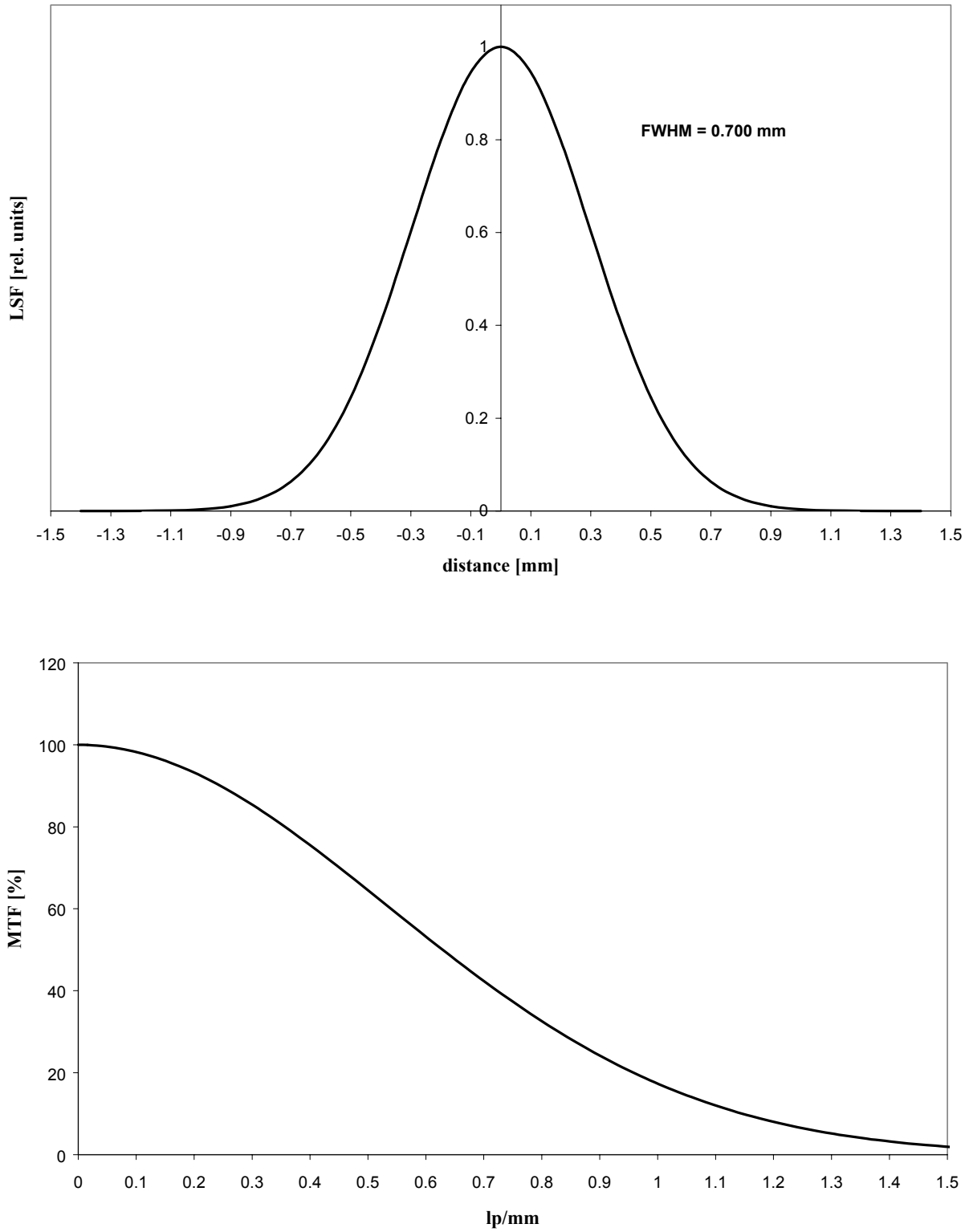

Fig. 4. (a) LSF and (b) MTF determined with the detection system when the distance between the gadolinium foil and the converter is 2.5 cm.

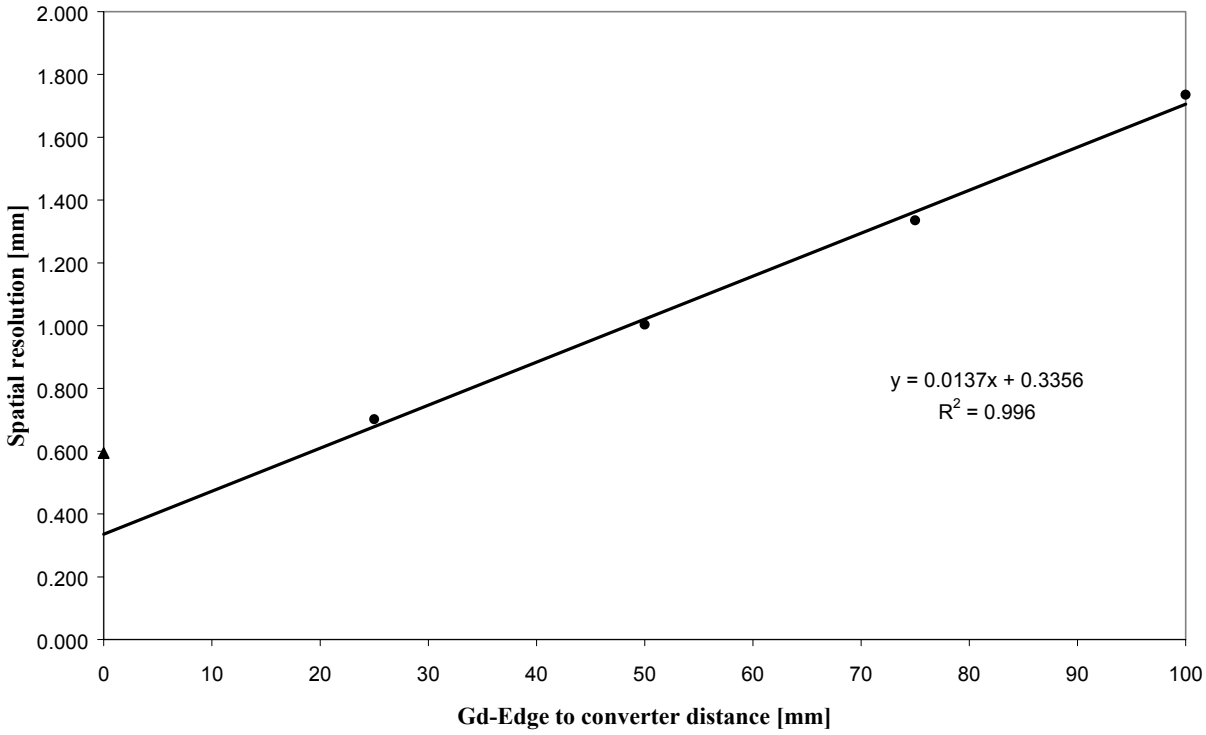

Fig. 5. Resolution determined by the FWHM of the LSF vs. gadolinium foil to converter distance.

4. Data Reconstruction

The raw data files are saved as they are collected to the local drive for subsequent processing. The first correction that must be considered is for white spots; they are caused by gamma radiation hitting the CCD chip [17]. For that purpose, a 3×3 median filter is applied to the whole data set. The technique consists in replacing the pixel value with the median of neighbouring pixel values. To take the varying neutron exposure into account, projections are normalized by the proton current impinging the target during the image acquisition. The dark current, the signal measured in the absence of any neutrons, is very uniform. Thus, an average background is subtracted from the flat field and the projections. The flat field is the image measured with neutrons, but without a sample in the beam, including effects of non-uniformity in the incident neutron beam and a non-uniform response of the detection system. A mean flat field is calculated for the normalization of the projections. Then, the sinograms are created and computed by taking the negative logarithm.

Finally, each slice is reconstructed independently by back-projecting the sinograms. Assuming parallel beam geometry, a filtered back-projection algorithm with a Shepp-Logan filter is used for the reconstruction [18]. Both reconstruction method and image processing have been implemented in C language [19].

Using VGStudio MAX 1.0©, 3D images of the sample under investigation are generated immediately by assembling the reconstructed slices into a 3D-array [20]. The computational time is completely dominated by the time to back-project. The typical CPU time on a PII-300 MHz PC is about 30 s to reconstruct a 320×320 pixels tomogram. Thus, the total amount of time required for the whole procedure, including the scanning of the 400 projections, is about 3 h for a $320 \times 320 \times 256$ data volume (50 MB).

5. Results and discussions

A variety of few-centimeters size samples coming from different fields were studied to illustrate suitable applications of cold neutron tomography. The first investigation was the study of mercury leaking from silver/amalgam fillings in teeth. Mercury is a predominantly absorber and then the sensitivity can be enhanced using cold neutrons. The vertical cut of the three-dimensional reconstruction, in Fig. 6, shows the core composed of soft pulp, surrounded by a layer of dentine that is coated with enamel. The filling is the strongest neutron absorber and can be clearly distinguished. Indeed, amalgam/silver dental fillings contain about 50% metallic mercury. No evident trace of mercury has been found in the inspected teeth, but further analyses have to be done to determine the limits of the method.

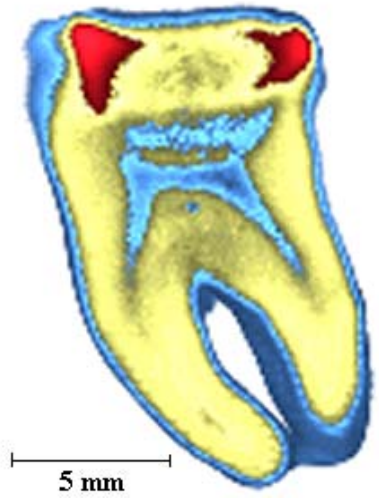

Fig. 6. Vertical cut in a 3D reconstructed tooth showing filling, enamel, dentine and dental pulp.

Next, the technique was applied to produce quality information in geology. An ore of cinnabar from Tuscany (Italy), made up of mercury sulfide, has been studied. As illustrated in Fig. 7, a high contrast was achieved between mercury and limestone; the layered deposit of mercury can be located on the outside of the sample.

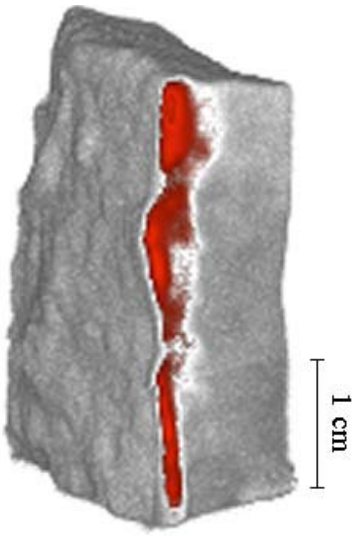

Fig. 7. Reconstructed image of a cinnabar ore with a thin layer of mercury on the outside.

Since neutrons penetrate metals easily, electronic devices are favorable samples to be inspected by neutrons. Another illustration of the technique was a tomography of an Erasable Programmable Read Only Memory (EPROM). In Fig 8, the circular quartz window covering the chip is transparent to the naked eye but relatively opaque to neutrons. On the reconstructed three-dimensional picture, pins and connectors can also be clearly made out. Finally, a small electric motor was investigated. Fig. 9 shows a part of this device with rolling bearings in the central cavity.

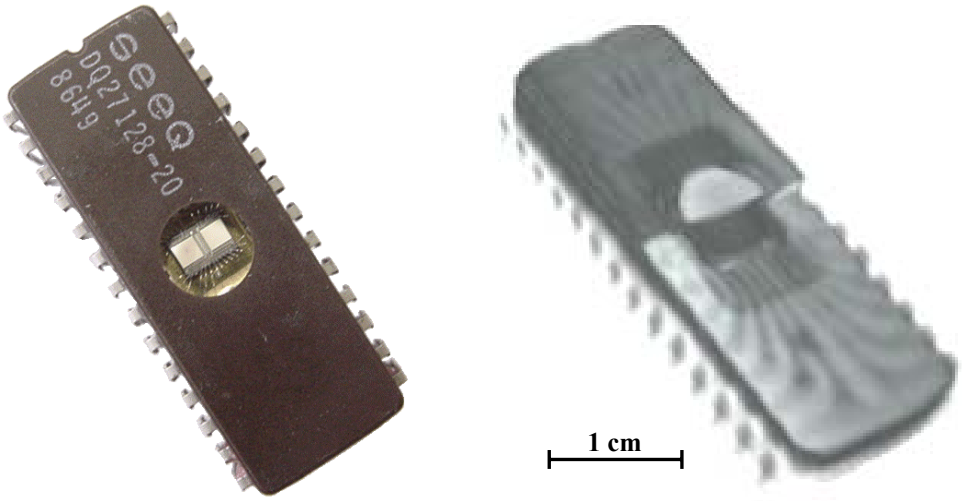

Fig. 8. Partial vertical cut in a 3D image of an EPROM revealing the structure in detail.

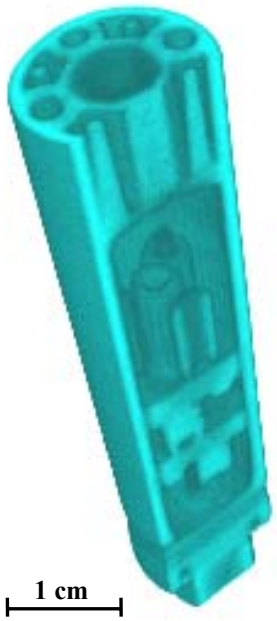

Fig. 9. Inner part of a 3D reconstructed electric motor.

6. Conclusions and outlook

Tomography using a cold neutron beam has been shown to be an interesting approach in obtaining strong contrast imaging. Due the high flux available at SINQ, a low exposure time per image is necessary and thus most of the limitations in time resolution are eliminated. The choice of a CCD camera and a ^{6}LiF/ZnS:Ag converter as the detection system allows fast scans with a high sensitivity. However, the 12 bits dynamic range of the CCD is not sufficient for high quality tomography, particularly with such small

samples. In the future, the dynamic in the images will be improved by using a 16 bits CCD.

The spatial resolution is limited by the divergence of the beam and the conversion screen. At the end of the neutron guide, the critical angle of reflection and the wavelength spectrum determines a relatively low "effective" L/D. Further improvements on the L/D could be certainly achieved by using Soller collimators at the exit of the guide. Different scintillators will be tested also in order to increase the spatial resolution. Particularly, a reduction in the thickness of the ^{6}LiF/ZnS:Ag converter could carry out big improvements while maintaining a reasonable efficiency.

Interesting applications for neutron tomography can be found in industry, geology, archeology and dentistry. Tomography using neutrons is a complementary technique to classical X-ray tomography. The spatial resolution is not as good as the resolution available with synchrotron light [21], nevertheless neutron tomography can produce information where X-rays must fail. For instance, this technique provides a good opportunity to safely investigate nuclear waste encapsulated in a lead container. It will also be possible to look inside pyrotechnical devices even though they are covered by lead or steel cladding. Since cold neutrons are strongly attenuated by hydrogen, traces of hydrogen in inorganic materials can be easily detected.

Finally, the temporary transfer of a velocity selector will enable to perform energy-selective neutron radiography and tomography. By selecting neutrons with energies just above and just below the Bragg cut-off of some materials, it is possible to discriminate between components of a sample [22]. Indeed, the Bragg cut-off is related to an abrupt drop in the attenuation coefficient below an energy given by the material. Thus, the radiographs show a different contrast depending on the energy of the neutrons and the components are easily separated by image processing. All of these investigations will be undertaken in the near future.

Acknowledgements

The present study is supported by the Swiss National Science Foundation, the Paul Scherrer Institute and by the Research Board of the Rijksuniversiteit Gent. The authors wish to express their gratitude to Dr. E. Lehman and P. Vontobel for their help and also Prof. M. Maggetti and Dr. H. Surbeck for providing some of the samples.

[1] J. Byrne, Neutrons, Nuclei and Matter, An exploration of the Physics of Slow Neutrons, Institute of Physics Publishing, 1994.

[2] A.C. Kak, M. Slaney, Principles of Computerized Tomographic Imaging, IEEE Press, New York, 1988.

[3] J.A. Parker, Image Reconstruction in Radiology, CRC press, Boston, 1990.

[4] E. Lehmann, P. Vontobel, L. Wienzel, Properties of the Radiography Facility NEUTRA at SINQ and its potential use as European reference facility, Sixth World Conference on Neutron Radiography, Osaka, 1999.

[5] P. Vontobel et al., Neutron tomography setup at SINQ: Status and first results, PSI-Annual Report, Volume VI: Large Research Facilities.

[6] For further information, see http://www.cost524.com.

[7] M. Crittin, J. Kern, J.-L. Schenker, Nucl. Instr. and Meth. A 449 (2000) 221.

[8] G.S. Bauer, Nucl. Instr. and Meth. B 139 (1998) 65.

[9] W. Wagner et al., J. Neutron Res. 6 (1998) 249.

[10] H. Pleinert, E. Lehmann, S. Körner, Nucl. Instr. and Meth. A 399 (1997) 382

[11] For further information, see http://www.appscintech.com.

[12] B. Schillinger, Estimation and measurement of L/D on a cold and thermal neutron guide, Sixth World Conference on Neutron Radiography, Osaka, 1999.

[13] H. Kolbe, E. Lehmann, W. Gunia, S. Körner, Nucl. Instr. and Meth. A 424 (1999) 40.

[14] A.L. Weickenmeier, W. Nüchter, J. Mayer, Optik 4 (1995) 147.

[15] H. Kobayashi, Beam Formation and Characterization for Neutron Radiography, Neutron Radiography, Vol. 6, Gordon and Breach Science Publishers, London, New York, 2000, pp. 167-176.

[16] H. Kobayashi, H. Wakao, Accurate measurement of L, D and L/D for divergent collimators, Neutron Radiography, Vol. 3, Kluwer Academic Publishers, Dordrecht, MA, 1990, pp. 889-892.

[17] B. Schillinger, Neue Entwicklungen zu Radiographie und Tomographie mit thermischen Neutronen und zu deren routinemässigem Einsatz, Dissertation TU München, Mensch & Buch Verlag Berlin, 1999.

[18] G.T. Herman, Image Reconstruction from Projections, Academic press, New York 1980.

[19] T. Materna, TOUPI A reconstruction and visualisation package, Internal report IPF-PAN, University of Fribourg, Switzerland.

[20] For further information, see http://www.volumegraphics.com.

[21] Th. Materna, J. Jolie, W. Mondelaers, B. Masschaele, V. Honkimaki, A. Koch, Th. Tschentscher, J. Synchrotron Rad. **6** (1999) 1059.

[22] T.E. McDonald Jr. et al., Time-gated energy-selected cold neutron radiography, Nucl. Instr. and Meth. A 424 (1999) 235.

New features in cold neutron radiography and tomography Part I: Thinner scintillators and a neutron velocity selector to improve the spatial resolution

S. Baechler[a,b*], N. Kardjilov[c], M. Dierick[d], J. Jolie[e], G. Kühne[b],
E. Lehmann[b], T. Materna[e],

[a] *Physics Department, University of Fribourg, Ch-1700 Fribourg, Switzerland*
[b] *Paul Scherrer Institute, CH-5232 Villigen, Switzerland*
[c] *Fakultät für Physik E21, Technische Universität München, D-85747 Garching, Germany*
[d] *Vakgroep Subatomaire en Stralingsfysica, University of Gent, B-9000 Gent, Belgium*
[e] *Institut für Kernphysik, Universität zu Köln, D-50937 Köln, Germany*

The tomography set-up developed at the PGA facility of the Swiss spallation source SINQ has provided encouraging results in the field of cold neutron imaging. Performances of the detection system based on a CCD camera and a converter screen have been recently improved using ^{6}LiF/ZnS:Ag scintillators with different thickness. Indeed, reducing the layer of the scintillator improved considerably the spatial resolution while keeping a reasonable efficiency. Furthermore, a neutron velocity selector was temporarily added to the set-up to perform radiography and tomography experiments with monochromatic neutron beams. Basic properties of transmitted beams were studied to assess the applicability of this device in neutron imaging. Of interest was the enhancement of the L/D-ratio by selecting neutron beams of short wavelengths. Cold neutron tomography demonstrated to be a useful technique in various spheres of activity, such as aerospatial industry or radioactive waste storage. Various applications of the neutron velocity selector are described in the second part, namely, New features in cold neutron radiography and tomography – part II: Applied energy-selective neutron radiography and tomography.

1. Introduction

The cold neutron tomography setup at the Swiss spallation source SINQ of the Paul Scherrer Institute has been successfully operated at the end of the 1RNR12 PGA neutron guide since March 2000 [1]. Interesting applications were performed with this set-up on samples coming from different fields: industry, geology and dentistry. However, a higher spatial resolution is required for several technical applications,

such as the control of pyrotechnic material for the aerospatial industry or generally for the study of fine details in biological, geological and archeological objects. Neutron tomography limitations in image sharpness are predominantly given by the converter and the beam divergence. Here we study possible ways to improve the quality of the installation, focusing on beam divergence, detector resolution and the wavelength of the neutrons. The latter is of importance because cold neutrons, in comparison with thermal neutrons at the NEUTRA facility [2], produce images with higher contrast due to the 1/v behavior of the neutron capture cross section. Moreover for those elements, like metallic components, which show deviations from the 1/v behavior, the different transparency depending on the neutron wavelength can be used.

In a neutron guide, the divergence of the beam is determined by the critical angle of reflection, which depends on the neutron wavelength [3]. An effective divergence angle of 0.8°, corresponding to a L/D-ratio of 70, was experimentally determined at the end of the guide. Such a low L/D-ratio limits considerably the achievable spatial resolution independently from the detector properties. Indeed, the unsharpness U is related to the distance between the object and the detector plane d and the L/D: U = d/(L/D) [4].

The quality of images is also affected by the characteristics of the detection system. The inherent resolution of the detector based on a CCD camera looking onto a standard ^{6}LiF/ZnS:Ag scintillator has been determined to be about 0.6 mm. To our knowledge, the standard 0.42-mm-thick ^{6}LiF/ZnS:Ag scintillator (ND type) yields the best performance for thermal neutrons. The absorption layer thickness was optimized to obtain a good compromise between self-shielding effects and interaction probabilities. The reduction in thickness of the converter is a common way to improve the spatial resolution. Indeed, a thinner layer limits the spread of light in the scintillator and thus reduces the detector blurring. On the other hand, the thinning down decreases the efficiency while a reasonably short duration of a single projection is required for tomography experiments. Imaging properties such as resolution, efficiency and linearity were determined for ^{6}LiF/ZnS:Ag screen with various thickness. A 0.10-mm and 0.20-mm-thick scintillator have been specially manufactured for this purpose [5].

A setup at the end of a neutron guide never competes with the classic flight tube setup concerning spatial resolution [6]. The effects of the beam divergence on the image quality were studied by measuring the spatial resolution at different distances between the object and the converter plane. These investigations were also performed at the end of the NCR 1RNR13 neutron guide, where the beam conditions were only slightly different [7].

Finally, a neutron velocity selector was installed at the end of the PGA neutron guide

to obtain radiography and tomography at specific neutron energies. The transmitted beam was characterized and studied in detail for different neutron wavelengths. In fact, the velocity selector acts as a collimator at short wavelength, because the divergence angle of the beam is proportional to the wavelength. Besides, the monochromator gives the possibility to modify the contrast of radiographs. Indeed, neutrons interact with matter in different ways which depend strongly on the energies of the incidents neutrons. For instance attenuation coefficients vary abruptly in crystalline materials at the so-called Bragg cut-off. This phenomenon can be exploited to achieve materials discrimination in radiography and tomography images by selecting appropriate neutron energy beams [8], [9].

2. Experimental apparatus

The tomography detector has been developed at the PGA station using cold neutrons provided by the spallation source SINQ [10]. Cold neutrons are transported to the experiments by means of super-mirror coated neutron guides. The coating allows an increase of the critical angle of reflection by a factor of two when compared with common Ni coated guides. Therefore, the flux at the end of the guides is considerably improved and the transmitted spectrum is enlarged into the thermal regime. However, a bigger critical angle of reflection implies a higher divergence of the beam. In other words, super-mirror guides have a lower L/D-ratio than Ni coated guides. The last 10 m of the PGA neutron guide are coated with pure Ni. The beam size at the exit of the guide is 20 mm wide and 50 mm high and the neutron flux at the sample position is about $1.8 \cdot 10^8$ n/cm^{2}s. On the other hand, the NCR station is located at the end of a completely super-mirror coated guide of 30x120 mm^2 cross section with a neutron flux of $4.9 \cdot 10^8$ n/cm^2.

The visible light emitted from the ^{6}LiF/ZnS(Ag) scintillator exposed to the neutron beam was imaged with an optical lens onto a Peltier-cooled CCD camera through a 45-degree mirror. The converter was fixed onto a 2-mm-thick aluminum plate to avoid penetration of surrounding light inside the detection box. The CCD-sensor had a scan area of 8.6x6.9 mm^2 covered by 1280x1024 pixels (6.7 μm square pixels), a dynamic range of 12 bits (4096 gray-levels per pixel) and a fast read-out time of 8 full frames per second. The optical configuration resulted in a field of view of (2.7x3.4) cm^2. Thus, the effective pixel size of 26 μm did not restrict the achievable resolution. The detection system was shielded against neutron and gamma radiation in order to avoid white spots on images. Finally, the data stream was transferred via a fiber optic cable connecting camera and PCI-Interface-Board. Software for controlling the camera settings, displaying and storing the images was developed on Labview©. A typical exposure time of 7 s was necessary to cover the full

dynamic range of the CCD using the 0.42-mm-thick scintillator under standard conditions at the PGA station. The detection system has been described in more details elsewhere [1].

3. Basic properties of the detection system

3.1 Spatial resolution

The spatial resolution of the detection system was measured by taking a radiograph of a sharp-edge made up of a 25-μm-thick Gadolinium foil placed directly on the aluminum plate of the scintillator. Then, the Edge Spread Function (ESF) was determined from a line profile perpendicular across the edge. The Line Spread Function (LSF) can be easily found by taking the derivative of the ESF and the Modulation Transfer Function (MTF) by calculating the one-dimensional Fast Fourier Transform (FFT) of the LSF. The distance required for the edge response to rise from 10% to 90% yielded the spatial resolution. The main advantage of using ESF for measuring resolution is that all edges responses have a similar shape [11]. On the other hand, the LSF depicts either a Lorentzian shape when the image blurring comes predominantly from the converter or a Gaussian shape when several degradation sources are combined, such as converter, scattering and geometric unsharpness [12]. Fig. 1 shows ESF obtained with ^{6}LiF/ZnS:Ag scintillators of various thickness: the standard

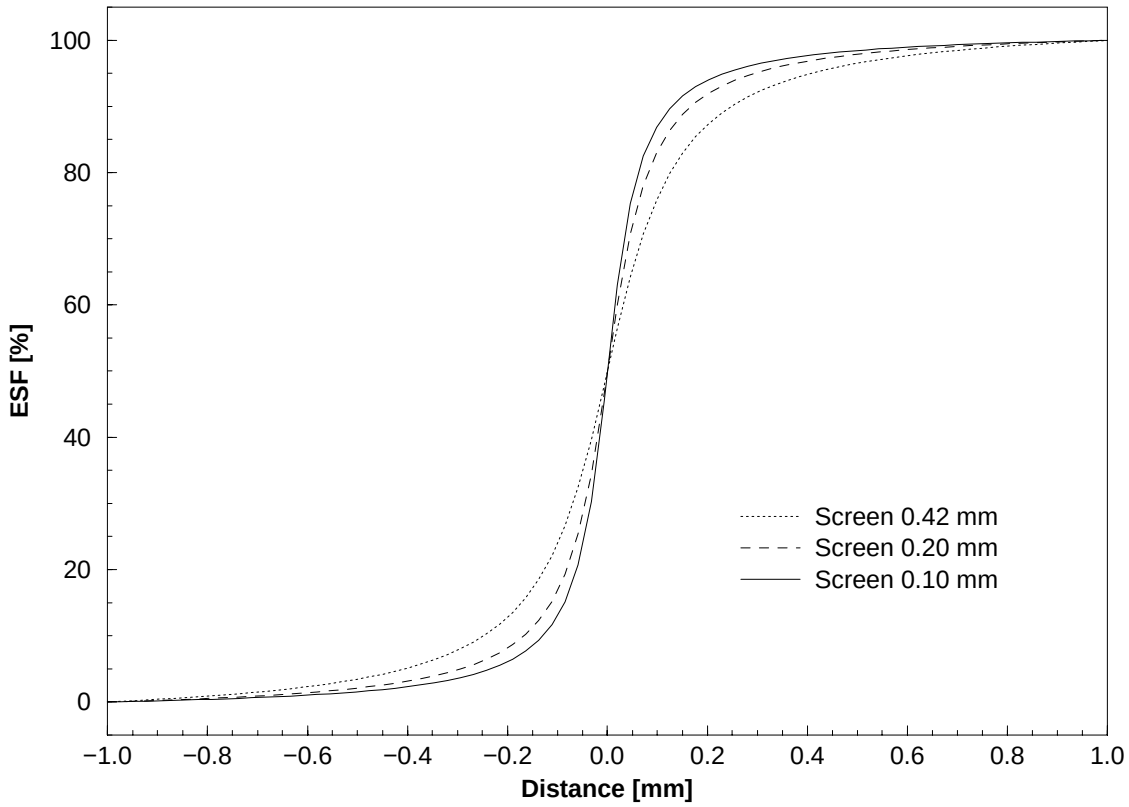

Fig. 1. Edge Spread Function of three converter screens with different thickness.

0.42-mm as well as the 0.20-mm and 0.10-mm-thick screens manufactured for this experiment. In Table 1, the spatial resolution was determined by calculating the mean value of the 10%-90% responses obtained at the PGA and NCR beam line. Small errors corresponding to the one standard deviation (1SD) confirm that when the object was directly on the screen, the geometric properties of the guide did not influence the resolution.

Table 1. Spatial resolution and relative efficiency of the detection system using ^{6}LiF/ZnS:Ag scintillators with various thickness

Thickness [mm]	Resolution [mm]	Rel. Efficiency [%]
0.42	0.54(2)	100
0.20	0.34(1)	85
0.10	0.24(1)	64

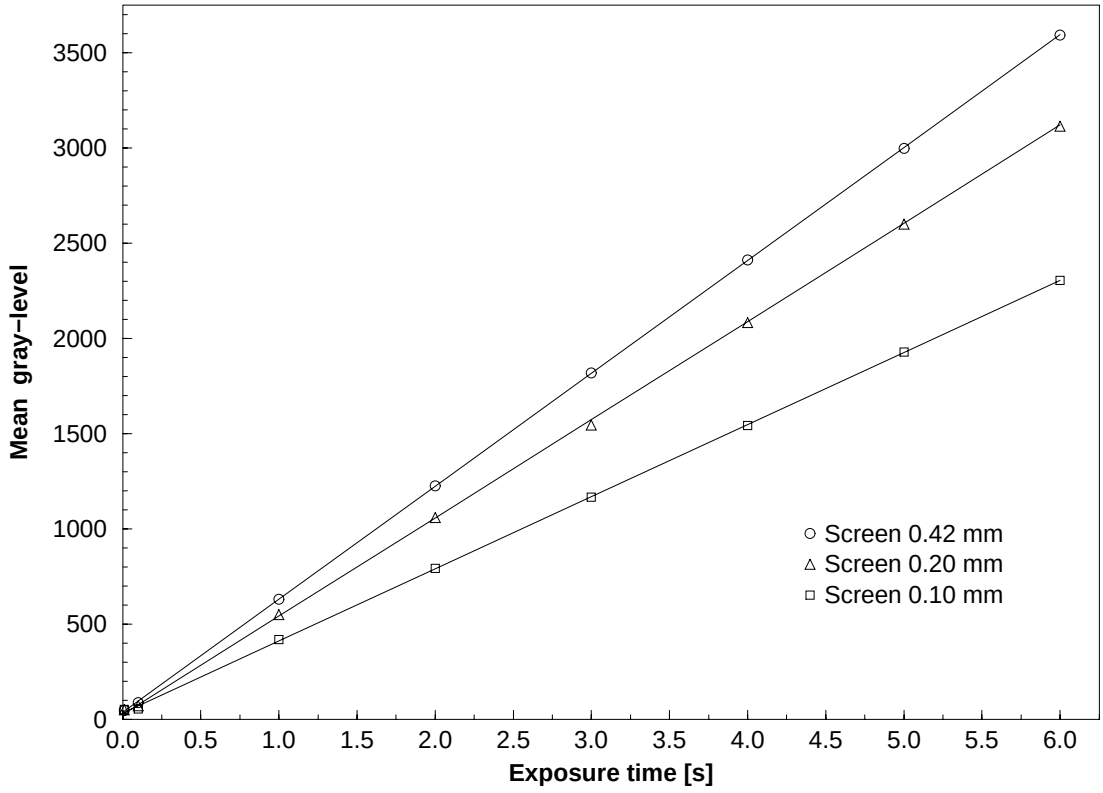

Fig. 2. Linearity and efficiency: dependency of the mean gray-level on the exposure time for different screens.

3.2 Linearity and efficiency

To compare the efficiency and linearity of the detection system depending on the choice of the scintillator, open beam measurements were performed with different exposure times for each scintillator. Then, the mean-gray-level value was determined over a region of interest

for each image and was plotted versus the exposure time. The data points fit perfectly a straight line, demonstrating a good linearity of the imaging device independently of the converter thickness (Fig. 2). Comparing the slopes of the linearity curves yielded the relative efficiency of both new thin scintillators in respect to the standard 0.42-mm-thick. The results, given in Table 1, show that the reduction in thickness carried out big improvements in the resolution while keeping a reasonable efficiency. Additionally, a 0.30-mm-thick Gd_2O_2S:Tb (gadolinium oxysulfide scintillator) scintillator (Kodak Lanex Fast screen), commonly used for X-ray imaging, has been tested for cold neutron imaging. Even though a reasonable resolution of 0.29 mm was obtained, the efficiency was nearly 8 times lower than the standard ^{6}LiF/ZnS:Ag. Thus, the 0.10-mm-thick ^{6}LiF/ZnS:Ag screen was undeniably the most appropriate scintillator and was used for the following measurements. Finally, radiographs of a relay in Fig. 3 illustrate clearly the enhancement of image sharpness using the thinnest converter. The object was placed in close contact to the converter plate for both images.

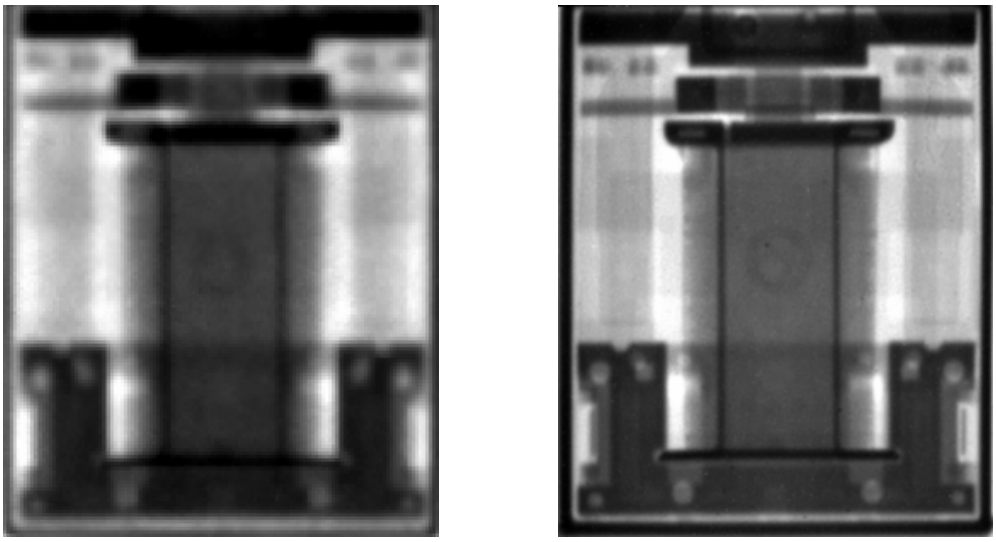

Fig. 3. Radiograph of a relay, 24 x 30 mm^2, taken with a) 0.42-mm-thick converter, b) 0.10-mm-thick converter.

3.3 Effects of beam divergence on spatial resolution

The divergence of the beam was studied by measuring ESF at different distances between the Gadolinium foil and the converter plane. Then, the spatial resolution extracted from different edge responses was plotted versus the distance. Fig. 4 shows experimental data points determined at both PGA and NCR neutron guides with errors corresponding to 1SD. The non-linear behavior observed at short distances

was generated by the inherent unsharpness of the detector that weighted predominantly in the general degradation compared to the geometric unsharpness. Removing the first value, data points fit perfectly to a straight line with a correlation coefficient of 1.000 in both cases. The geometric unsharpness relative to the distance object-converter given by 1/(L/D) corresponded to the linear regression slope. Thus, the L/D of 52 ± 2 obtained at the NCR station was in good agreement with the value of 50 ± 5 determined by the standard Kobayashi and Wakao method [13]. At the PGA beam line, the newly measured L/D of 68 ± 2 agrees with the previous value (L/D = 73 ± 4) determined using the standard 0.42-mm-thick scintillator [1]. Finally, these results demonstrated experimentally the higher beam divergence obtained at a super-mirror coated guide (NCR) in comparison with a Ni coated guide (PGA).

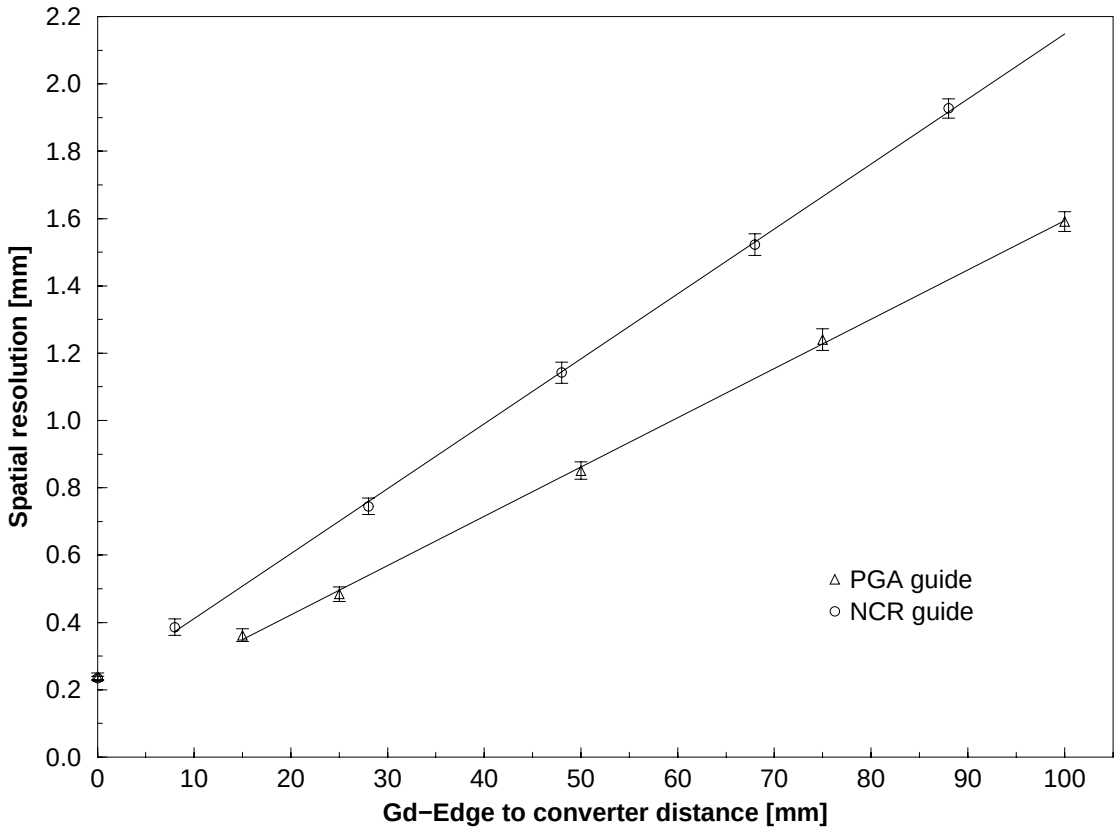

Fig. 4. Spatial resolution determined by the 10%-90% response of the Edge Spread Function versus the distance between the gadolinium foil and the scintillator plate.

4. Neutron imaging with the velocity selector

4.1 Characteristics

The neutron velocity selector is a high-speed turbine, which is transparent only for these neutrons which manage to pass between twisted lamellae inserted in the rotor in a time interval defined by the rotation speed of the selector. The turbine, which was 290-mm in diameter and 250-mm in length, consisted of 72 blades of carbon-fiber composite material coated with ^{10}B. This mechanical device selected neutrons in speed range between 3000 and 28300 rpm with a speed constancy of 0.2%. The case enclosing the rotor included two windows covered by 0.4-mm-thick aluminum foils for neutron entry and exit. In addition, vacuum and cooling systems ensured satisfactory support for the selector exploitation: the rotor temperature was kept between 15-25°C and the vacuum below 10^{-3} mbar. The selector was controlled and operated with its control and monitoring program via a PC.

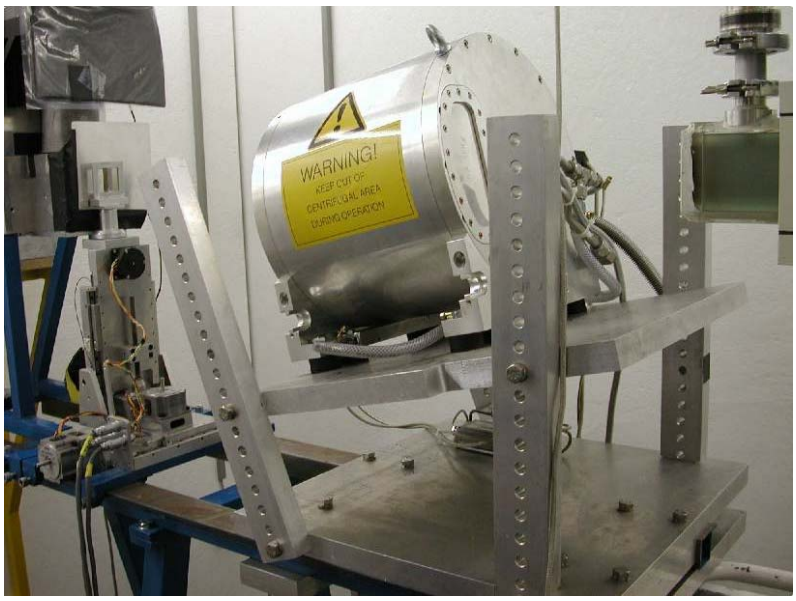

Fig. 5. Positioning of the neutron velocity selector at the PGA beam line for radiography and tomography purposes.

The wavelength distribution of neutrons is not only dependent on the rotation speed, but also on the tilting angle between the rotation axis and the neutron beam [14]. Thus, the velocity selector was fixed on a appropriate tilted table in order to achieve the desired neutron energy range (Fig. 5). The tilting angle chosen at 12.74° gave a suitable energy interval from 2.56 Å (at maximal speed) to 10.50 Å (at minimal speed), excepting between 4.48 and 5.24 as well as 8.08 and 9.35 due to resonance

selector frequencies. The energy resolution $\Delta\lambda/\lambda$ of the neutron distribution at the exit of the selector depends only on the tilting angle ξ and was in the order of 30%. So, neutron beams with relatively broad energy spectra were used for radiography investigations. In this way, the beam intensity was still reasonable at different neutron energy ranges to perform radiography experiments in short measuring times. This advantage was particularly suitable for tomography measurements.

4.2 Properties of the beam

A line profile was extracted horizontally across the image of the beam for different neutron wavelengths, in order to characterize the intensity distribution. At short wavelengths, the line profile showed a significant breakdown on the right side. With increasing wavelength, this inhomogeneity was first leveled off more and more and finally translated on the left side (Fig. 6). The wavelength dependence of the distribution over the width resulted from the curvature of the guide and the structure of beam profiles could be qualitatively verified by phase-space consideration [15]. To prove the reproducibility of inhomogenities in the beams generated by the velocity selector, a distribution pattern was measured two times under the same conditions. After dividing both images, the arithmetic mean μ and the standard deviation σ were calculated over a region of interest. The signal variation given by σ/μ [%] never exceeded 1.5 % independently on the wavelength and thus showed a good reproducibility of the velocity selector in combination with the detector.

The intensity of the transmitted beam was measured for different wavelengths and compared with the intensity of the white beam, i.e. the distribution without the velocity selector. For this purpose, the mean-gray-level value was calculated for each image and normalized by the exposure time. Plotting the relative intensity versus the wavelength gave the spectral neutron distribution of the white beam at the PGA guide (Fig. 7). Then, a semi-empirical $L/D = 1/\tan(2\gamma_c)$ was estimated by calculating the arithmetic mean value of all wavelengths as [2]:

$$\lambda_{av} = \frac{\sum_i \lambda_i \cdot n_i}{\sum_i n_i} = 5.0 \pm 0.2 \text{ Å} \qquad (1)$$

With the critical angle $\gamma_c = 0.1°/\text{Å}$ of a guide coated with natural nickel, a L/D of 57 was obtained. This estimation was available for a constant angular distribution of neutrons. In reality, imperfection of the guide decreased the reflectivity essentially at big angles, leading to a smaller effective divergence and thus a greater L/D. Finally, the fully experimental L/D-ratio determined previously was more reliable.

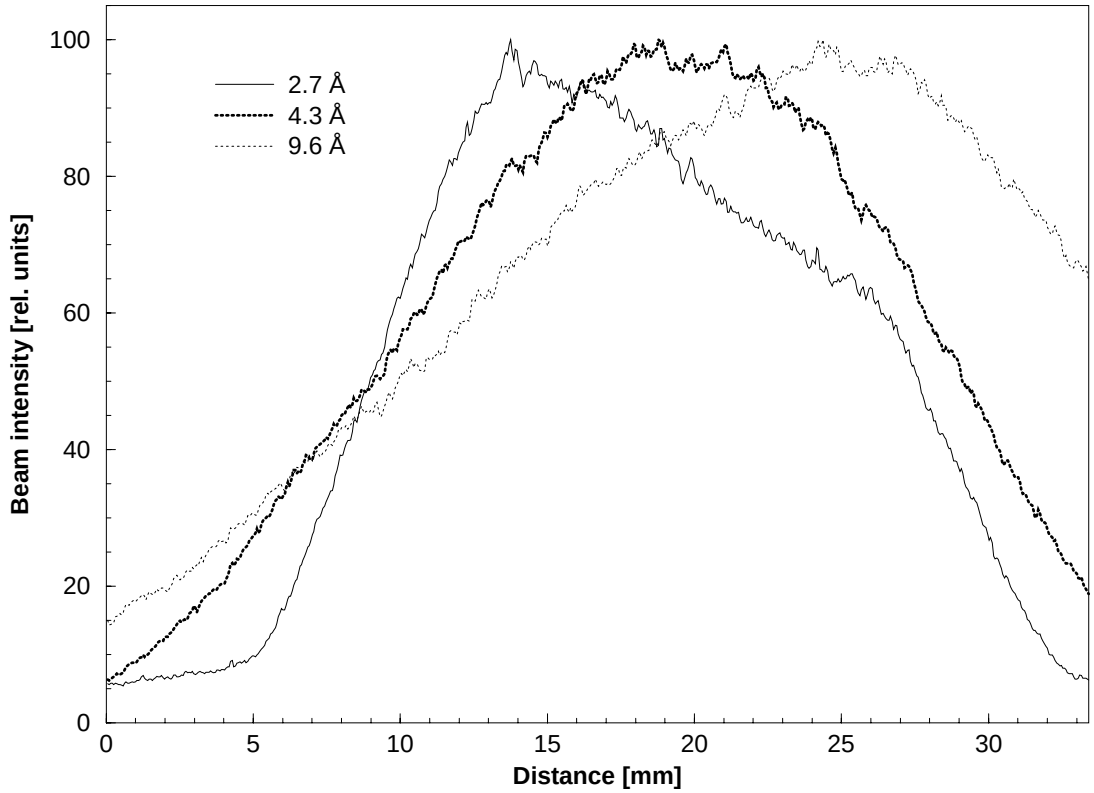

Fig. 6. Intensity profile over the width of monochromatic neutron beams at 2.7 Å, 4.3 Å and 9.6 Å.

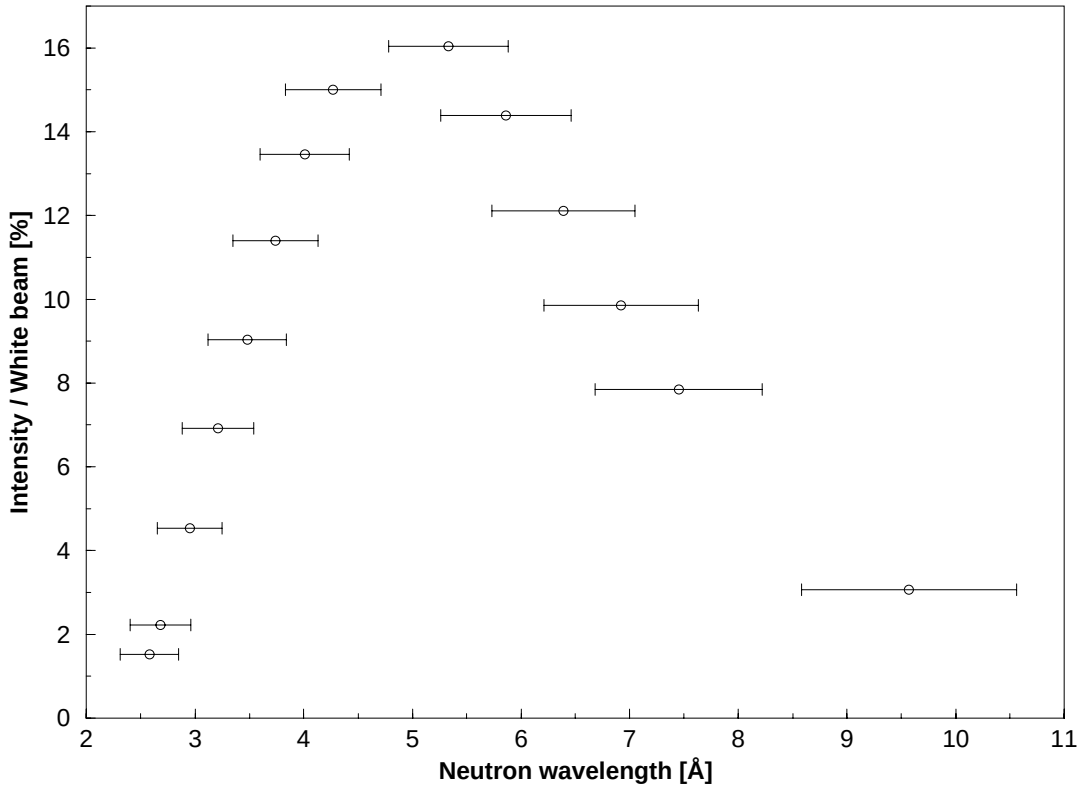

Fig. 7. Relative intensity of transmitted beams measured for different wavelengths yielding approximately the spectral neutron distribution of the white beam.

4.3 Spatial resolution

The influence of the selected neutron wavelength on the divergence angle was investigated by measuring sharp-edges at 5-cm from the scintillator plate. Then, the spatial resolution was determined conventionally by measuring the 10% to 90% response on the ESF (Fig. 8). At short wavelength, the resolution was considerably improved compared to the measurement performed without the velocity selector. The resolution at 5 cm from the converter reached 0.45 mm with the 2.7 Å monochromatic beam, instead of 0.85 mm using the white beam. In this case, the selector worked as a collimator thus enhancing the L/D. Although increasing the wavelength degraded gradually the image sharpness, a plateau was reached above 6.5 Å. Indeed, the divergence was restricted by the maximum acceptance of the velocity selector and became constant for the low energy component of the neutron spectrum.

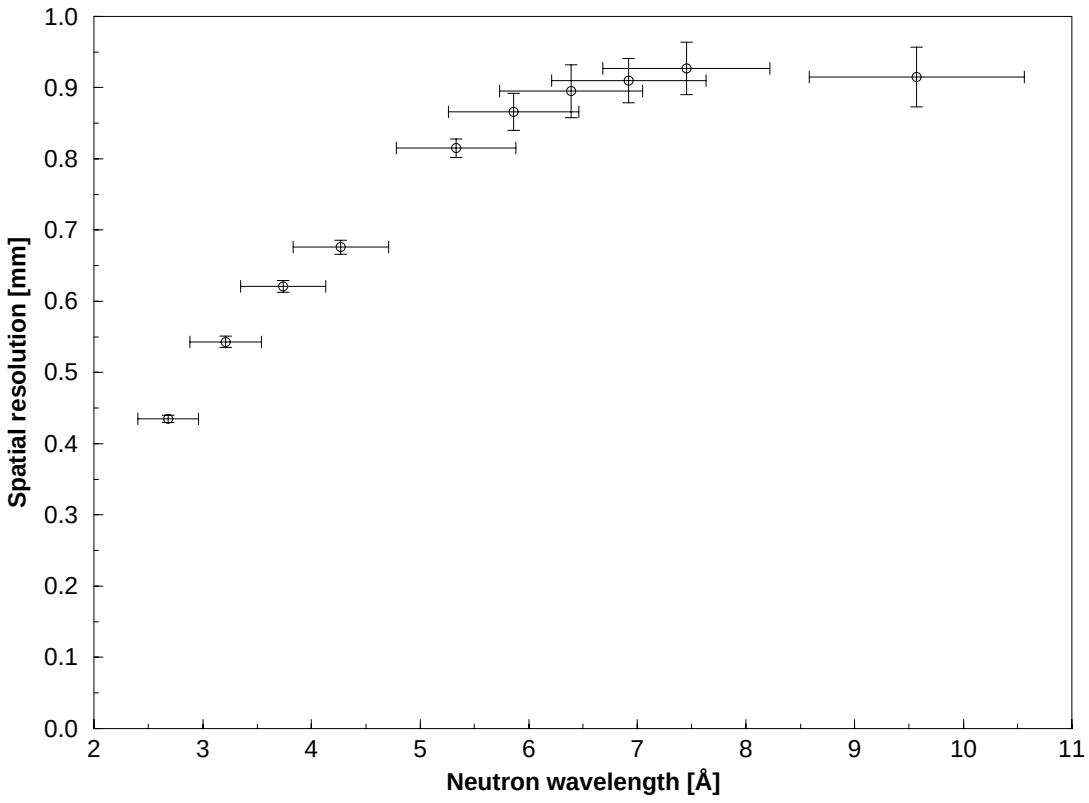

Fig. 8. Neutron wavelength dependence of the beam divergence on the spatial resolution measured at 5-cm from the scintillator plate.

For instance, a dried hornet was imaged using a neutron beam at two different wavelengths, 2.7 and 5.3 Å (Fig. 9). The specimen was fixed on a needle located at 2.5 cm from the converter plane. Both radiographs showed distinctly the three parts of the insect:

the head with strong mandibles, the thorax with three pairs of legs attached and the abdomen tipped with the stinger. The wings were nearly transparent to neutrons and thus hardly visible on the radiographs. As expected, the monochromatic beam at 2.7 Å (short wavelength) yielded sharper edges and reproduced finer details in the image. On the other hand, the contrast was improved at 5.3 Å due to the increment of attenuation coefficient in organic material at higher wavelengths.

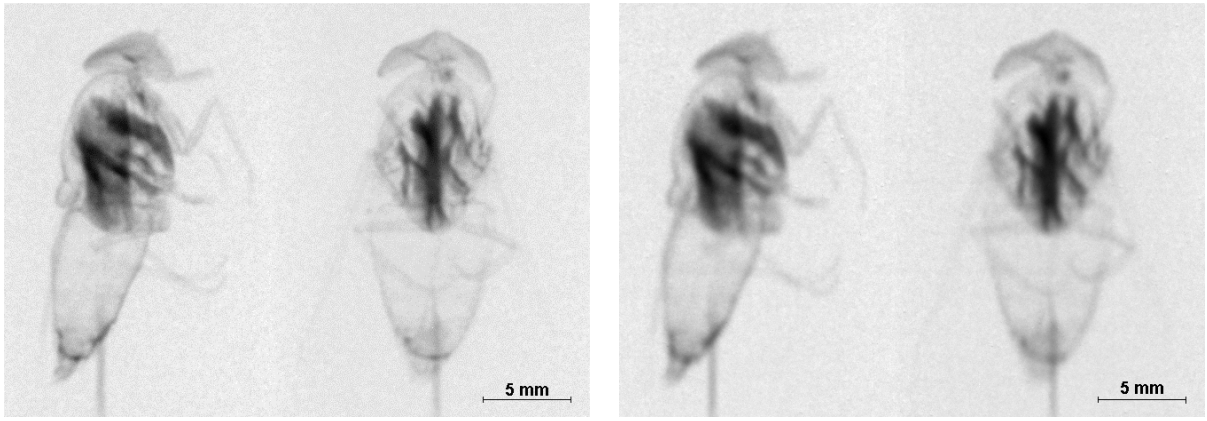

Fig. 9 . Profile and face radiographs of a 20-mm-long dried hornet a) at 2.7 Å and b) 5.3 Å.

5. Tomographic example

The quality of reconstructed objects in tomography was studied by measuring a 15-mm-width padlock according to different configurations. First, the experiment was performed with the ^{6}LiF/ZnS:Ag screen of standard thickness under normal beam conditions at the PGA neutron guide. Then, measurements were repeated after replacing the standard 0.42-mm by the 0.10-mm-thick converter. Finally, this last experiment was realized again using the neutron velocity selector to monochromatize the beam at 2.7 Å.

The distance between the object and the converter plane was as small as possible to minimize the beam divergence effects, i.e. 25 mm due to the mechanics of the system. Detected image pixels were created by binning together 2×2 26 µm CCD pixels, resulting in an effective size of 52 µm. This operation minimized the size of images and reduced the exposure time without affecting the quality of projections. Indeed, the spatial resolution greatly exceeded the pixel size. Consequently, measuring times of 1.5 s to 2.0 s per projection were sufficient for both converter screens using the standard beam . Because of the restricted neutron intensity of the selector at 2.7 Å, an exposure time of 80 s was required. The sample was rotated from 0° to 180° by discrete intervals of 0.9° resulting in 201

images. The data set was collected automatically using appropriate software. The data reconstruction consisting in processing successively horizontal slices of the object was based on a filtered back-projection algorithm using a Shepp-Logan filter [16], [17]. This procedure has been described in more details in ref. [1]. Finally, the volumetric object generated by the stack of image slices was visualized by VGStudioMax 1.0.

Reconstructed objects from the three different projection data sets are shown in Fig. 10. The image measured with the standard converter (a) was strongly blurred and thus the components were reconstructed oversized. More details were resolved and sharper objects were obtained using the 0.10-mm-thick screen (b). However, edges are more rounded than in the last image (c) measured with the neutron velocity selector. Differences were very prominent when looking at the springs.

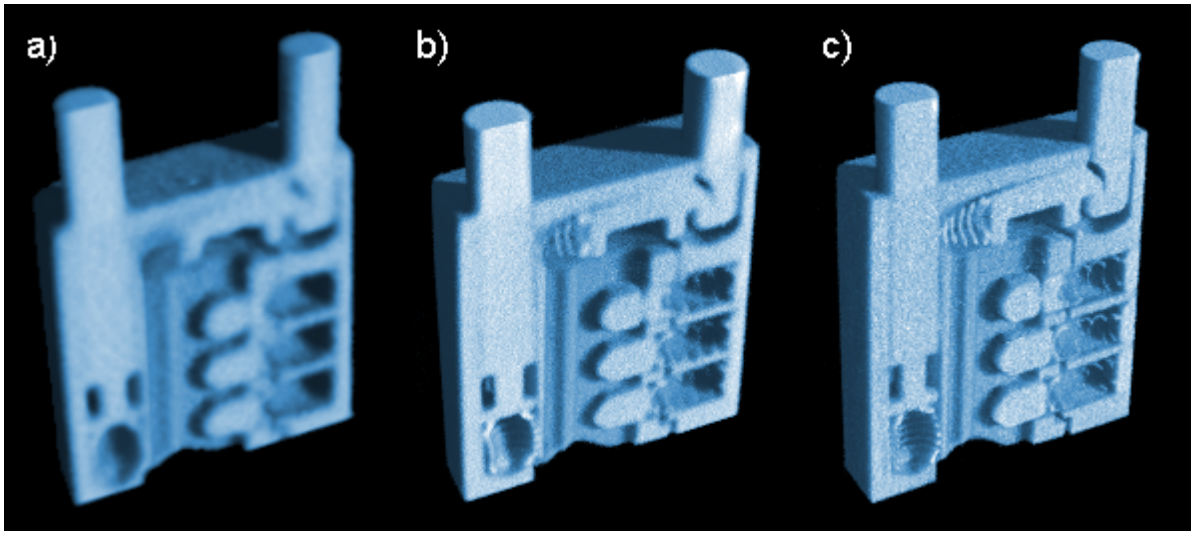

Fig. 10. Tomographic results of a small padlock (width = 15 mm) under the following configurations: a) white beam and 0.42-mm-thick scintillator, b) white beam and 0.10-mm-thick scintillator, c) monochromatic beam at 2.7 Å and 0.10-mm-thick scintillator.

6. Applications

A useful application of cold neutron tomography was found with respect to final storage of radioactive waste, where leaching tests are being performed on activated slag samples with arbitrary structures. Of importance for the determination of the leaching rate is the accurate measurement of the surface area of the sample. This task appears arduous for a piece with an irregular surface geometry. The current method using a calliper is time consuming and not really precise. In addition, radioactivity restricts the handling of real samples. Neutron tomography gives a good possibility to safely investigate

radioactive slag samples encapsulated in a lead container. Furthermore, cold neutrons, compared to thermal neutrons, have a lower attenuation coefficient for lead due to the Laue-Bragg scattering. The slag sample was tightly fixed inside a lead cylinder of 50 mm outer diameter and 5 mm wall thickness placed on the rotating table. The experiment was realized with the second configuration combining the 0.10-mm-thick screen and the normal beam. The tomographic procedure was followed as described above. Then, from the volumetric object, a polygonal iso-surface was extracted using VGStudioMax 1.0, thus yielding the surface area of the sample (Fig. 11). The surface area of inactivated or low activated samples were also calculated accurately using the calliper method and only 1.5% deviations were found with the surface area measured by neutron tomography. The technique has been applied with success for 7 different activated slag samples [18].

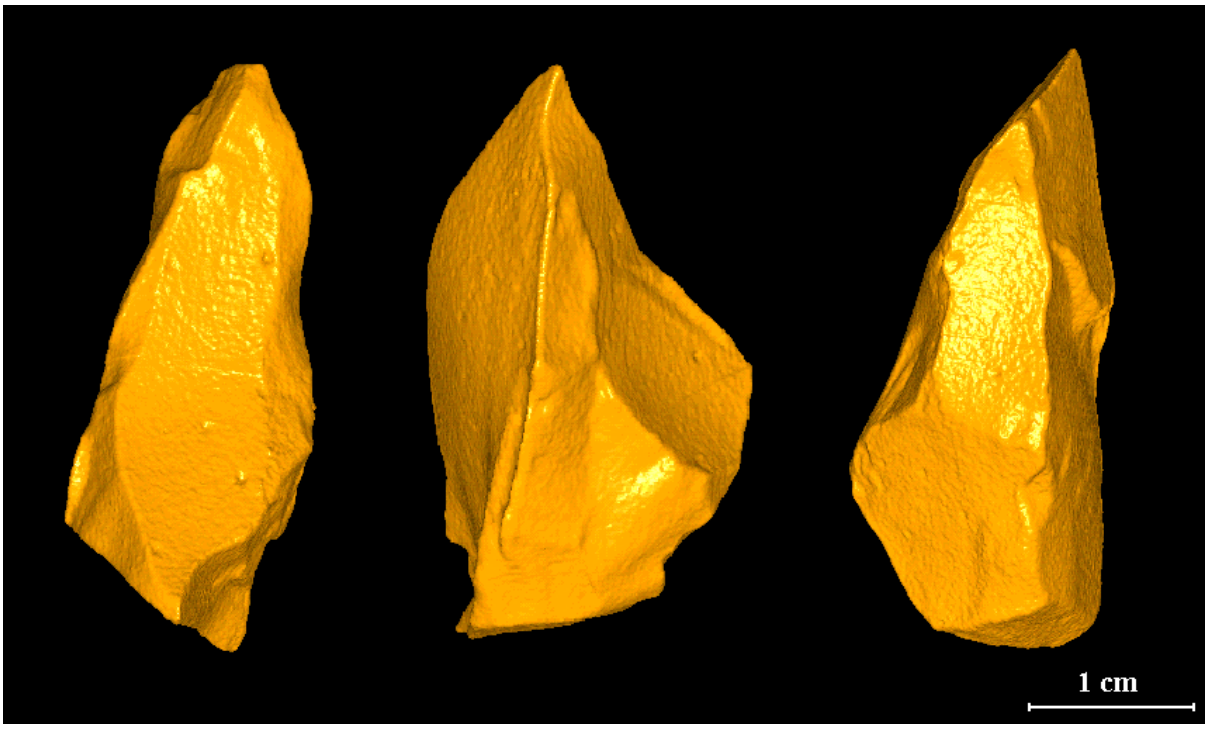

Fig. 11. Polygonal surfaces extracted from tomographic volumes of three activated slag samples. Surface areas: a) 13.01 cm^2, b) 14.83 cm^2, c) 17.43 cm^2.

Neutron radiography is a powerful tool for the quality-control of explosive devices used in space programs, such as Ariane launchers programs [19]. A pyrotechnic rod cutter provided by Dassault-Aviation has been recently inspected at the PGA beam line. Fig. 12 a) & b) shows a picture of the object and a neutron radiograph composed of 8 individual exposures. Cold neutrons were able to penetrate the object even though covered by

steel cladding. In addition, tomographic examinations were performed in the fixing device to obtain more information about the inner structures. A distance of 4 cm between the object and the converter was required to rotate the sample over 180°. The reconstructed object is showed in Fig. 12c) where components representing different materials were extracted from the volumetric data set. For instance, O-rings containing lots of hydrogen were easily segmented and could be controlled in minute detail.

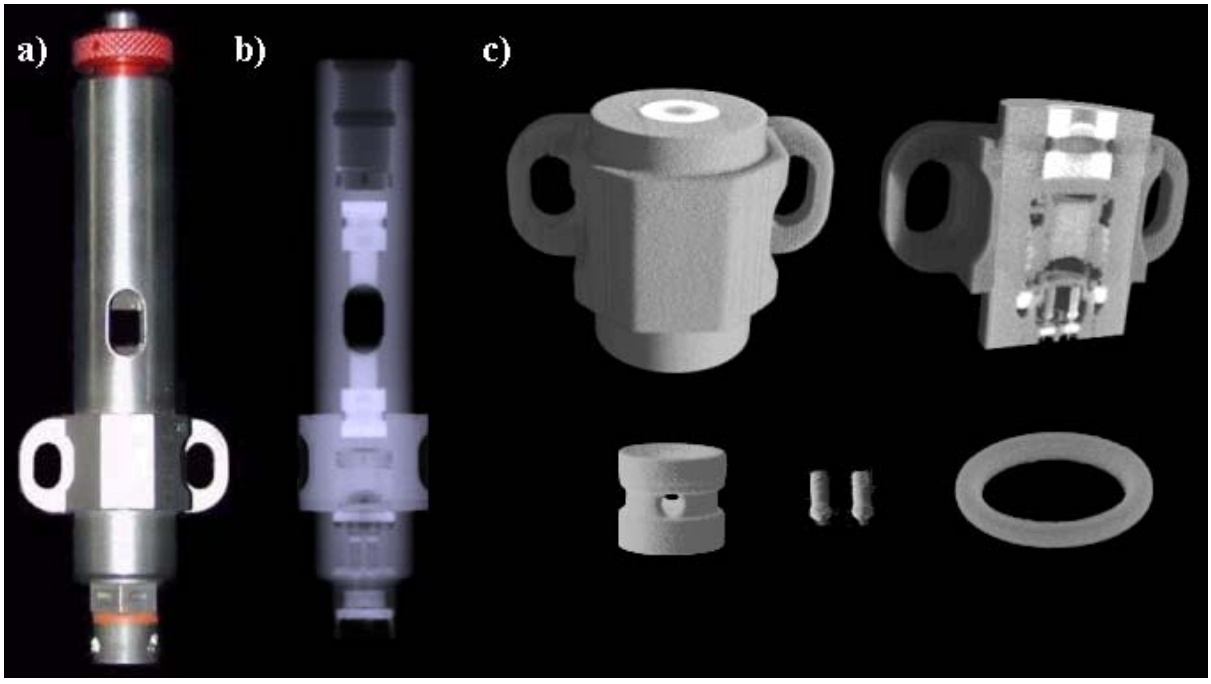

Fig. 12. Quality control of a 12-cm-height pyrotechnic cutter (Dassault-Aviation): a) picture, b) neutron radiograph, c) partial reconstructed volume and segmented components.

7. Conclusions

Thinner layers of ^{6}LiF/ZnS:Ag coating neutron converter resulted in lower spread character and thus improved image sharpness. The highest spatial resolution, about 0.24 mm, was achieved with the 0.10-mm-thick screen. At the same time, a reasonable efficiency was maintained despite the thinning down of absorbing material. At the end of the neutron guide, the low L/D degraded considerably the quality of images. Because the beam divergence decreases at short wavelength, selecting a harder neutron beam gave a good opportunity to improve the L/D. Thus, the neutron velocity selector installed at the PGA beam line acted as a collimator for selected neutrons being below 5 Å, which corresponded to the average wavelength (1) of the white beam distribution spectrum. Despite the smaller intensity of monochromatic beams, a realistic exposure time per radiography image

was achievable at most of the wavelengths.

For tomography experiments, projection data sets of good quality generated volumetric objects with sharper edges and finer details. Besides, cold neutron tomography was applied to determine the surface area of activated slag samples connected to radioactive waste storage. Furthermore, the technique yielded promising results for quality control in aerospatial industry. The velocity selector opens new possibilities for applied neutron radiography and tomography. For instance, the selector combined to the Bragg cutoff phenomenon can be used to differentiate among materials [Part II].

As a consequence of encouraging results provided by cold neutron imaging, a tomography set-up supplied by a neutron velocity selector will be installed permanently at the NCR location. A project of adding a flight tube at the end of the guide is under study in order to improve the L/D.

Acknowledgements

This work was supported by the Swiss National Science Foundation, the Paul Scherrer Institute and the COST action 524 WG-5 “Neutron Tomography and Computation Analysis”. The authors would like to acknowledge G. Frei and R. Erne for the technical support, P. Vontobel for his assistance, Dr. G. Bayon for providing the pyrotechnic cutter, Dr. H.P Zimmermann for his collaboration with inspection of radioactive waste. Also the authors wish to express their gratitude to Prof. Dr. P. Böni and Dr. R. Gaehler for the temporary transfer of the neutron velocity selector.

[1] S. Baechler, B. Masschaele, P. Cauwels, M. Dierick, J. Jolie, T. Materna, W. Mondelaers, Nucl. Instr. and Meth. A 481 (2002) 397.

[2] http://neutra.web.psi.ch

[3] B. Schillinger, Estimation and measurement of L/D on a cold and thermal neutron guide, 6th World. Conf. on Neutron Radiography, Osaka, 1999.

[4] H. Kobayashi, Beam Formation and Characterization for Neutron Radiography, Neutron Radiography (6), pp. 167-176, Gordon and Breach Science Publishers, 2000.

[5] For further information, see http://www.appscintech.com.

[6] E. Lehmann, P. Vontobel, L. Wienzel, Properties of the Radiography Facility NEUTRA at SINQ and its Potential Use as European Reference Facility, 6th Word Conf. on Neutron Radiography, Osaka, 1999.

[7] G. Kühne, R. Erne, PSI Annual Report 1999, Appendix VI, p. 70.

[8] T.E. McDonald Jr., T.O. Brun, T.N. Claytor, E.H. Farnum, G.L. Greene, C. Morris, Nucl. Instr. and Meth. A 424 (1999) 235.

[9] N. Kardjilov, energy-selective neutron radiography and tomography, submitted to J. Apll. Rad. Isotopes, 2001.

[10] G.S. Bauer, Nucl. Instr. and Meth. B 139 (1998) 65.

[11] S.W. Smith, The Scientist and Engineer's Guide to Digital Signal Processing, 2nd ed., California Technical Publishing, San Diego, 1997.

[12] A. A. Harms, D.R. Wyman, Mathematics and Physics of Neutron Radiography, D. Reidel Publishing Company, 1986.

[13] H. Kobayashi, H. Wakao, Accurate measurement of L, D and L/D for divergent collimators, Neutron Radiography (3), pp. 889-892, Kluwer Academic Publishers , 1990.

[14] http:\\sans.web.psi.ch/SANSDoc/node35.html#nvs

[15] W. Wagner, G.S. Bauer, J. Duppich, S. Janssen, E. Lehmann, M. Lüthy, H. Spitzer, J. Neutron Res. 6 (1998) 249.

[16] G.T. Herman, Image Reconstruction from Projections, Academic press, New York, 1980.

[17] Th. Materna, TOUPI. A Reconstruction and Visualisation Package. Internal report IPF-PAN. University of Fribourg, Switzerland, 1999.

[18] S. Baechler, J. Jolie, E. Lehmann, M. Patorski, H.P. Zimmermann, Labor für Radio- und Umweltchemie der Universität Bern und des Paul Scherrer Instituts, Annual Report 2001, p. 34.

[19] G. Bayon, Nucl. Instr. and Meth. A 424 (1999) 92.

List of publications

Refereed articles

Non-destructive analysis of a bulky sample from a natural fossil reactor, S. Baechler, M. Crittin, J. Kern, T. Materna, P. Cauwels, B. Masschaele, W. Mondelaers, H.U. Johner, V. Honkimaki, M. Piboule, J. Radioanal. Nucl. Chem. 250 (2001) 39.

Prompt gamma ray activation analysis for determination of boron in aqueous solutions, S. Baechler, P. Kudejova, J. Jolie, J.-L. Schenker, N. Stritt, Nucl. Instr. and Meth. A 488 (2002) 410.

The k_0-method in cold-neutron prompt gamma-ray activation analysis, S. Baechler, P. Kudejova, J. Jolie, J.-L. Schenker, Submitted for publication in J. Radioanal. Nucl. Chem. (2002).

The new cold neutron tomography set-up at SINQ, S. Baechler, B. Masschaele, P. Cauwels, M. Dierick, J. Jolie, T. Materna, W. Mondelaers, Nucl. Instr. and Meth. A 481 (2002) 397.

New features in cold neutron radiography and tomography, Part I: Thinner scintillators and a neutron velocity selector to improve the spatial resolution, S. Baechler, N. Kardjilov, M. Dierick, J. Jolie, G. Kühne, E. Lehmann, T. Materna, Submitted for publication in Nucl. Instr. and Meth. A (2002).

New features in cold neutron radiography and tomography, Part II: Applied energy-selective neutron radiography and tomography, S. Baechler, N. Kardjilov, M. Dierick, J. Jolie, G. Kühne, E. Lehmann, T. Materna, Submitted for publication in Nucl. Instr. and Meth. A (2002).

The development of a high-power bremsstrahlung radiator for the production of monochromatic X-rays, P. Cauwels, B. Masschaele, W. Mondelaers, S. Baechler, J. Jolie, T. Materna, Radiat. Phys. Chem. 61 (2001) 439.

First results of micro-neutron tomography by use of a focussing neutron lens**,** B. Masschaele, S. Baechler, P. Cauwels, M. Dierick, J. Jolie, W. Mondelaers, Radiat. Phys. Chem. 61 (2001) 623.

Element sensitive X-ray micro tomography for determination of the metal diffusion in teeth with amalgam fillings, B. Masschaele, S. Baechler, P. Cauwels, P. Cloetens, M. Dierick, J. Jolie, W. Mondelaers, Radiat. Phys. Chem. 61 (2001) 625.

Contribution to Conferences, Workshops and Seminars

Non-destructive analysis of a bulky sample from a natural fossil reactor**,** S. Baechler, M. Crittin, J. Kern, T. Materna, P. Cauwels, B. Masschaele, W. Mondelaers, H.U. Johner, V. Honkimaki, M. Piboule, in Proc. of the 10th Int. Symp. on Capture Gamma-Ray Spectroscopy and Related Topics, Santa Fe, USA, August 30 - September 3, 1999, Ed. Stephen Wender, (2000) 734.

The PGA installation at SINQ**,** S. Baechler, Internal talk at PSI, Neutron Scattering session, May 16, 2000.

Comparison of tomography using cold neutrons and high energy X-rays**,** S. Baechler , P. Cauwels, J. Jolie, B. Masschaele, T. Materna, W. Mondelaers, 5th Int. Conf. on Nuclear and Radiochemistry, Pontresina, Switzerland, September 3-8, 2000, book of abstracts p. 298.

Comparison of tomography using cold neutron and high energy X-rays, S. Baechler, Oberseminar über Strahlenphysik, Institut für Kernphysik, Universität zu Köln, Deutschland, February 13, 2001.

A 15-MeV Linear Electron Accelerator-Based Source of Tunable Monochromatic Hard X-Rays, W. Mondelaers, B. Masschaele, P. Cauwels, M. Dierick, P. Lahorte, J. Jolie, S. Baechler, T. Materna, Proc. of the 20th Int. Linac Conf., Monterey, USA, August 21-25, 2000.

Status and prospects of neutron tomography in Europe, E. Lehmann, P. Vontobel, B. Schillinger, T. Bücherl, S. Baechler, J. Jolie, W. Treimer, R. Rosa, G. Bayon, S. Legoupil, S. Körner, V. Micherov, M. Balasko, in Proc. of the 15th World Conf. on Non-Destructive Testing, Rome, Italy, October 15-21,2000.

Applied energy-selective neutron radiography and tomography, N. Kardjilov, S. Baechler, E. Lehmann, Int. Conf. on Neutron Scattering, München, Germany, September 9-13, 2001.

Non-refereed papers and reports

Prompt gamma analysis of a sample from a natural reactor using a neutron focusing capillary lens, S. Baechler, J. Jolie, PSI Annual Report 2000, Vol. VI, p. 63.

Prompt gamma-ray activation analysis of ashes from the PSI-incinerator, S. Baechler, J. Jolie, H.-F. Beer, M. Rüthi, S. Bajo, M. Egloff, M. Patorski, H.-U. Aebersold, E. Lehmann, H.-P. Zimmermann, Labor für Radio- und Umweltchemie der Universität Bern und des Paul Scherrer Instituts, Annual Report 2001, p. 33.

Determination of the surface area of activated slag samples, S. Baechler, J. Jolie, M. Patorski, H.P. Zimmermann, Labor für Radio- und Umweltchemie der Universität Bern und des Paul Scherrer Instituts, Annual Report 2001, p. 34 .

Applied energy-selective neutron radiography and tomography at PGA station, S. Baechler, N. Kardjilov, G. Frei, E. Lehmann, PSI Annual Report 2001.

Setup of a CCD based detection system at the NCR station, S. Baechler, M. Dierick, R. Erne, G. Kühne, T. Materna, PSI Annual Report 2001.

Curriculum vitae

Nom :	Baechler
Prénom :	Sébastien
Date et lieu de naissance :	21 mai 1975, Fribourg
Nationalité :	Suisse
Lieu d'origine :	Rechthalten (FR)
Etat civil :	célibataire

Formation

1981-1987	Ecole primaire à Corminboeuf (FR)
1987-1990	Ecole secondaire au Cycle d'Orientation du Belluard à Fribourg
1990-1994	Collège St-Michel à Fribourg, maturité type C
1994-1999	Université de Fribourg, diplôme en physique expérimentale
1999-2002	Université de Fribourg, assistant/doctorant en physique

Diplômes

Maturité fédérale en type C

Diplôme en physique expérimentale

Diplôme de maître de gymnase

Acknowledgements

First, I would like to express my gratitude to Prof. Dr. Jan Jolie who has guided my research work with enthusiasm and valuable scientific insight. I have benefited from his knowledge, competence and experience.

I thank Prof. Dr. Jean-Claude Dousse who gladly accepted that I joined his research group to pursue my thesis work in Fribourg. I am very grateful for his availability for advice.

I also address my thanks to Dr. Eberhard Lehmann for the profitable collaboration at PSI. He was always open to helpful discussions and advice.

I am grateful to Jean-Luc Schenker who helped me with the electronics.

Special thanks to Petra Kudejova, Thomas Materna, Manuel Dierick, Bert Masschaele, Nikolay Kardjilov, Laurent Genilloud, Gabriel Frei, Guido Kühne, Peter Vontobel, Peter Zimmermann for their help during my thesis work.

I am also grateful to all other members of the former group PAN and the present group FRAP, especially Michel Berset, Yves-Patrick Maillard, Olivier Mauron and Pierre-Alexandre Raboud for the pleasant atmosphere during work.

I acknowledge the Swiss National Science Foundation and the Paul Scherrer Institute who supported this work financially.

Finally, many thanks to the administrative and workshop staff for their kindness, and to all of those I would have forgotten to mention.

Je tiens enfin à remercier tout particulièrement mes parents qui m'ont permis de mener à bien mes études, et m'ont encouragé et aidé financièrement durant toutes ces années.

Merci également à mon amie Stéphanie, tous mes proches, mes amis, qui m'ont toujours soutenu tout au long de mes études.